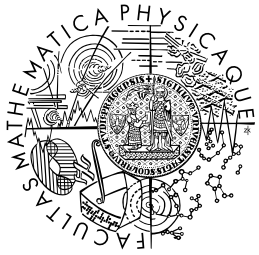

FACULTY
OF MATHEMATICS
AND PHYSICS
Charles University

DOCTORAL THESIS

Tomáš Vlasák

Microstructural investigations of novel high entropy alloys

Department of Low Temperature Physics

Supervisor of the doctoral thesis: prof. Mgr. Jakub Čížek, Ph.D.

Study programme: Physics

Study branch: Physics of Condensed Matter and Materials Research

Prague 2022

I declare that I carried out this doctoral thesis independently, and only with the cited sources, literature and other professional sources. It has not been used to obtain another or the same degree.

I understand that my work relates to the rights and obligations under the Act No. 121/2000 Sb., the Copyright Act, as amended, in particular the fact that the Charles University has the right to conclude a license agreement on the use of this work as a school work pursuant to Section 60 subsection 1 of the Copyright Act.

In Prague 27 September 2022 .....

Mgr. Tomáš Vlasák

I would like to thank professor Čížek for supervising my thesis.

Title: Microstructural investigations of novel high entropy alloys

Author: Tomáš Vlasák

Department: Department of Low Temperature Physics

Supervisor: prof. Mgr. Jakub Čížek, Ph.D., Department of Low Temperature Physics

Abstract: High entropy alloys constitute a novel approach in materials research. In this thesis, four novel alloys (namely NbTaTiZr, HfNbTaTiZr, HfNbTiVZr and HfNbTaTiVZr) are investigated. Their microstructure and mechanical properties are studied both in the as-cast and the annealed state. It is shown that their strengthening is caused by lattice distortions, which are the result of random filling of lattice sites by atoms of various elements with different atomic radii. Furthermore, positron annihilation investigations revealed that positrons actively search for open volumes in interstitial regions associated with lattice distortions, and therefore lattice distortions can be characterised by positron lifetimes.

Keywords: high entropy alloys positron annihilation

Contents

Introduction

This doctoral thesis deals with high entropy alloys, which constitute a relatively new approach in materials science. They are alloys consisting of at least five allying elements each with concentration in the range $(5 - 35)$ at.%. In the literature four common effects of HEA has been described: the high entropy effect, the lattice distortion effect, the sluggish diffusion effect and the so-called cocktail effect. It has been proposed that these so-called core effect are responsible for unique properties of HEAs.
In this thesis I investigated the microstructure and mechanical properties of NbTaTiZr, HfNbTaTiZr, HfNbTiVZr and HfNbTaTiVZr alloys. As the HfNbTaTiZr alloy proved to be the most promising one, further investigations were done on it. This included processing using severe plastic deformation in order to achieve grain refinement down to nano-scale and measurements using scanning electron microscopy, positron annihilation spectroscopy and measurements of mechanical properties.

1. High entropy alloys

1.1 Definition of high entropy alloys

High entropy alloys (HEAs) constitute a relatively new approach in materials science. This approach was proposed in 1995 and the first results concerning high entropy alloys were published in 2004. The definitions of the term 'high entropy alloy' currently used in the literature vary, but two notions lie at the core of all of them: high entropy alloys should consist of at least four (usually five or six) alloying elements and / or should show high entropy of mixing. The following paragraphs show how these two notions are in fact closely related.
The molar configurational entropy of mixing for ideal solutions of N elements is given by the equation

$$ {}^{M}S^{ideal} = -R\sum_{i}^{N} x_i \ln x_i, \tag{1.1} $$

where R is the gas constant and x_i is the molar fraction of the i-th alloying element, which can be defined as

$$ x_i = \frac{n_i}{\sum_i^N n_i}, \tag{1.2} $$

where n_i is the number of moles of the i-th element present in the alloy.
It can be easily seen that the ideal entropy of mixing has the highest value for the case when $x_1 = x_2 = \cdots = x_N$ (so-called equimolar solution). Furthermore, one can see that the more alloying elements are dissolved in an equimolar solution, the bigger the ideal entropy of mixing is. This corresponds to the fact that the entropy of mixing is proportional to the number of different possibilities in which the elements can occupy lattice sites, which is naturally greater in a solution of more alloying elements.
For the case of $N = 2$ and $x_1 = x_2 = \frac{1}{2}$ (i.e. binary equimolar ideal solution), a simple calculation gives the value of ideal entropy of mixing of just $\Delta S_{mix}^{ideal} \approx 0.69R$. The entropy of mixing of ideal equimolar solution of five elements can be similarly evaluated as $\Delta S_{mix}^{ideal} \approx 1.61R$.
The theory of ideal solutions assumes that the elements occupy lattice sites randomly. This assumption is only rarely fulfilled in real solutions. Nonetheless, the formula for the ideal entropy of mixing shows how large number of alloying elements can possibly lead to high mixing entropies as compared to the entropies of conventional binary or ternary alloys.
One can use the values of entropy of mixing of ideal equimolar solutions for forming a precise definition of high entropy alloys. Yeh classifies alloys into three categories based on their correspoding ideal entropy of mixing. Yeh [2006] The boundary values of entropy are chosen as values of molar entropy of mixing for ideal equimolar solutions of two and five elements as follows:

- low entropy alloys: $S_{mix}^{ideal} < 0.69R$,
- medium entropy alloys: $0.69R < S_{mix}^{ideal} < 1.61R$,
- high entropy alloys: $S_{mix}^{ideal} > 1.61R$.

1.2 Thermodynamics of phase formation

1.2.1 Gibbs free energy

There are usually many competing phases in an alloy. Thermodynamically stable phases can be predicted by minimizing the Gibbs free energy. The molar Gibbs free energy for phase $\oslash$ is given by the formula

$$G_m^{\oslash} = \sum_i^N x_i {}^{\circ}G_i^{\oslash} + {}^{M}G^{ideal} + {}^{E}G^{\oslash}, \tag{1.3}$$

where x_i is the mole fraction of the i-th alloying element, ${}^{\circ}G_i^{\oslash}$ is the molar Gibbs energy for the pure i-th element, ${}^{M}G^{ideal}$ is the ideal molar Gibbs energy of mixing and ${}^{E}G^{\oslash}$ is the excess molar Gibbs energy. All so-called ideal quantities refer to ideal solutions, i.e. solutions where all elements are completely soluble and are mixed randomly.
By taking pure elements as the standard states we can leave out the first term in the equation. The second term can be rewritten using standard thermodynamic relation $G = H - TS$ in this way:

$$G_{mix}^{ideal} = {}^{M}H^{ideal} - T{}^{M}S^{ideal}, \tag{1.4}$$

where ${}^{M}H^{ideal}$ is the ideal enthalpy of mixing, T is the temperature and ${}^{M}S^{ideal}$ is the ideal entropy of mixing. Since the enthalpy of mixing in ideal solutions is zero, the preceding formula can be rewritten as

$${}^{M}G^{ideal} = -T{}^{M}S^{ideal}. \tag{1.5}$$

As already mentioned in the previous section, the ideal entropy of mixing is given by

$${}^{M}S^{ideal} = -R\sum_i^N x_i \ln x_i, \tag{1.6}$$

where R is the gas constant. The third term in the equation for molar Gibbs energy 1.3 can be similarly rewritten as

$${}^{E}G = {}^{E}H^{\oslash} - T{}^{E}S^{\oslash}, \tag{1.7}$$

where ${}^{E}H^{\oslash}$ is the excess entropy and ${}^{E}S^{\oslash}$ is the excess entropy, both terms are originating from the nonideality of the solution.
In the next sections the ideal and excess entropies will be combined into one quantity $S^{\oslash} = {}^{M}S^{ideal} + {}^{E}S^{\oslash}$ and the excess enthalpy of mixing will be denoted as ${}^{E}H^{\oslash} = H^{\oslash}$, so we can write

$$G^{\oslash} = H^{\oslash} - TS^{\oslash}. \tag{1.8}$$

1.2.2 Solid solutions

Solid solutions are a class of materials that consist of well soluble constituents and posses a single crystal structure.

For a simple prediction whether an element can dissolve in a metal and form a solid solution one can use Hume-Rothery rules. These rules are purely empiric and have a different form for substitutional and interstitial solid solutions. The rules for substitutional solid solutions are as follows:

1. If a solute atom differs in its atomic size by more than about 15% from the solvent atom, the solubility is likely to be low.

2. If a solute atom and the solvent atom have very different electronegativity, than there is a tendency for the two elements to form a compound rather than a solid solution.

3. A metal of lower valency is more likely to dissolve to a large extent in one of higher valency and vice versa. [Smallman and Ngan, 2014]

The molar Gibbs energy for the solid solution phase is given by

$$G^{SS} = H^{SS} - TS^{SS}. \tag{1.9}$$

In ideal solution the enthalphy H^{SS} is zero and the entropy of mixing S^{SS} is just the ideal configurational entropy ${}^{M}S^{ideal}$, the excess term is zero. In regular solutions the enthalpy of mixing is nonzero, $H^{SS} \neq 0$, and the entropy of mixing is taken as the same as that for ideal solution, even though atoms does not have entirely random positions. In real subregular solutions, both the enthalpy of mixing H^{SS} and the excess entropy of mixing ${}^{E}S^{SS}$ are nonzero. If the enthalpy is $H^{SS} > 0$, there is a tendency towards phase separation. On the other hand, if the enthalpy is $H^{SS} < 0$, there is a tendency toward chemical short-range ordering. Vast majority of binary metallic solutions behave nonideally.
The entropy S^{SS} of real, sub-regular solutions consists of ideal configurational entropy, an excess configurational term resulting from unequal sized atoms and other non-configurational terms like the vibrational term, the electronic term and the magnetic term. It is not clear to which extent the entropy and the shape of the curve depicting dependency of entropy on composition is affected by the fact that in sub-regular solutions atoms are not distributed randomly. [Miracle and Senkov, 2017]
For ideal and regular binary solutions the curves depicting dependence of enthalpy and Gibbs energy on mole fraction of one constituent is symmetric with respect to the equimolar concentration. It is very difficult to obtain experimental H^{SS} data for real systems. A common approximation of the enthalpies can be obtained using the Miedema method Miedema [1973]. The enhalpies given by this model are approximate only, typical error is very large, around 35% even after removing estimates with errors over 100%. Nonetheless, the model can predict good or bad solubility with a high precision. [Miracle and Senkov, 2017] The enthalpy in the Miedema scheme for a binary system can be approximated by the equation

$$H = 4\left[\sum_{k=0}^{3} \Omega_k \left(x_1 - x_2\right)^k\right] x_1 x_2, \tag{1.10}$$

where Ω_k are interaction parameters and x_1 and x_2 are the molar fractions of the first and second element, respectively.

For subregular solutions the minimum of H^{SS} and therefore G^{SS} does not need to like exactly at $x_1 = x_2 = 0.5$, but it lies usually in close vicinity in the range $x_1 = 0.5 \pm 0.1$. [Miracle and Senkov, 2017] Examples of thermodynamic potentials for a regular solution (Co-Ni) and a subregular solution (Ni-Ce) given by Takeuchi and Inoue [Takeuchi and Inoue, 2010] are plotted in figures 1.1 and 1.2.

Figure 1.1: Molar enthalpy, entropy and Gibbs energy of mixing for Co-Ni. Data taken from [Takeuchi and Inoue, 2010].

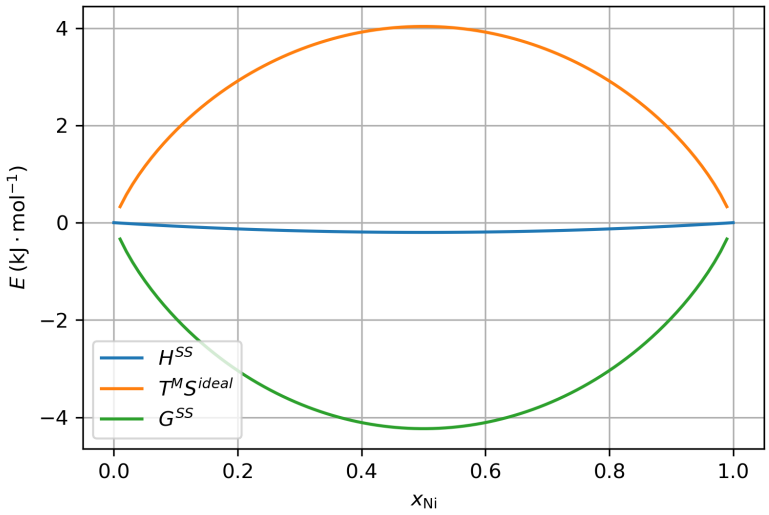

Figure 1.2: Molar enthalpy, entropy and Gibbs energy of mixing for Ni-Ce. Data taken from [Takeuchi and Inoue, 2010].

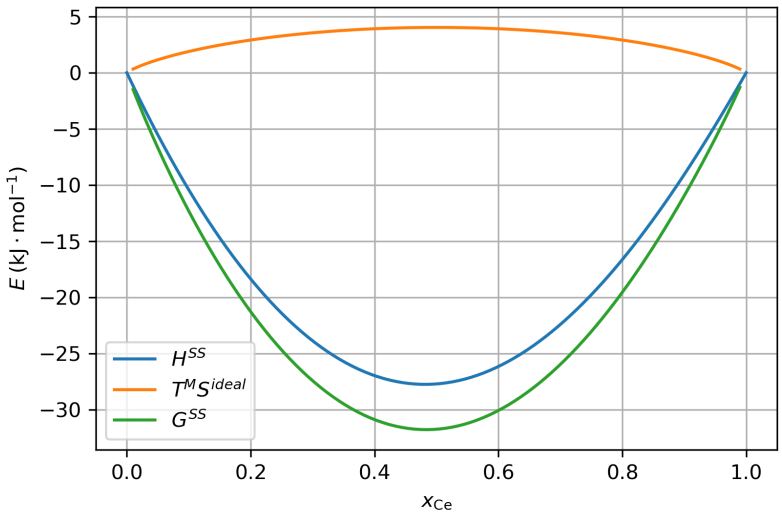

1.2.3 Intermetallic phases

Intermetallic (IM) compound is a type of alloy that displays long-range ordering of atoms on two or more sub-lattices. The probability of finding an atom on a

given site in ideal solid solutions is given by its molar fraction x_i. In sub-regular solid solutions, atoms are not distributed perfectly randomly, but the probability of finding an atom on a given site should not differ significantly from its molar fraction x_i. On the other hand, in intermetallics the probability of finding an atom on a given sub-lattice is significantly different from x_i due to long-range ordering, and is usually very close to 0 or 1.
The Gibbs energy for the itermetallic phases is given by the equation

$$G^{IM} = H^{IM} - TS^{IM}. \tag{1.11}$$

The entropy of IM phases is very low in traditional alloys and it can be assumed that it is essentially zero for a perfectly ordered IM phase. However, the configurational entropy can increase in concentrated alloys when the alloy consists of more elemental constituents than the number of lattice sites is. The ideal configurational entropy of such an alloy can then be estimated as

$$S^{IM,ideal} = -R\frac{\sum_{x=1}^{N_s}\left(\sum_{i=1}^{N} f_i^x \ln f_i^x\right)}{\sum_{x=1}^{N_s} a^x}, \tag{1.12}$$

where i is an index marking different atom species present on the same sub-lattice, N is the total number of atom species, x is an index marking sub-lattices, N_s is the number of sub-lattices, a^x is the number of sites on the x-th sub-lattice and f_i^x is the inverse of the number of different atom species present on the x-th sub-lattice.
When applying this model it is neccessary to take care as the composition on each sub-lattice may differ from that given by stoichiometric ratios. Experimentally, it is very difficult to determine which elements are present on which sub-lattice and whether the elements are distributed randomly on the sub-lattice. [Miracle and Senkov, 2017]
A classical theory gives the enthalpy of IM phase in the following form:

$$H = \sum_{i,j} \left(n_{i,j}\varepsilon_{i,j}\right), \tag{1.13}$$

where $\varepsilon_{i,j}$ are the bond enthalpies between neighbouring i-th and j-th atoms and $n_{i,j}$ the number of bonds with neighbouring atoms per atom.
Solid solutions and intermetallic compounds of the same composition have generally the same bond enthalpies $\varepsilon_{i,j}$, but the number of bonds $n_{i,j}$ differs. For example, in intermetallic compounds an atom of the first type can be surrounded only by atoms of another type, which would give $n_{11} = 0$, whereas in solid solutions where atoms are distributed more randomly this number is likely to be $n_{11} > 0$.
Miracle and Senkov [Miracle and Senkov, 2017] compared enthalpies of the solid solution phases calculated using the Miedema method by Takeuchi et al. [Takeuchi and Inoue, 2010] and enthalpies of intermetallic phases taken from various sources. Histogram of 1176 values of H^{SS} (around equimolar composition) and 1055 values of H^{IM} (around stoichiometric composition) for metal-metal and metal-semimetal compounds is plotted in figure 1.3.
In intermetallic phases one can expect to find more bonds between unlike atoms, which are more stable than bonds between the same atoms. Therefore enthalpies

Figure 1.3: Comparison of the enthalpies of the SS and IM phases. Taken from [Miracle and Senkov, 2017].

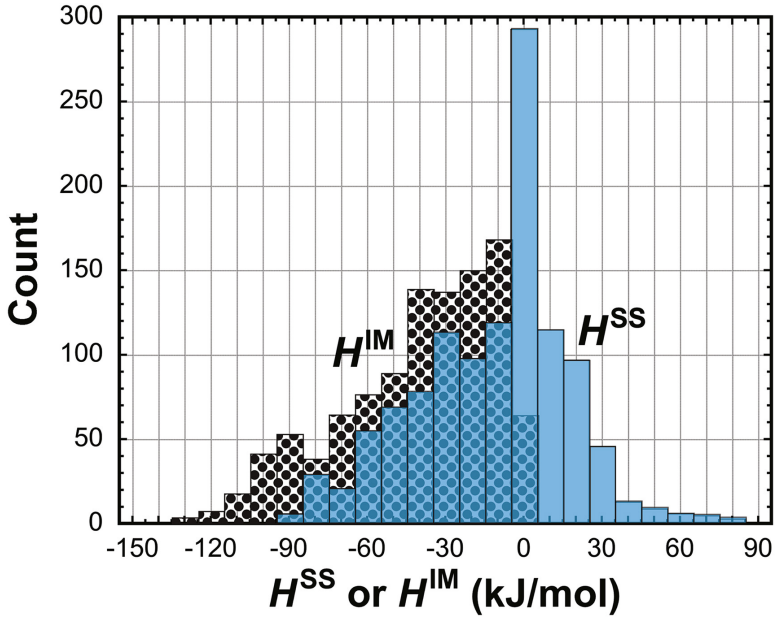

of the IM phases should be lower than enthalpies of SS phases. The data plotted in the figure show this trend.

1.3 HEA core effects hypotheses

Although the concept of high entropy alloys is rather new and only a small fraction of possible alloys has been studied experimentally, several common effects have been identified and described in the literature. These effects are proposed to be the cause of the exceptional characteristics of HEAs and are therefore called *HEA core effects*. There are four of them, namely the high entropy effect, the lattice distortion effect, the sluggish diffusion effect and the coctail effect. The following sections give a brief overview of them.

1.3.1 The high entropy effect

The high entropy effect hypothesis says that the configurational term of the entropy of HEAs should dominate over vibrational, electronic and magnetic terms and that it may favour solid solution (SS) phases over competing intermetallic (IM) phases.

The first hypothesis is usually based on qualitative comparisons only. For example, Yeh et al. [Yeh et al., 2004b] compares the ideal configurational entropy with the entropy of metal fusion. By Richards' rule, the entropy changes in fusion should be around $\approx R$ (k_B per atom) for many elements at their melting points. The configurational entropy for ideal equimolar solution of three elements is already higher. However, the Richards' rule is not found to be universally applicable. [Grimvall, 1999]

Another problem is that it is not fully known to what extent is the entropy of solid solution HEAs similar to the ideal configurational entropy. The statement

that atoms are randomly distributed in HEAs have never been experimentally proved. In fact, vast majority of solid solution are subregular and therefore their atoms are not distributed fully randomly, but there are local correlations between atoms of various elements. This causes the entropy term to differ from the ideal one. [Miracle and Senkov, 2017]

Due to the second hypothesis, some authors may assume that the solid solution is the most stable at equimolar composition, since the ideal configurational entropy has the largest value for equimolar composition. Yet the dependence of enthalpy on composition may be assymetric for nonideal solutions, and so the Gibbs potential may not have the minimal value at equimolar composition and therefore the role of entropy of mixing in stabilizing solid solution phases might be over-emphasized.

Zhang et al. [Zhang et al., 2014] notes that if the configurational term had an absolutely dominant role in stabilizing the solid solution, the following conclusions could be made: 1) increasing the number of alloying elements N should increase the probability of forming a HEA, 2) different alloys with the same number of alloying elements N should have the same probability of forming a HEA, 3) equal content of alloying elements should always be advantageous over unequal content of alloying elements.

Cantor et al. [Cantor et al., 2004] tried to prepare two alloys consisting of 20, respectively 16 elements in equal proportions. Both of these alloys were brittle and consisted of many phases, but the main phase was an FCC phase enriched in Co, Cr, Fe, Mn and Ni. Subsequently they prepared equimolar CoCrFeMnNi alloy with a FCC single phase. When they tried to enrich this alloy with other elements, no single-phase alloy formed, which shows that simple adding more elements and therefore increasing the ideal configurational entropy may not help in preparing stable single-phase alloys.

The single-phase FCC CoCrFeMnNi alloy was a basis for research of Otto et al. [Otto et al., 2013b] They attempted at replacing one element in this alloy a time with an element of similar properties, but yet again no single-phase alloy was formed.

Miracle and Senkov [Miracle and Senkov, 2017] give an in-depth analysis of the terms contributing to the excess entropy relative to the ideal configurational entropy $S^{ideal,\oslash}$. The excess entropy consists of excess configurational entropy ${}^{conf}S^{\oslash}$ (due to the ordering or lattice distorsion effects), excess entropy due to vibrations of atoms ${}^{vib}S^{\oslash}$, magnetic moments ${}^{mag}S^{\oslash}$ and electronic effects ${}^{elec}S^{\oslash}$. The total molar entropy of the phase $\oslash$ can therefore be expressed as:

$$S^{\oslash} = S^{ideal,\oslash} + {}^{conf}S^{\oslash} + {}^{vib}S^{\oslash} + {}^{mag}S^{\oslash} + {}^{elec}S^{\oslash}. \tag{1.14}$$

The difference between the net molar entropy for SS and IM phase is thus

$$\begin{aligned}\Delta S^{SS-IM} = &\left(S^{SS,ideal} - S^{IM,ideal}\right) + \left({}^{conf}S^{SS} - {}^{conf}S^{IM}\right) + \\ &+ \left({}^{vib}S^{SS} - {}^{vib}S^{IM}\right) + \left({}^{mag}S^{SS} - {}^{mag}S^{IM}\right) + \\ &+ \left({}^{elec}S^{SS} - {}^{elec}S^{IM}\right).\end{aligned} \tag{1.15}$$

Entropy curves of binary liquid alloys given in the literature use pure elements as the standard state. The entropy of pure elements ${}^{\circ}S^{\oslash}$ needs to be added to such

values. The first two terms in equation 1.14 are zero for pure elements and the vibrational term is the largest out of the others. Therefore ${}^{\circ}S^{\oslash}$ can be reasonably approximated by ${}^{vib}S^{\oslash}$. The vibrational entropy ${}^{vib}S^{\oslash}$ can then be calculated as

$$ {}^{vib}S^{\oslash} = \int_0^{T_0} \frac{C_v^{\oslash}}{T} dT, \tag{1.16} $$

where $C_v^{\oslash}$ is the molar heat capacity of element $\oslash$ at constant volume and T is the absolute temperature. The calculation of alloy entropy is then based on Kopp's rule, which says that alloy entropies can be approximated as a linear average of the elemental entropies.
In this way they obtained total molar entropies of binary liquid alloys S^{liquid} for a number of binary alloys. The results showed that S^{liquid} was over an order of magnitude larger than $S^{\oslash,ideal}$ and that the largest contribution to this term was the vibrational term of pure elements. But the difference ${}^{vib}S^{SS} - {}^{vib}S^{IM}$ still does not have to be large. In one study, as they noted, this difference was determined experimentally to be around $0,1R$.
After subtracting the vibrational entropy of pure elements, the equation for total molar entropy can be written as follows:

$$ S^{\oslash} - {}^{vib}S^{\oslash} = S^{ideal,\oslash} + {}^{conf}S^{\oslash} + {}^{vib}S^{\oslash,remnt} + {}^{mag}S^{\oslash} + {}^{elec}S^{\oslash}, \tag{1.17} $$

where ${}^{vib}S^{\oslash,remnt}$ is the remnant vibrational entropy term that corresponds to the part of vibrational entropy that is not approximated well by the Kopp's rule. The total molar entropy after subtraction of vibrational entropy of pure elements as a function of composition for some representative binary systems is plotted in figure 1.4. It is clear that the excess terms may be significant and that the ideal configurational term may not be the dominant factor.

1.3.2 The lattice distortion effect

In conventional alloys, most lattice sites have the same kind of atoms as their neighbours, which does not cause large lattice distortions. On the other hand, the crystal lattice in concentrated alloys can be significantly distorted when the alloying elements have different sizes, different bonding types and different crystal structure tendencies. This distorsion is claimed to be larger in high entropy alloys than in other types of alloys. Murty et al. [2019]
The consequences of the lattice distorsions are claimed to be a decrease in intensity of X-ray diffraction peaks, an increase of hardness and a reduction of electrical and thermal conductivity. Systematic studies of these effects are lacking and it is therefore not clear to what extent these characteristics may be influenced by other phenomena. Miracle and Senkov [2017] However, explanation of the properties listed above based on lattice distortion were given in the literature as follows.
HEAs with body-cented cubic structure (BCC) appear to show smaller solution hardening than HEAs with face-centered cubic structures (FCC). This could be explained by the fact that each site in FCC structures has 12 nearest neighours, whereas in BCC structures each site has only 8 nearest neighbours (with 6 next-nearest neighbours that are more distant than next-nearest neighbours in FCC). It has been proposed that the vicinity of atoms in FCC structures will be more distorted, as the atoms have closer neigbouring sites than in BCC structures.

Figure 1.4: The total molar entropies of binary liquid alloys. Taken from [Miracle and Senkov, 2017]

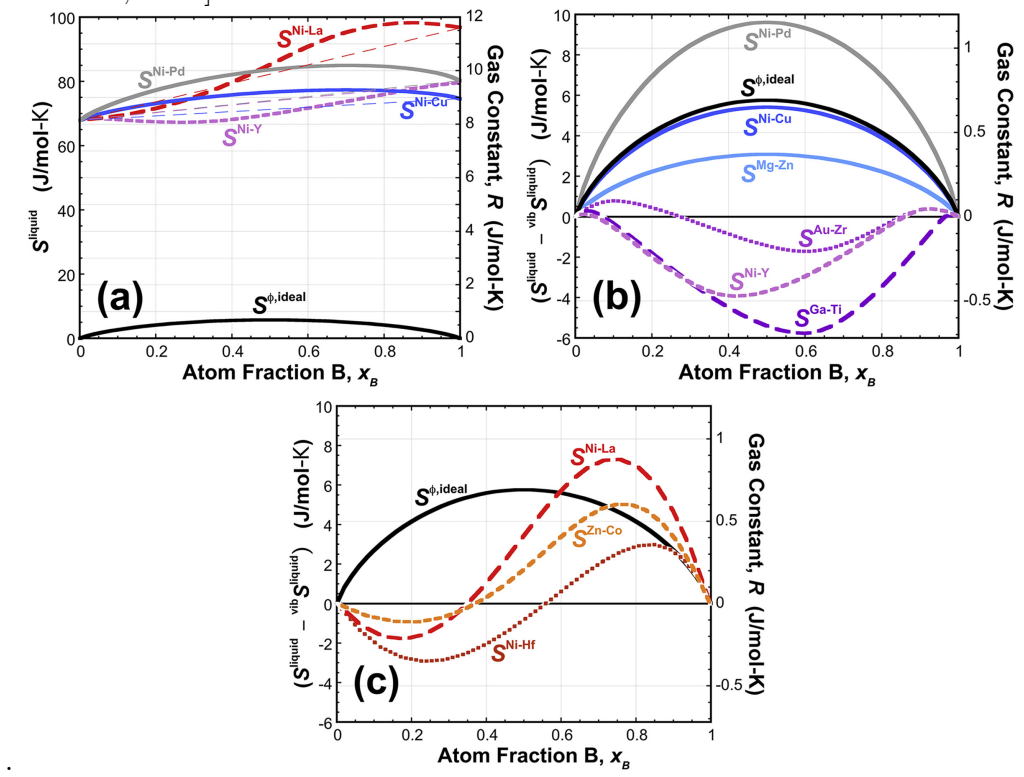

This should support the claim that higher hardness can be attributed to larger lattice distortion. Murty et al. [2019]

Larger diffuse scattering of X-rays and electrons at distorted lattice may explain less sharp X-ray diffraction peaks and decrease in electrical conductivity. These effects are independent of temperature, which is indicative of smaller impact of phonon scattering and seem to support the lattice distortion hypothesis. Murty et al. [2019]

The theory of ideal solutions assumes that all lattice sites are occupied by equal-sized, yet chemically different atoms. Significant lattice distorsion caused by atoms of different sizes in HEAs should therefore contribute to the excess configurational entropy. Correspoding calculations have been attempted for metallic glasses, but not yet for HEAs. [Miracle and Senkov, 2017]

When it comes to enthalphy, following considerations have been published. The coordination numbers are usually 12 for FCC and HCP structures and 14 for BCC structures. Coordination numbers in systems with unequal-sized atoms can singnificantly differ. Coordination numbers smaller than 12 are common for smaller atoms and coordination numbers larger than 12 are common for bigger atoms. But in systems with unequal-sized atoms both smaller and larger atoms coexist and therefore the average coordination number will fall in the range of around 12 to 14. Moreover, is has been proposed that the bond enthalpy decreases when the number of bonds increases. As a result the enthalpy in HEAs may not differ from classical thermodynamic models due to lattice distortion. Miracle and Senkov [2017]

1.3.3 The sluggish diffusion effect

It has been proposed that diffusion is very slow in high entropy alloys, even though experimental evidence is mostly lacking because of the difficulty of measuring diffusion. These claims are usually based on indirect evidence, such as observations of formation of nanocrystals and amorphous phases upon solidification or on theoretical models. [Miracle and Senkov, 2017]
Because each lattice site in HEAs is surrounded by different atoms, each site forms different bonds with neighbouring sites and therefore has different lattice potential energy. If the variation of lattice potential enegy is large enough, low lattice potential energy sites are proposed to serve as traps for diffusing atoms and thus contribute to slower diffusion rates and higher activation energies. [Tsai et al., 2013]
Diffusion coefficients have been measured directly for FCC Co–Cr–Fe–Mn–Ni alloy by Tsai et al. [Tsai et al., 2013] The diffusion was studied at elevated temperatures from 1173 K to 1373 K, where the alloy behaved like ideal solutions. Three couples of samples that differed in the concentration of two elements were used.
The authors claim that diffusion coefficients of the elements in this alloy were indeed smaller than those in the pure FCC metals and Fe–Cr–Ni(–Si) alloys, as predicted by the sluggish diffusion hypothesis. The diffusion rates decreased in the sequence Mn, Cr, Fe, Co and Ni. Measured diffusion coefficients as a function of temperature normalized to the melting temperature are plotted in figure 1.5. The activation energy of the element with the slowest diffusion rate, nickel, was close to the value of activation energy for grain growth in the equimolar Co-Cr-Fe-Mn-Ni alloy.

Figure 1.5: Diffusion coefficients for Mn, Cr, Fe, Co and Ni in various materials normalized to the melting temperature T_m. Taken from [Tsai et al., 2013].

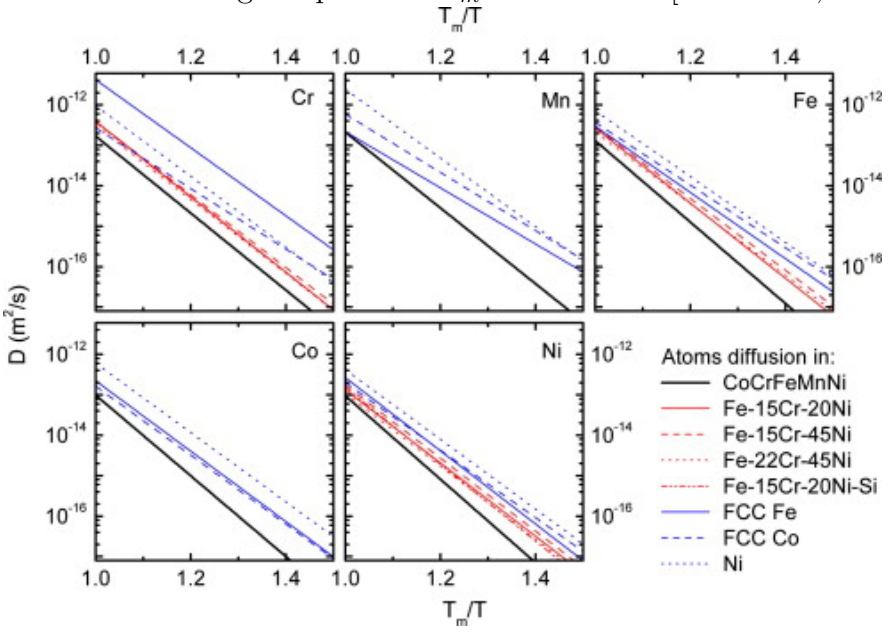

Validity of the conclusions of this study were challenged by Miracle and Senkov in their review paper, where they offered an alternative analysis of the data.

They note that accurate measurement of diffusion coefficients is challenging and differences within one order of magnitude are not considered significant. They claim that the diffusion parameters for Co–Cr–Fe–Mn–Ni do not significantly differ from diffusion coefficients for other FCC metals. They argue that the diffusion coefficient of nickel in studied HEA is in fact *larger* than in austenic steels and pure iron when compared at the same temperature in the temperature range 873 – 1323 K. [Miracle and Senkov, 2017]

1.3.4 The 'cocktail' effect

The term 'cocktail effect' describes the fact that some unusual combinations of elements can result in alloys with very different and surprising properties, even though one would not expect that. This phrase is often used when talking about three kinds of alloys: bulk metallic glasses (amorphous alloys formed at very high cooling rates that exhibit a glass transition), super-elastic and super-plastic metals (metals that can be deformed over about 600% during tensile deformation) and high entropy alloys. Miracle and Senkov [2017]

1.4 Microstructure of HEAs

1.4.1 Composition of HEAs

Miracle and Senkov [Miracle and Senkov, 2017] analyzed 408 different HEAs published by mid-2015. They consist of 37 elements:

- 1 alkali metal - Li
- 2 alkaline earth metals - Be, Mg
- 22 transition metals - Ag, Au, Co, Cr, Cu, Fe, Hf, Mn, Mo, Nb, Ni, Pd, Rh, Ru, Sc, Ta, Ti, V, W, Y, Zn, Zr
- 6 lanthanides - Dy, Gd, Lu, Nd, Tb, Tm
- 3 metalloids - B, Ge, Si
- 1 non-metal - C

Not all of these elements are present often in HEAs. Over 70% of HEAs contain Co, Cr, Fe, Ni. Other common elements are Al, Cu, Mn and Ti, these are present in more than 100 alloys. These alloys are either midle entropy or high entropy alloys according to the entropy definition of HEA. Generaly these alloys can be called complex concentrated alloys (CCAs).
Miracle and Senkov classify CCAs into seven alloy families according to their element content and common properties:

1. *3d transition metal CCAs* are alloys that contain at least 4 of these elements: Al, Co, Cr, Cu, Fe, Mn, Ni, Ti and V. This is the most widely studied family. Miracle and Senkov consider them as extensions of stainless steels and superalloys as austenitic, duplex and precipitation hardened stainless steels all have Fe, Cr and Ni as principal elements.

2. *Refractory metal CCAs* are alloys that contain at least 4 of these elements: Cr, Hf, Mo, Nb, Ta, Ti, V,W, and Zr plus Al. They are studied far less frequently, only 29 of them were reported before mid-2015. They were developed as a result of search for new high temperature structural metals.

3. *Low-density CCA family* are alloys containing Al, Be, Li, Mg, Sc, Si, Sn, Ti and Zn. Only 7 alloys have been reported in this faily. This family was motivated by the need to find new structural metals with low density for aerospace applications.

4. *4f elements CCAs* are alloys containing at least 4 of these elements: Dy, Gd, Lu, Tb and Tm plus Y. The discovery of these alloys was the consequence of a search for single-phase, solid solutions HEA with HCP structure.

5. *CCA brasses and bronzes* are alloys containing Al, Cu, Mn, Ni, Sn and Zn. The alloys in this family are represented by the formula $Al_xSn_yZn_z\,[CuMnNi]_{1-x-y-z}$.

6. *Precious metals CCAs* contain at least 4 of these elements: Ag, Au, Co, Cr, Cu, Ni, Pd, Pt, Rh and Ru.

7. *B, C or N CCAs* are alloys consisting of B, C or N and elements from 3d transition metal or refractory metal CCA families. Most of the alloys are produced as thin films.

1.4.2 Types of microstructure

A wide range of microstructures has been found in CCAs, including amorphous, nanocrystalline, single-phase and multi-phase conditions.
Miracle and Senkov analyzed 648 reports of microstructure of 408 different alloys. [Miracle and Senkov, 2017] The most common phases are disordered (solid solution) FCC phase (found 465 times in 410 alloys) and BCC phase (found 357 times in 306 alloys). Ordered IM phase B2 follows with 177 occurrences in 175 alloys.
All but one single-phase FCC SS alloy either belong to the 3d transition metal family or are ternary alloys of 3d transition metals. This can be ascribed to the presence of FCC-stabilizing elements such as Co, Cu, Mn and Ni. Around 45% of single-phase BCC alloys belong to the refractory metal family, the rest are 3d transition metal CCAs.
The first problem with the preceding statistics is that some alloys were studied in multiple studies, which resultn in multiple reports of microstructure for the same alloy. Moreover, microstructures are often reported (in around 70% cases) in as-cast, non-equilibrium state. Miracle and Senkov claim that post-process annealing of as-cast alloys reduces the percentage of SS alloys and increases the number of (SS + IM) alloys.
Another problem is that the objective of the HEA community is to find single-phase solid solution HEAs, so researchers tend to pre-select elements that are expected to form a signle phase solid solution (possibly according to Hume-Rothery rules). This lead to an interest of the HEA community in 3d transition metal family alloys consisting of elements with extremely small mixing enthalpies. HEA

solid solutions seems to have simple structures because elements from which they consist have almost always simple structures.
The number of reported SS phases might be overestimated as two or more reported phases can be a part of the same phase in hyperdimensional phase diagram. For example, the pairs Cu-Ni and Co-Fe are extended binary solid solutions. It seems that they are different from each other, but CoCuFeNi is also a single-phase solid solution, so there is a possibility that CuNi, CoFe and CoCuFeNi are in fact a part of the same solid solution phase in hyperdimensional composition space. Furthermore, problems can occur when distinguishing between SS and IM phases with similar structure or using inconsistent terminology. [Miracle and Senkov, 2017]

1.5 Mechanical properties of HEAs

Miracle and Senkov [Miracle and Senkov, 2017] note that early studies of properties of HEAs are not entirily reliable since most samples included defects such as casting segregation, dendritic microstructures and residual stresses when being studied. Most alloys that have been studied and therefore their mechanical properties belong to the 3d transition metal alloy family. Results from the refractory metal family of alloys consists mainly of hardness or compression data with very little data from tensile testing.

1.5.1 3d transition metal alloys

Hardness of single-phase FCC $Al_xCoCrCuFeNi$ and $Al_xCoCrFeNi$ alloys has been studied. The hardness of the single-phase FCC alloy is around $100 - 200$HV. As more aluminium is added, the FCC structure changes to a mixture of FCC and BCC phase and the hardness increases. The hardness then rises to around 600HV for single-phase BCC alloy when enough aluminium is added. Yeh et al. [2004a]
Compression tests have been done on alloys containing CoCrFeNi and Al, Cu or Ti. In alloys with significant amount of BCC or B2 phases the compressive yield strength can be quite high from 1300 to 2400 MPa with some values as high as 3300 MPa. Compressive ductilities are often below 10%. Ductility gets worse in alloys with higher volume fraction of IM phases. Miracle and Senkov [2017]
The most studied alloy for tensile properties is CoCrFeMnNi. Miracle and Senkov [2017] The yield and ultimate strengths decrease with increasing temperature with the steepest decrease in the range of 77 to 300 K. The deformation for $\varepsilon < 2.4\%$ occurs by planar dislocation glide on $1/2 < 110 > \{111\}$ slip system. After plastic strains $\varepsilon > 20\%$ at $T = 300\,\mathrm{K}$, dislocations lose their planar character and organize into cell structures. This behaviour is usual for FCC metals. Below RT both tensile strength and tensile ductility is increased by nano-twinning. Otto et al. [2013a]
Increasing strength and decreasing ductility with increasing Al content have been reported in equimolar CoCrFeMnNi and similar 3d transition metal alloys such as $Al_x(CoCrFeMnNi)_{100-x}$. He et al. [2014] Decreasing the amount of Cr leads to decrease in strength, but increasing the amount of Cr above 26 at.% leads to strengthening due to the formation of the σ phase. Zaddach et al. [2015]

Content of other elements does not seem to have such a big influence on mechanical properties – the properties of other quaternary and ternary equimolar alloys based on Co-Cr-Fe-Mn-Ni do not significantly differ from those for the equimolar CoCrFeMnNi alloy (as long as Cr is retained). Miracle and Senkov [2017]
Strength of 3d metals family HEAs is not particularly high, it is comparable with strengths of stainless steels. Representative data on compression characteristics is given in figure 1.6. Strengthening can be achieved by work-hardening or grain refirement, precipitation hardening is not well studied yet. Work-hardening occurs at all temperatures below 1000 K and is especially strong below RT. Thermally activated flow at temperatures above 1000K produces a drop in strength. Miracle and Senkov [2017]

Figure 1.6: Tensile data of 3d transition metal alloys and selected commercial steels and nickel superalloys. Taken from [Miracle and Senkov, 2017].

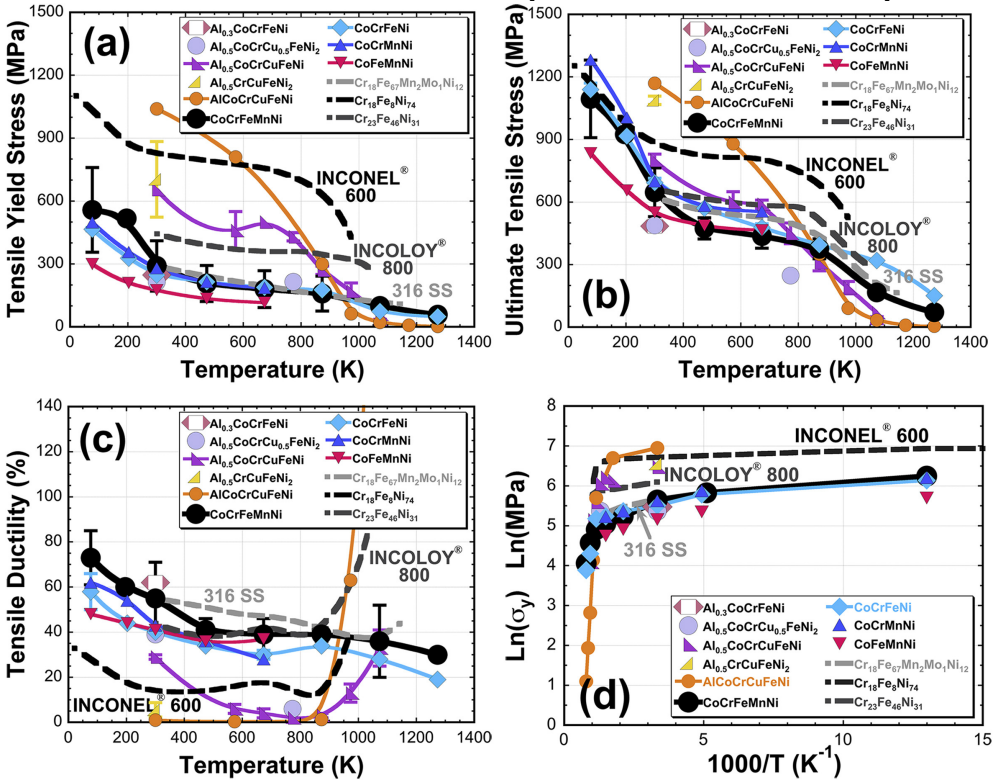

The 3d transition metal family alloys contituting from Nb and Sn contain IM phases. Strength increases and ductility decreases by adding more Nb or Sn. The change is caused by the increase of the volume fraction of IM phases. When the IM phase dominates, the ductility is lost, the alloy becomes very brittle. Liu et al. [2012], Liu et al. [2013a], Liu et al. [2015]

1.5.2 Refractory metal alloys

Microstructures of refractory metal family alloys typically consist of one or more BCC phases. Properties of elemental constituents of refractory metal alloys are different, which is reflected in the fact that refractory metal HEAs have larger span of mechanical properties. Miracle and Senkov [2017]

Representative data on compression characteristics is given in figure 1.7. Compressive yield stress decreases with rising temperature with a significant drop at around 1000 K. MoNbTaW and MoNbTaVW have high strengths at elevated temperatures of around 2000 K, but both have high density and show a brittle to ductile transition between RT and 1000 °C. Senkov et al. [2011b] This motivated alloys with lighter elements like Cr, Ti, V and Zr. For example, $AlMo_{0.5}NbTa_{0.5}TiZr$ has the density of $\rho = 7,400\,\mathrm{kg \cdot m^{-3}}$, the highest RT yield strength σ_y and yield strength ratio to density σ_y/ρ measured to date and 10% compressive RT ductility. Senkov et al. [2014] Refractory metal alloys have potential for high temperature industry applications.

Figure 1.7: Tensile data of refractory metal HEAs and selected commercial steels and nickel superalloys. Taken from [Miracle and Senkov, 2017].

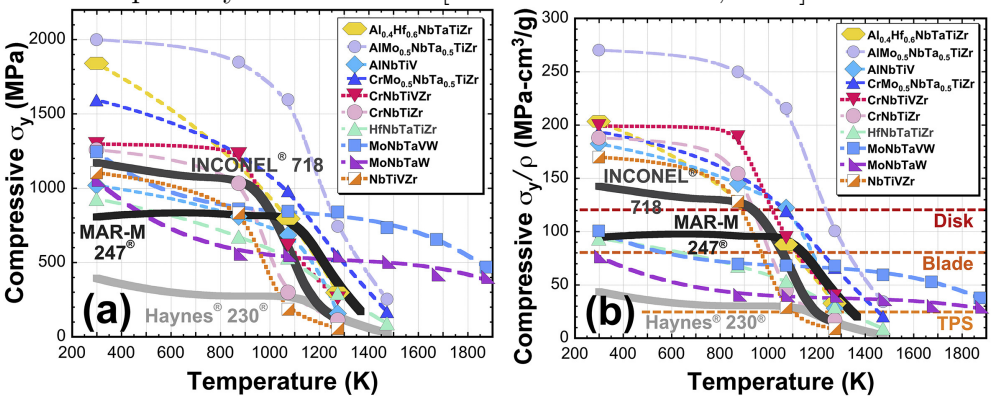

2. Characterisation methods

2.1 Positron anihilation techniques

2.1.1 Source of positrons

As a source of positrons usually β^+ emmiters are used. A radioisotope ${}^A_Z X$ decays via β^+ emission into the isotope ${}^A_Z X'$, a positron e^+ and a neutrino ν:

$$ {}^A_Z X \rightarrow {}^A_{Z-1} X' + e^+ + \nu. \tag{2.1}$$

The spectrum of kinetic energies of positrons generated by β^+ decay is continuous. The energy spectrum for positrons emitted by ^{22}Na radioisotope as simulated by Geant4 Agostinelli et al. [2003] is in the figure 2.1. The average energy is around 0.215 MeV and the maximum positron energy (end-point-energy) lies at around 0.54 MeV.

Figure 2.1: Energy spectrum of positrons from β^+ decay of sodium-22 simulated by Geant4. Taken from [Li et al., 2020].

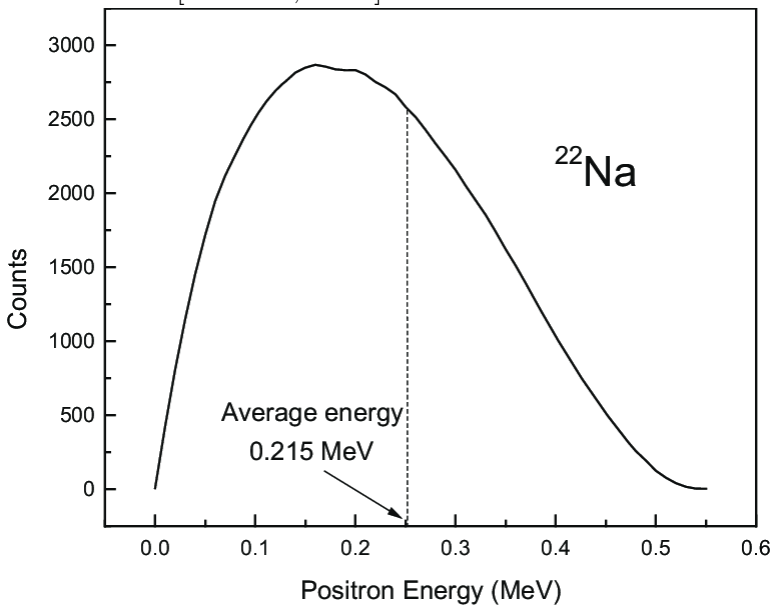

The most commonly used radioisotope is sodium ${}^{22}_{11}$Na with a half-life of 2.6 years. It decays into stable neon ${}^{22}_{10}$Ne, but only about 0.06 % of the sodium atoms decay directly into the ground state of neon nucleus. The rest decays into an excited state of neon ${}^{22}_{10}$Ne*. The excited state of neon has a lifetime of 3.7 ps and passes into the ground state while emitting a 1275 keV gamma ray.
Positron source commonly used in experiments is made by pouring a few drops of ^{22}NaCl solution on a very thin foil with thickness of a few micrometers, evaporating it and covering it by another piece of the foil. Čížek [1999]

2.1.2 Thermalization of positrons in solids

When a positron enters a solid, its kinetic energy is in the order of hundreds of kiloelectronvolts. It starts to lose its energy very quickly in tree subsequent steps.

In the first step, a positron loses its energy by collisions with inner electrons of the host atoms. The first step lasts for around 1 ps.
When the positron has reached an energy in the range of 10 eV, the main dissipation process is excitation of conduction electrons. This second step lasts for periods in the order of 1 ps. When the energy of the positron is on the order of fractions of electronvolts, the positron dissipates energy by scattering on phonons. The last third step takes the longest time, it can last for a few picoseconds. Čížek [1999]

2.1.3 Implantation profile

The probability density function $P(x)$ that a positron penetrated to the depth x below the surface decays exponentially:

$$P(x) = \alpha_+ e^{-\alpha_+ x}. \tag{2.2}$$

The coefficient α_+ can be approximated using the following equation:

$$\frac{1}{\alpha_+}\ [\mathrm{cm}] \simeq \frac{E_{max}^{1.4}\ [\mathrm{MeV}]}{16\rho\ [\mathrm{g \cdot cm^{-3}}]}, \tag{2.3}$$

where ρ is the density of the material given in $\mathrm{g \cdot cm^{-3}}$ units and E_{max} is the maximum kinetic energy of the positrons leaving the source, i.e. the end-point-energy, expressed in MeV. After plugging in typical values for metals one can clearly see that positrons can reach sufficient depth in the order of tens of hundreds microns, so the positron annihilation techniques can be used to test bulk properties of materials. Čížek [1999]

2.1.4 Thermalized positrons

Thermalized positrons undergo random diffusion motion with diffusion coefficients in the order of 0.1 to 2 $\mathrm{cm^2 s^{-1}}$. Due to the scattering on phonons the temperature dependence of the diffusion coefficient D_+ is

$$D_+ \sim \frac{1}{\sqrt{T}}. \tag{2.4}$$

The mean free path of positron between scattering events with the phonons l_+ is given by the equation

$$l_+ = \sqrt{D_+ \tau_{ph}}, \tag{2.5}$$

where τ_{ph} is the relaxation time of scattering of positrons on phonons. Since the relaxations time τ_{ph} for metals is in the order of femtoseconds, the mean free path is in the order of nanometers.
The mean distance from the place of positron thermalisation to the place where it is located just before its annihilation is the mean positron diffusion length L_+. It is given by the equation

$$L_+ = \sqrt{D_+ \tau_I}, \tag{2.6}$$

where τ_I is the lifetime of delocalized positron. For metals L_+ is in the order of hundreads of nanometers.
The wavelength of thermalized positron is given by the equation

$$\lambda_+ \text{ [nm]} = \frac{h}{m^* v_+} \simeq 5.2\sqrt{\frac{293 \text{ [K]}}{T \text{ [K]}}} \tag{2.7}$$

and it is larger than interatomic spacing. Therefore we speak about free or delocalized positrons in solids. The volume $\lambda_+^2 L_+$, which is explored by positron during its lifetime is occupied by $\sim 10^7$ atoms. Čížek [1999]

2.1.5 Positron annihilation and lifetime experiments

Nearly immediately after the decay of sodium-22 a photon with eneregy 1274 keV is emitted. This photon serve the purpose of start signal, i.e. it provides information that a positron was born. Then the positron enters the solid and is thermalized by the processes described in the preceding sections. After being thermalised, the positron annihilates with an electron. Two gamma rays are emitted upon annihilation. Let us denote the energies of the photons as E_1 and E_2. Then the following relation holds:

$$E_1 + E_2 = \sqrt{m_0^2 c^4 + p_-^2 c^2} + \sqrt{m_0^2 c^4 + p_+^2 c^2} - E_B, \tag{2.8}$$

where $m_0 c^2$ is the rest energy of the electron, p_- is the momentum of the electron, p_+ is the momentum of the positron and E_B is the binding energy of the electron. If we assume that both the electron and the positron has zero momentum just before annihilation, then the energy of both emitted gamma rays is exactly $m_0 c^2 = 511$ keV. The photons are then emitted in exactly opposite directions.
One of these photons is registered and serves as stop signal. The lifetime of the positron is the time it passes between registration of the start and the stop signal. Čížek [1999]

2.1.6 Annihilation of free positron

The lifetime of a free positron τ_B is given by the inverse of the annihilation rate λ_B:

$$\tau_B = \frac{1}{\lambda_B}. \tag{2.9}$$

The annihilation rate λ_B is given by the equation

$$\lambda_B = \pi r_e^2 c \hat{n}_-, \tag{2.10}$$

where r_e is the classical radius of electron given in terms of the elementary charge e and the permittivity of vacuum ε_0 as

$$r_e = \frac{e^2}{4\pi\varepsilon_0 m c^2} \tag{2.11}$$

and $\hat{n}_-$ can be calculated as

$$\hat{n}_- = \int n_+ (\boldsymbol{r}_+) \, n_- (\boldsymbol{r}_+) \, \gamma (\boldsymbol{r}) \, \mathrm{d}^3 \boldsymbol{r}, \tag{2.12}$$

where $n_+ (\boldsymbol{r}_+)$ is the positron density, $n_- (\boldsymbol{r}_+)$ is the electron density and γ is an enhancement factor accounting for the increased electron density in the vicinity of the positron caused by the coulombic and exchange-correlation interaction. Čížek [1999]

2.1.7 Annihilation model for defect-free material

Let us assume that a positron at time $t = 0$ enters a metal without defects. The probability $n(t)$ that at time t the positron has not annihilated yet is the solution of the following differential equation:

$$\frac{\mathrm{d}n(t)}{\mathrm{d}t} = -\lambda_B n(t), \tag{2.13}$$

where λ_B is the bulk annihilation rate of the free positron. The solution of equation 2.13 is an exponential function:

$$n(t) = \mathrm{e}^{-\lambda_B t}. \tag{2.14}$$

In positron experiments we measure numbers of positrons annihilated at various time intervals. The ideal spectrum of positron lifetimes in solids should be of the following form:

$$S_{id}(t) = -\frac{\mathrm{d}n(t)}{\mathrm{d}t} = \lambda_B \mathrm{e}^{-\lambda_B t}. \tag{2.15}$$

The bulk positron lifetime is then

$$\tau_B = \frac{1}{\lambda_B}. \tag{2.16}$$

Čížek [1999]

2.1.8 Annihilation model for material with one type of defects

Let us now assume a case of material with single type of defect in which positrons can get trapped. The probability that at time t the positron is in the free state, delocalized in the lattice, shall be denoted $n_B(t)$. The probability that at time t the positron is trapped in the defect shall be denoted $n_D(t)$. As before, $n(t)$ is the probability that at time t the positron has not been annihilated yet. Because a positron that has not been annihilated yet can be present only in the free state or trapped in the defect, the following equation obviously holds:

$$n(t) = n_B(t) + n_D(t). \tag{2.17}$$

Thermalized positrons can annihilate either in the free state with annihilation rate λ_B or in trapped state at defects with annihilation rate λ_D. The annihilation rate

λ_D is different for each type of defect and each type of material. Finally, let us denote K_D the probability that a positron gets trapped in the defect.
The conventional trapping model describing kinetics of positron trapping in a material with single type of defects is based on the following assumptions:

1. only thermalised positrons can be trapped in the defect,
2. trapped positrons cannot escape from the defect and come back into the free state
3. defects are distributed randomly in the material.

Making these assumptions, one can write down the following differential equations for probabilities of annihilation in the free or trapped state:

$$\frac{\mathrm{d}n_B(t)}{\mathrm{d}t} = -\left(\lambda_B + K_D\right) n_B(t) \tag{2.18}$$

$$\frac{\mathrm{d}n_D(t)}{\mathrm{d}t} = -\lambda_D n_D(t) + K_D n_B(t), \tag{2.19}$$

where K_D is the positron trapping rate, which represents the probability that a positron gets trapped in the defect.
The initial conditions are as follows:

$$n_B(t=0) = 1 \tag{2.20}$$

meaning that at the instant the positron enters the material it is not annihilated yet and

$$n_D(t=0) = 0 \tag{2.21}$$

meaning that at the instant the positron enters the material it is not trapped in defect yet.
The solution of the set of differential equations 2.18 and 2.19 is as follows:

$$n_B(t) = \mathrm{e}^{-(\lambda_B + K_D)t} \tag{2.22}$$

$$n_D(t) = \frac{K_D}{\lambda_B + K_D - \lambda_D}\left[\mathrm{e}^{-\lambda_D t} - \mathrm{e}^{-(\lambda_B + K_D)t}\right]. \tag{2.23}$$

The ideal spectrum can then be calculated as

$$S_{id} = -\frac{\mathrm{d}n(t)}{\mathrm{d}t} = -\frac{\mathrm{d}\left(n_B(t) + n_D(t)\right)}{\mathrm{d}t} = \lambda_I I_I \mathrm{e}^{-\lambda_I t} + \lambda_{II} I_{II} \mathrm{e}^{-\lambda_{II} t}, \tag{2.24}$$

where

$$\lambda_I = \lambda_B + K_D \tag{2.25}$$

$$\lambda_{II} = \lambda_D. \tag{2.26}$$

The ideal spectrum consists of two exponential components with lifetimes τ_I, τ_{II} and intensities I_I, I_{II} given by the following relations:

$$\tau_I = \frac{1}{\lambda_I} = \frac{1}{\lambda_B + K_D}, \tag{2.27}$$

$$\tau_{II} = \frac{1}{\lambda_{II}} = \frac{1}{\lambda_D}, \tag{2.28}$$

$$I_{II} = \frac{K_D}{\lambda_I - \lambda_D} = \frac{K_D}{\lambda_B + K_D - \lambda_D}, \tag{2.29}$$

$$I_I = 1 - I_{II}. \tag{2.30}$$

Čížek [1999]

2.1.9 Determination of defect concentration

From equations 2.27 - 2.30 the positron trapping rate K_D can be isolated:

$$K_D = I_2 \left(\frac{1}{\tau_1} - \frac{1}{\tau_2} \right). \tag{2.31}$$

The positron trapping rate K_D is proportional to the concentration of defects in the material c_D:

$$K_D = \nu_D c_D, \tag{2.32}$$

where ν_D is the specific positron trapping rate specific to given kind of defects. It represents the positron trapping rate per unit concentration of defects. Typical values of the specific positron trapping rate for vacancies in metals are in the order of 10^{14}–$10^{15}\mathrm{s}^{-1}$ at., for dislocations in metals it is in the order of 10^{-5}–$10^{-4}\mathrm{m}^2\mathrm{s}^{-1}$. Providing that the specific positron trapping rate is known or has been estimated, one can subsequently determine the concentration of the defects from positron lifetime measurement.
With increasing concentration of defects, the lifetime of the second component τ_2 remains constant, but intensity of the component belonging to trapped positrons rises. The lifetime of the first component τ_1 decreases with increasing concentration of defect. If K_D is much larger than λ_B, practically all positrons annihilate in the trapped state and the lifetime τ_I and the intensity I_1 decrease to zero. This is called saturated positron trapping. The determination of the defect concentration using the conventional trapping model is then not possible and one can get only a lower limit of defect concentration. Čížek [1999]

2.1.10 Assumptions of conventional trapping model

The conventional trapping model is based on the following assumptions:

1. only thermalised positrons can be trapped at defects,
2. trapped positrons cannot escape defect and come back into the free state
3. defects are distributed randomly in the material.

To test these assumptions it is useful to use the τ_f parameter defined as

$$\tau_f = \left(\frac{I_1}{\tau_1} + \frac{I_2}{\tau_2}\right)^{-1}. \tag{2.33}$$

If τ_f lifetime agrees with the bulk lifetime τ_B of delocalised positrons in well annealed (defect-free) material, it means that the assumptions of conventional trapping model are reasonably satisfied in the material studied. Čížek [1999]

2.1.11 Real positron lifetime spectrum

The real positron lifetime spectrum we obtain while performing experiment is the convolution of the ideal spectrum $S_{id}(t)$ and the resolution function of the spectrometer R, to which we need to add the background B from random coincidences:

$$S(t) = S_{id}(t) * R(t) + B, \tag{2.34}$$

where the symbol $*$ denotes convolution. The ideal spectrum is a sum of the following exponential components:

$$S_{id}(t) = \sum_i \lambda_i I_i \mathrm{e}^{-\lambda_i t}. \tag{2.35}$$

A typical spectrum obtained in a positron lifetime experiment is shown in figure 2.2.

Figure 2.2: A typical postron lifetime spectrum. The measured spectrum and the resolution function of the spectrometer are shown. Taken from Tuomisto and Makkonen [2013].

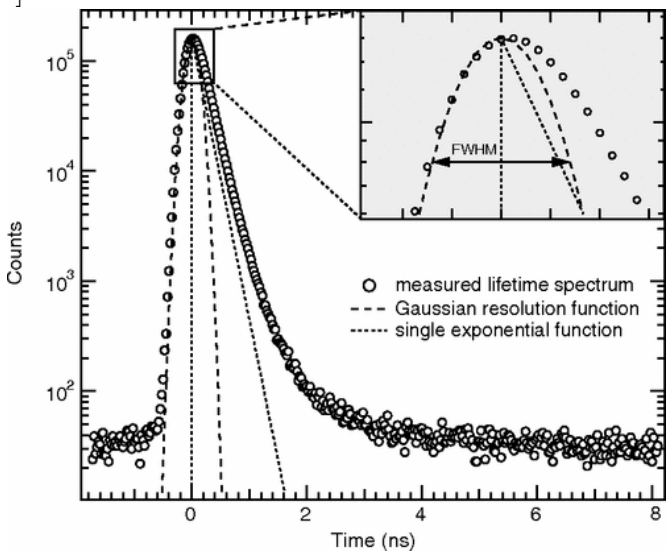

To obtain information about defects, the measured spectrum needs to be decomposed into exponential components of the form written in equation 2.35. The number of components is not known beforehand and the sole mathematical problem concerning decomposition of the measured spectrum into exponential components is rather difficult. Besides in the ideal spectrum consisting of several

exponential components there are usually at least two other components due to positron annihilation in the ^{22}NaCl source and in thin foil covering the source. As a further complication, the resolution function of the spectrometer can never be exactly defined. Čížek [1999]

2.1.12 Doppler broadening of annihilation peak

The energies E_1 and E_2 of the gamma rays emitted when a positron and an electron annihilate are interconnected by the following equation:

$$E_1 + E_2 = \sqrt{m_0^2c^4 + p_-^2c^2} + \sqrt{m_0^2c^4 + p_+^2c^2} - E_B, \tag{2.36}$$

where m_0c^2 is the rest energy of the electron, p_- is the momentum of the electron, p_+ is the momentum of the positron and E_B is the binding energy of the electron in the material.
The momentum of the positron p_+ is very small when the positron is thermalized, i.e. $p_+ \approx 0$. If we assume that $p_-c \ll m_0c^2$, then the energies of annihilation gamma rays are

$$E_1 = m_0c^2 - \frac{E_B}{2} + \Delta E \tag{2.37}$$

$$E_2 = m_0c^2 - \frac{E_B}{2} - \Delta E, \tag{2.38}$$

where ΔE is the Doppler shift in energy of annihilation gamma rays due to the momentum of the electron. It can be shown that the Doppler shift in energy is directly proportional to the component of the electron momentum that is parallel to the direction of the gamma ray emission p_L:

$$\Delta E = \frac{p_Lc}{2}. \tag{2.39}$$

The deflection θ of annihilation gamma rays from anti-collinearity is directly proportional to the component of the electron momentum that is transversal to the direction of the gamma ray emission p_T:

$$\theta = \frac{p_T}{m_0c}. \tag{2.40}$$

Čížek et al. [2010]

2.1.13 Coincidence Doppler broadening spectroscopy

The coincidence Doppler broadening spectroscopy (CDB) is based on simultaneous measurement of energies of both annihilation gamma rays E_1 and E_2. In positron lifetime experiments only one of these annihilation gamma rays is detected. If the annihilating positron is thermalised, than the following relations hold:

$$E_1 - E_2 = 2\Delta E = p_Lc \tag{2.41}$$

$$E_1 + E_2 = 2m_0c^2 - E_B. \tag{2.42}$$

As one can see from the first of these equations, from the Doppler shift of the annihilation gamma ray energies the longutidinal momentum of the annihilating electron-positron pair p_L can be determined. Since momentum of thermalized positron is negligible, the momentum of annihilating electron-positron pair is determined mainly by the momentum of electron.
Coincidence measurement of both annihilation gamma rays significantly reduces background noise, which usually consists of single photon events only. As a consequence coincidence measurement reduces background by three orders of magnitude and even high-momentum part of the spectrum can be easily distinguished. The high-momentum part of the spectrum is due to positron annihilations with core electrons, which remain located in atomic orbitals and are almost not affected by the crystal bonding, and therefore give information on the chemical elements surrounding positron annihilation site.
Results of CDB experiments are usually expressed using so-called CDB ratio curves. The CDB curve is obtained by diving the measured spectrum by a spectrum measured for a well-defined reference sample Čížek et al. [2010]

2.1.14 Line shape parameters

To quantify the contribution of the core and valence electrons to the momentum distribution, the so-called S and W line shape parameters are used. The S parameter is the area of the central part of the annihilation peak (divided by the total area under the whole peak), see figure 2.3. The integration limits are chosen so that a similar integration on a reference sample gives the S parameter equal to 0.5. The S parameter is a measure of the contribution of the low momentum conductive and valence electrons. Positrons trapped in open-volume defects predominantly annihilate with such electrons, and therefore the S parameter is increased in materials with open volume defects.
The W parameter is the area under the wings of the annihilation photo-peak (divided by the total area under the whole peak). The integration limits are chosen so that a similar integration on a reference sample gives the W parameter close to 0.03. The W parameter is a measure of the contribution of the high momentum core electrons and is therefore decreased in presence of defects. As it depends on core electrons, it provides extra information on the local chemical environment of the annihilation site.
In presence of more type of defects, each defect contributes to the resulting total S and W parameters according to the following equations:

$$S = \eta_B S_B + \sum_i \eta_{D_i} S_{D_i} \tag{2.43}$$

and

$$W = \eta_B W_B + \sum_i \eta_{D_i} W_{D_i}, \tag{2.44}$$

where the first term on the right side corresponds to the annihilation of free positrons and the terms in the sum correspond to the annihilation of positrons trapped in various types of defects. Hautojärvi [1979]

Figure 2.3: Annihilation photo-peaks broadened by the Doppler shift of the annihilation gamma rays and the depiction of the area from which the S parameter (on the left) and W parameter (on the right) are calculated.

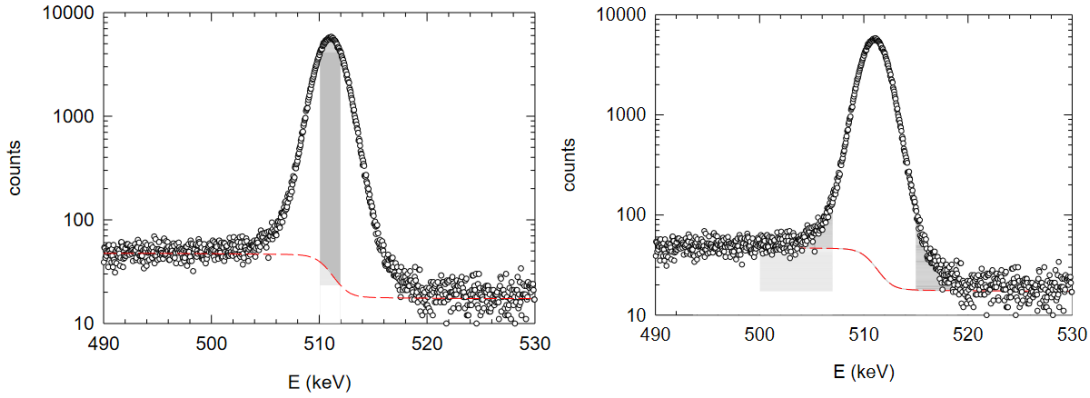

2.2 Scanning electron miscroscopy

2.2.1 Electron beam and electron scattering in the sample

The source of electrons in a scanning electron microscope can be a tungsten filament, but more commonly LaB_6 crystal. The maximum accelerating voltage of emitted electrons is around 30 keV. The probe scans the sample in two perpendicular directions.

When electrons from the incident beam enter the solid, they can be scattered both elastically (by electrostatic interaction with the nuclei) and inelastically (by interaction with atomic electrons).

Backscattered electrons are incident electrons that were elastically scattered to angle higher than 90 degrees. They lose only a small fraction of kinetic energy and therefore have a high chance of leaving the sample be detected and contributing to the back-scattered (BSE) signal.

Secondary electrons are atomic electrons ejected from the specimen as a result of inelastic scattering of incident electrons of the electron beam. Inelastic scattering can take away a significant portion of the incident electron energy. Inelastically scattered incident electrons can be stopped and absorbed in the sample. The electron range R is the maximum range incident electrons can reach before being stopped and absorbed. The secondary electrons which escape from the sample and are detected contribute to the secondary electron (SE) signal. Egerton [2005]

2.2.2 Penetration depth

The electron range R in solids can be approximated by the following formula:

$$\rho R \approx a E_0^r, \tag{2.45}$$

where ρ is the density of material, $r \approx 1.35$, $a \approx 10\,\mu\mathrm{g} \cdot \mathrm{cm}^{-2}$ and E_0 is the energy of the electrons in kiloelectronvolts. The coefficient a is roughly independent of the atomic number Z. The strong dependence of R on Z is reflected in the formula by the fact that solids with higher Z tend to have larger densities. Physically,

this dependance is caused by high-angle elastic scattering of electrons deplating the incident electron beam. It can be shown that the total probability of elastic scattering of an electron at to angle larger than α is given by the equation

$$P_e = \frac{\rho t Z^2 e^4}{16\pi\varepsilon_0^2 u E_0^2 \alpha^2 A}. \tag{2.46}$$

This probability is proportional to the second power of Z, and therefore in solids with larger R many electrons are scattered before penetrating deep into the material.
The range rapidly decreases with decreasing energy of the electrons E_0. Low energy electrons can come to a halt after fewer inelastic collisions and the probability of an inelastic collision is inversely proportional to the energy E_0. Egerton [2005]

Figure 2.4: Simulation of penetration of electrons with incident energy of 20 keV to HfNbTaTiZr alloy created using the CASINO simulation program. Red curves correspond to trajectories of backscattered electrons. Hovington et al. [1997] Drouin et al. [2007]

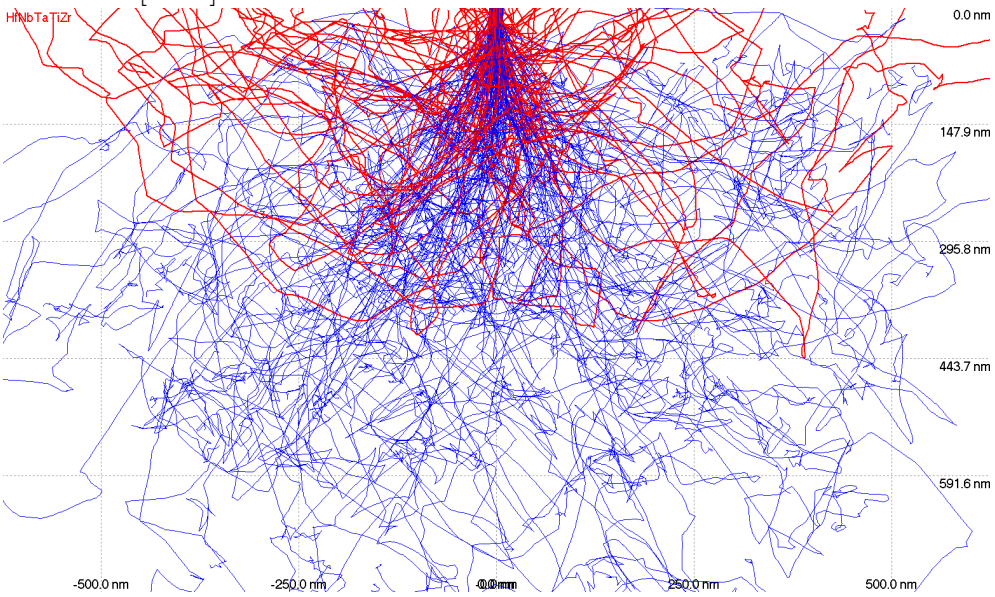

2.2.3 Secondary electron signal

If incident electron scatter inelastically, only a small fraction of their energy is used for release of secondary electrons. Most of the energy of the incident beam transforms into the kinetic energy of the secondary electrons. The secondary electrons therefore wander through the solid and can be subsequently scattered inelastically. Since the probability of inelastic scattering is inversely proportional to the energy, most secondary electrons travels only a few nanometers or less (the starting energy is around 100 eV or less). Hence, only secondary electron emitted near the surface can escape from the sample. Therefore the secondary electron signal gives us information on surface topology of the sample.
The secondary-electron yield δ is defined as the number of released secondary electrons per one incident electron. Its values lie usually somewhere between

0.1 and 10. The secondary-electron yield depends on the energy of the incident electrons (decreases with increasing E_0), the angle between the electron beam and the surface, and on the chemical composition of the sample. The yield is smallest for the normal incidence and increases with decreasing angle between the beam and the sample surface. Let the secondary-electron yield for normal incidence be $\delta(0)$, the angle between the normal to the surface and the electron beam is φ and the corresponding secondary-electron yield is $\delta(\varphi)$. Than it can be showed that the following relation holds:

$$\delta(\varphi) = \frac{\delta(0)}{\cos\varphi}. \tag{2.47}$$

This variation of the secondary-electron yield is responsible for topographical contrast - we can distinguish features on the sample surface that differ in height and shape. Apart from the angular dependence of the secondary-electron yield the topographical contrast is affected by the position of the secondary electron detector - the dector is not usually directly over the sample, so features that are tilted towards the detector look brighter. As a result the image reconstructed from the secondary electron signal looks like a 3D image.
To enhance the secondary electron signal, the Everhart-Thornley detector is often used. It includes a wire-mesh electrode biased positively by a few hundred volts that attract the secondary electrons. After they have passed through the grid, they are accelerated towards a scintillator positively biased by several thousand volts. The scintillator is a material capable of cathodoluminescence, which means that it emits around a hundred of visible photons upon absorption of an electron. The photons are then lead to a photomultiplier tube. The entrance of the photomultiplier tube is coated with a material with low electron work function that serves as a photocathode. Low energy electrons emitted from the photocathode are accelerated toweards a series of dynodes. At each dynode up to ten electrons per each incoming photoelectron are emmited. This whole process results in high amplification with little noise. Egerton [2005]

2.2.4 Backscattered electron images

Backscattered electrons are incident electrons that were elastically scattered to angles higher than 90 degrees either after a single scattering event, or after a series of collisions at scattering angles lower than 90 degrees. The backscattered electrons lose only a small fraction of their energy during collisions, and therefore they have nearly the same energies as the electrons in the incident electron beam. If the electron loses too much energy during collisions, it does not have enough energy to leave the sample and is absorbed into the material. Therefore the backscattered-electron signal gives information only from the depths of about half of the electron penetration depth.
The cross section for elastic scattering is strongly dependent on the atomic number of the sample. In practise, the fraction of incident electrons that escape as backscattered electrons increases approximately linearly with increasing atomic number Z (for low Z). Therefore backscattered electron signal contains information on chemical composition of the sample.
By making the bias on the first grid of the detector negative, we can ensure

that it will repel secondary electrons. Backscattered electrons can be detected only if they fall on the scintillator directly or if they get absorbed by a material beyond the grid, which causes emition of secondary electrons that can fall on the scintillator. However, the image reconstructed in such a way is weak and noisy. More often so-called Robinson detector is used. It consists of an annular shaped scintillator placed directly over the sample. The photons emitted by the scintillator are directed towards the photomultiplier tube. Another alternative is a solid-state detector that consists of a silicon diode. If backscattered electrons penetrate into the region between the n-doped and p-doped parts of the diode, they can excite electrons from the valence to the conduction band and produce mobile electrons and holes. The current obtained in such a way can be measured and the backscattered electron signal can be reconstructed from it. Egerton [2005]

2.2.5 Electron backscatter diffraction

In the sample backscattered electrons can interfere and the resulting diffraction pattern can give us information on orientation of crystalites of a polycrystalline sample. For perfoming electron bascatter diffraction (EBSD) experiments, the sample is put into the SEM chamber at an angle of around 70° from the horizontal towards the diffraction camera, so that the incident electrons fall on the sample at an angle of 20 ° measured from the sample surface plane. The backscattered electrons can interfere with each other and produce a diffraction pattern if the Bragg's condition in the following form is satisfied:

$$2d \sin\theta = n\lambda, \tag{2.48}$$

where d is the interplanar distance, θ is the angle between the electrons and the planes of the crystal and λ is the wavelength of the electrons. Electrons satisfying this condition for different angles φ (see figure 2.5) produce bright spot at different places of the screen, producing effectively a line on the screen. The resulting pattern consists of many such lines arising from many different plane systems with different interplanar distances d. By analysing the pattern and comparing it to a simulated pattern for different rotations of the crystal, the orientation of the crystallite at the studied point can be deduced. By scanning the sample and perfoming the experiment at many points we can deduce the crystalite orientation at each point. Since the crystal orientation is the same inside each grain, using EBSD we can finally obtain a map of orientations of grains from which the polycrystalline sample consists. Goldstein et al. [2018]

2.3 X-ray diffraction analysis

2.3.1 Properties and sources of X-rays

For diffraction structure analysis we need to use electromagnetic radiation of wavelength around 10^{-10} m, which is a typical size of interatomic spacing in crystalline solids.
An X-ray tube consists of a heated filaments which emits electrons that are accelerated and then fall on the anode. When the electrons interact with the material

Figure 2.5: Electron backscatter diffraction geometry. Taken from `https://www.jeol.co.jp/en/words/semterms/search_result.html?keyword=EBSD`.

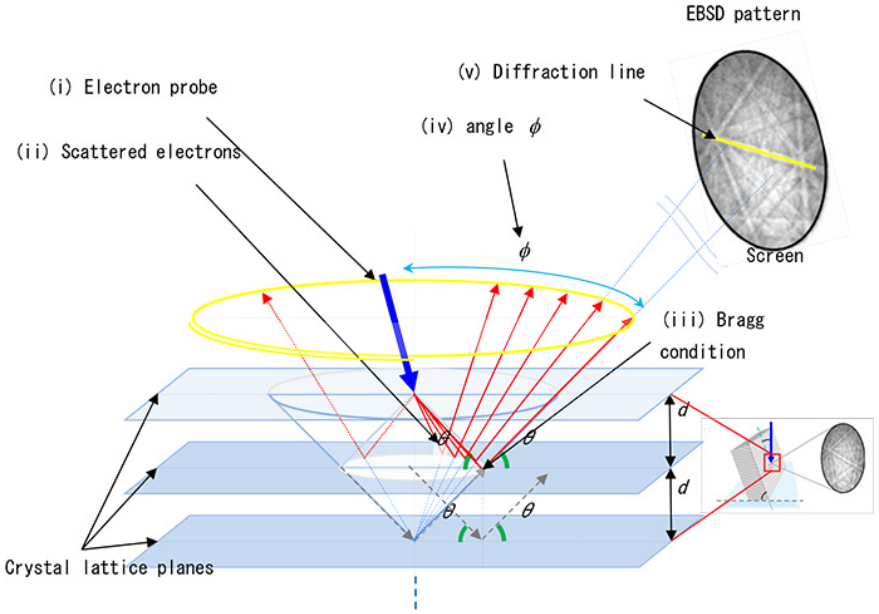

of the anode, two types of radiation is emitted: brehmstrahlung with continuous spectrum that results from the electrons slowing down in the material, and radiation with line spectrum that is a result of atomic electrons filling vacancies caused by the accelerated electrons. There are usually two lines present in the spectrum: The K_α line results from electronic transitions between the L and K shells and the K_β line results from transitions between the M and K shells. Myers [1997]

2.3.2 Elastic scattering of X-rays on a crystal

When an atom is irradiated by collimated beam of monochromatic X-rays with wave vector $\overrightarrow{k} = \frac{2\pi}{\lambda}$, it starts to radiate spherical waves of the same wavelength λ as the incoming radiation. The amplitude of the wave is dependent on the ability of the atom to scatter radiation expressed by the so-called *atomic form factor* f. For small diffration angles the atomic form factor is linearly dependent on the atomic number. For higher angles it can be approximated by a sum of Gaussians.

In a crystal each atom starts to radiate a spherical wave. The waves interfere. We can assume that in the direction of constructive interference there is a diffracted beam of wave vector $\overrightarrow{k'}$. If we assume that the scattering is elastic, than $|\overrightarrow{k}| = |\overrightarrow{k'}|$.

The wave emitted by the first atom of the crystal is given by

$$\varphi_1 = \frac{\Phi f}{r'} \mathrm{e}^{i(k'r' - \omega t)}, \tag{2.49}$$

where Φ is the amplitude of the incoming beam and r' is the distance of the

detector from the first atom. The wave emitted by the second atom is given by

$$\varphi_2 = \frac{\Phi f}{r_B} \mathrm{e}^{i(k'r' - \omega t + \Delta)}, \tag{2.50}$$

where r_B is the distance of the detector from the second atom and Δ is the phase shift of the wave emitted by the second atom with respect to the wave emitted by the first atom. If $\overrightarrow{\rho}$ is the position vector of the second atom, than the phase shift Δ is given by the equation $\Delta = \overrightarrow{\rho} \cdot \left(\overrightarrow{k'} - \overrightarrow{k} \right)$.

Let us denote the position vector of the j-th atom $\overrightarrow{\rho}_j$ and the distance of the j-th atom from the detector r_j. Than the signal at the detector caused by waves emitted from all the atoms in the crystal is

$$\varphi = \sum_{\text{allatoms}} \frac{\Phi f}{r_j} \mathrm{e}^{i\left(k'r' - \omega t + \overrightarrow{\rho}_j \cdot \Delta \overrightarrow{k}\right)}. \tag{2.51}$$

The diffraction pattern will be caused mainly by the $\sum_{\text{allatoms}} \mathrm{e}^{i\left(\overrightarrow{\rho}_j \cdot \Delta \overrightarrow{k}\right)}$. The position of the j-th atom $\overrightarrow{\rho}_j$ can be expressed using lattice basis vector $\overrightarrow{a}$, $\overrightarrow{b}$ and $\overrightarrow{c}$:

$$\overrightarrow{\rho}_j = m\overrightarrow{a} + n\overrightarrow{b} + p\overrightarrow{c}. \tag{2.52}$$

Then we can write

$$\sum_{\text{allatoms}} \mathrm{e}^{i\left(\overrightarrow{r}_j \cdot \Delta \overrightarrow{k}\right)} = \sum_{m,n,p=0}^{(M-1)(N-1)(P-1)} \mathrm{e}^{i\left(m\overrightarrow{a} + n\overrightarrow{b} + p\overrightarrow{c}\right) \cdot \Delta \overrightarrow{k}}. \tag{2.53}$$

This expression can be easily summed. The intensity at the detector is then proportional to the expression $I \propto |\varphi\varphi^*|$, where the asterisk denotes the complex conjugate. The intensity of the diffracted beam can be shown to be proportional to the following expression:

$$I \propto \frac{\sin\left(\frac{1}{2}M\overrightarrow{a} \cdot \Delta\overrightarrow{k}\right)}{\sin\left(\frac{1}{2}\overrightarrow{a} \cdot \Delta\overrightarrow{k}\right)} \cdot \frac{\sin\left(\frac{1}{2}N\overrightarrow{b} \cdot \Delta\overrightarrow{k}\right)}{\sin\left(\frac{1}{2}\overrightarrow{b} \cdot \Delta\overrightarrow{k}\right)} \cdot \frac{\sin\left(\frac{1}{2}P\overrightarrow{c} \cdot \Delta\overrightarrow{k}\right)}{\sin\left(\frac{1}{2}\overrightarrow{c} \cdot \Delta\overrightarrow{k}\right)}. \tag{2.54}$$

The diffraction maxima can be found in directions for which the following conditions hold:

$$\sin\left(\frac{1}{2}\overrightarrow{a} \cdot \Delta\overrightarrow{k}\right) = 0 \tag{2.55}$$

$$\sin\left(\frac{1}{2}\overrightarrow{b} \cdot \Delta\overrightarrow{k}\right) = 0 \tag{2.56}$$

$$\sin\left(\frac{1}{2}\overrightarrow{c} \cdot \Delta\overrightarrow{k}\right) = 0. \tag{2.57}$$

This condition can be funfilled if

$$\Delta\overrightarrow{k} = h\overrightarrow{A} + k\overrightarrow{B} + l\overrightarrow{C}, \tag{2.58}$$

where h, k, l are integers (so-called *Miller indices*) and $\overrightarrow{A}$, $\overrightarrow{B}$ and $\overrightarrow{C}$ are reciprocal lattice basis vectors given by the following equations:

$$\overrightarrow{A} = 2\pi \frac{\overrightarrow{b} \times \overrightarrow{c}}{\overrightarrow{a} \cdot \left(\overrightarrow{b} \times \overrightarrow{c}\right)} \tag{2.59}$$

$$\overrightarrow{B} = 2\pi \frac{\overrightarrow{c} \times \overrightarrow{a}}{\overrightarrow{a} \cdot \left(\overrightarrow{b} \times \overrightarrow{c}\right)} \tag{2.60}$$

$$\overrightarrow{C} = 2\pi \frac{\overrightarrow{a} \times \overrightarrow{b}}{\overrightarrow{a} \cdot \left(\overrightarrow{b} \times \overrightarrow{c}\right)}. \tag{2.61}$$

Myers [1997]

2.3.3 Diffraction conditions

Diffraction maxima will be found in directions for which the following condition holds:

$$\Delta \overrightarrow{k} = h\overrightarrow{A} + k\overrightarrow{B} + l\overrightarrow{C} = \overrightarrow{G}_{hkl}, \tag{2.62}$$

where $\overrightarrow{G}_{hkl}$ is the reciprocal lattice vector perpendicular to the atomic plane of Miller indices h, k, l. One of the alternative formulations of this condition is called *Bragg's law*, which can be stated as follows: Diffraction maximum will be found if the following equation holds:

$$2d_{hkl} \sin\theta = n\lambda, \tag{2.63}$$

where θ is the angle between the crystal planes (of Miller indices h, k, l) and the incoming X-ray beam, d_{hkl} is the interplanar spacing between these planes, λ is the wavelength of the X-rays and n is the diffraction order. In reality one does not need to take into account higher-order diffraction, because n-th order diffraction on (h, k, l) planes is equivalent to the first-order diffraction on (nh, nk, nl) planes as the spacing between the (nh, nk, nl) is n-times smaller than the spacing between the (h, k, l) planes. Myers [1997]

2.3.4 Structure factor

In the preceding sections we assumed that all the atoms in the crystal have the same atomic form factor. If we now assume that the j-th atom has the atomic form factor f_j, then the term that is responsible for the diffraction pattern will be

$$\sum_j f_j \mathrm{e}^{i\left(\overrightarrow{\rho}_j \cdot \Delta\overrightarrow{k}\right)}. \tag{2.64}$$

Now if we plug into this expression $\overrightarrow{\rho}_j = u_j\overrightarrow{a} + v_j\overrightarrow{b} + w_j\overrightarrow{c}$ and the diffraction condition $\Delta\overrightarrow{k} = h\overrightarrow{A} + k\overrightarrow{B} + l\overrightarrow{C}$, we receive the so-called *structure factor* F_{hkl}:

$$F_{hkl} = \sum_j f_j \mathrm{e}^{i2\pi(hu_j kv_j lw_j)}. \tag{2.65}$$

The structure factor is zero for certain combinations of Miller indices h, k, l and certain types of crystal structure. This leads to systematic absences of diffraction peaks in the difractograms. In the simple cubic system there is no systematic absence, there will be a diffraction peak for any combination of Miller indices. But for body-centered cubic system for odd sums $h + k + l$ the structure factor will be zero, and thus there will be no peak. Similarly for face-centered cubic system, there will be no peak unless the indices h, k, l are either all even or all odd. Myers [1997]

2.3.5 Diffraction experiments

There are three basic X-ray diffraction experiments that can be used:

- **Laue method** In Laue method radiation of wavelength 0.2 Å to 2 Å is used. The crystal is stationary. The crystal chooses directions and wavelengths, for which diffraction maxima conditions are fulfilled. Each point in the diffraction pattern can be associated with different wavelength and diffraction angle θ. The diffraction pattern can be used to tell the symmetry of the crystal (since it has the same symmetry as the crystal) and to position the crystal in the desirable orientation0 (since the diffraction pattern of a known crystal for any orientation can be simulated).

- **Rotating crystal method** Using the rotating crystal method monocrystalline samples are studied using monochromatic X-rays. The crystal is being rotated around an axis. When the diffraction condition is met, a bright spot on the screen is observed.

- **Debye-Scherrer (powder diffraction) method** One can study powdered polycrystalline samples using the Debye-Scherrer method. The sample is grinded into a fine powder and put in a glass capillary. Every small grain of sample is randomly oriented, so one can expect that all orientations are present. If the sample is irradiated by X-rays, there are grains that are oriented in just the right direction so that the diffraction maximum condition is fulfilled. There is a cone of beams of angle $4\theta hkl$ leaving the sample that causes a bright circle to appear on the screen for each diffraction order and each set of grains oriented the correct way. Myers [1997]

2.3.6 Powder diffraction

The powder diffraction method is often conducted in the symmetric, so-called Bragg-Brentano geometry. In this geometry both the X-ray source and the X-ray detector are at an angle of θ with respect to the sample surface. The angle between the direction from which the X-rays come and the direction of the detector is therefore 2θ. From this reason the Bragg-Brentano geometry is sometimes called the $\theta - 2\theta$ geometry. When perfoming the experiment, the X-ray source is fixed at low incidence angle of about 5°, the sample is rotating at a rate of θ per minute and the detector is rotating at a rate of 2θ per minute. The diffraction condition is met for planes that are parallel to the sample surface.

The result of the measurement is a graph of the dependence of intensity measured by the X-ray detector on the angle 2θ. This graph shows distinct peaks corresponding to the diffraction on planes with Miller indices h, k, l with interplanar distances d_{hkl}. From the position of the peak interplanar distances and subsequently lattice parameters a_{hkl} can be deduced. There is a systematic error in the measurement caused by a deviation from the excentric position of the sample with respect to the center of focusing circle. We can correct the measured lattice parameters a_{hkl} by means of extrapolation, since for cubic materials the following holds:

$$a_{hkl} = a_0 + s \cos\theta \coth\theta, \tag{2.66}$$

where a_0 is the correct lattice parameter and s is a constant characterizing systematic instrumental error.

3. Samples preparation and characterisation methods

In the present work, NbTaTiZr, HfNbTaTiZr, HfNbTiVZr and HfNbTaTiVZr alloys were studied. All of the samples were prepared by vacuum arc melting and their microstructure and mechanical properties were investigated. Apart from that, HfNbTaTiZr alloy was processed by severe plastic deformation methods in order to refine its grains. The following sections give a brief review of vacuum arc melting, grain refinement techniques. The final sections give more information on the preparation and characterisation of the samples.

3.1 Vacuum arc melting

At the start of the vacuum arc remelting process, the alloy is formed into a cylinder electrode. The electrode is put into a cylindrical crucible made of copper, which is brought to a vacuum of about 0.1 to 13.3 Pascals. Subsequently the chamber is filled with Ar inert gas with pressure in the range $(0.3 - 0.8) \cdot 10^4$ Pa. There is a small amount of alloy on the bottom of the crucible. Large DC current is run into the electrode, starting an electric arc between the electrode and the alloy on the bottom, which causes the alloy to melt. The crucible is cooled by water. The solidification rate can be controlled by adjusting the electric current, the water cooling and the electrode distance from the sample.
The advantages of vaccum arc melting over other kinds of melting processes include removal of dissolved gases (hydrogen, nitrogen, oxygen, carbon dioxide, etc.) from the alloy and reduction of concentration of trace elements with high vapour pressure, such as carbon, sulfur, and magnesium. Moreover, the solidification rate of molten alloy can be closely controlled, which is important for avoiding segregation and porosity.

3.2 Grain refinement

Mechanical properties of metals and alloys can be often improved by grain refinement, since grain boundaries represent obstacles for motion of dislocations. The hardness (and other mechanical properties, like yield stress) is in many cases given by the famous Hall-Petch equation, which shows to be applicable to many metals and alloys. It can be stated in the following form:

$$H = H_0 + \frac{k_y}{\sqrt{d}}, \tag{3.1}$$

where H is the hardness, H_0 and k_y are material dependent constants and d is the average grain diameter. Materials with lower grain diameter show more strength, higher yield stress, but are usually brittle.

When it comes to high entropy alloys, previous studies of fcc CoCrFeMnNi HEA revealed an increase of strength in accordance with the Hall-Petch equation. Liu et al. [2013b] Increase of strength and ductility with decreasing grain size has been observed also for bcc HfNbTaTiZr HEA.
Modern methods using severe plastic deformation has been developed in order to refine the grains in small samples to the order of hundreds of nanometers. Ultrafine grained metals usually show higher strength and isotropic properties. Experimental proof of the Hall-Petch equation of ultrafine grained materials is not easy due to the small size of samples that can be subjected to severe plastic deformation. Nonetheless, the research performed on titan, copper and zinc indicate that the Hall-Petch equation may hold also for ultrafine grained materials.
Studies of ultrafine grained HEAs are not very common. CoCrFeMnNi HEA has been successfully processed and its strength increased approximately three times after its grains were refined to size sufficiently below 100 nm. Lee et al. [2016]

3.3 High pressure torsion

In the past decades, various methods for grain refinement down to nanoscale using severe plastic deformation have been developed. The most efficient method is high pressure torsion (HPT). It is a method that is characterized by deformation of disk-shaped samples by both compression and torsion. The sample is clamped between two anvils, the compression pressure is of the order of gigapascals. Torsion deformation is induced by rotation of the bottom anvil. The equivalent strain e at the distance r from the centre of the sample can be estimated from the following equation:

$$e = \frac{\phi r}{h\sqrt{3}}, \tag{3.2}$$

where $\phi = 2\pi N$, N is the number of revolution of the bottom anvil and h is the thicknesses of the sample after the deformation.
As can be seen from the equation, the deformation near the centre of the disc is small. Near the centre of the disc the grain size stays considerably bigger than near the edges, and the hardness in the centre is therefore far smaller. To achieve more homogenized results it is often necessary to deform the sample with pressure of several GPa and choose at least $N \approx 5$ revolutions. Zhilyaev and Langdon [2008]

3.4 NbTaTiZr, HfNbTaTiZr, HfNbTiVZr and HfNbTaTiVZr samples

NbTaTiZr, HfNbTaTiZr, HfNbTiVZr and HfNbTaTiVZr samples were prepared by vacuum arc melting from metals of 99.99% purity. Casting was done in an arc melting system AM200 (Edmund Bühler) equipped with a high vacuum pumping system with base pressure 10^{-7} mbar. Melting was done in an argon protective atmosphere of 400mbar pressure. Each sample was 10 times remelted and flipped, so that good homogeneity was ensured. Ingots had dimensions of approximately $100 \times 10 \times 5\,\mathrm{mm}^3$. Samples were annealed at 1200 °C for two hours in a vacuum

furnace in a vacuum of 10^{-5} mbar. When the annealing was finished the samples were quenched in water in vacuum.
The microstructure of these samples was investigated using scanning electron microscope FEI Quanta 200F) equipped with energy dispersive spectrometer (EDS). X-ray diffraction (XRD) measurements were done using the diffractometer D8 Discover (Bruker) and CuKα radiation.
Tensile properties were investigated at room temperature using Instron 1186 machine equipped with digital optical correlation system. The strain rate was 10^{-3} s^{-1}. Standard dog bone shape samples of length of 10.5 mm and diameter of 2 mm were cut from the ingots for this purpose. Vickers microhardness testing was carried out on an automated hardness tester Durascan by Struers. The applyied load was 0.5 kg for 10 s.

3.5 Grain refined HfNbTaTiZr samples

High pressure torsion (HPT) was employed for grain refinement of HfNbTaTiZr alloy prepared by arc melting. In order to process the alloy using HPT, small discs of diameter of 20 mm and thickness of 1 mm were cut from the cast ingot. These discs were than processed at room temperature with pressure of 2.5 GPa and with $N = \frac{1}{4}, \frac{1}{2}, 1, 5$ and 15 revolutions. Sample only compressed by the pressure of 2.5 GPa without any torsion deformation was also prepared.
As samples processed by HPT can be very inhomogeneous, the homogeneity of the samples was examined using Vickers hardness measurement. The measurements were carried out using automatic Struers Durascan 50. Load of 100 g applied for 10 s was used for each measurement in nodes of a rectangular mesh with node spacing of 0.5 mm.
Tensile testing was performed on the samples at room temperature with constant strain rate of 10^{-4} s^{-1}. The testing was performed two times on each of two miniature samples cut from the HPT processed discs. The miniature samples had length of 4.7 mm, width of 1.6 mm and thickness of 0.8 mm. One of the samples was cut near the centre of the disk, the other near the edge. The positions of the places from which the samples were cut is depicted in figure 3.1. Random speckle pattern was sprayed on the surface of the miniature samples, which allowed to measure strain using an optical extensometer with digital image correlation. As a reference, standard tensile measurement was also performed on dog-boneshape specimen of length of 12 mm, width of 3 mm and thickness of 2 mm cut from the as-cast alloy. Fracture surfaces of the samples ruptured in the tests were examined using JEOL JSM 5510LV scanning electron microscope.
Scanning electron miscroscopy observations of microstructure and EBSD measurements were done using ZEISS AURIGA COMPACT with EBSD camera. The area of the samples from which the EBSD map was made had dimensions of 1500 to 2500 mm^2 and the step size was 3 mm.
Transmission electron microscopy measurements were done using JEOL JEM 2000FX microscope operating at 200 kV. The locations on the sample from which circular samples for thin foils' preparation were taken are depicted in figure 3.1. The foils were prepared by twin-jet electro polishing using a H_2SO_4 and HF mixture (with volume ratio 9:1) at the temperature of 35 °C.

Figure 3.1: Geometry of a HfNbTaTiZr alloy sample processed by HPT: a) sample disc, b) figure depicting locations where measurements were taken. Positron annihilation measurements were taken at grey spots, tensile experiments were performed on cuts showed by blue solid line.

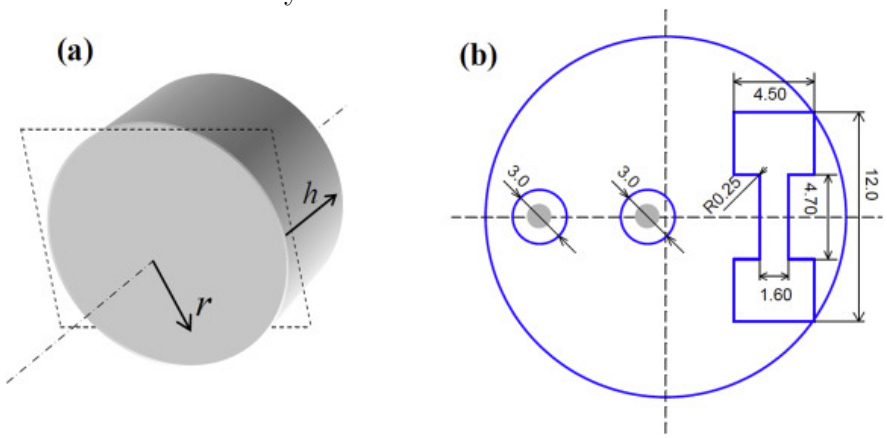

X-ray diffraction (XRD) characterizations were carried out on BRUKER D8 DISCOVER diffractometer equipped with 1D LYNX EYE detector. Diffraction patterns were measured in symmetrical Bragg- Brentano geometry using CuKα radiation. Preferred grain orientation was characterized by the Harris texture indices. Finally, the samples were examined using positron annihilation techniques. The measurements were done in two places on the sample, in the distance of approximately 1 and 7 mm from the centre of the disc. For positron lifetime measurements spectrometer with the time resolution of 145 ps was used. Standard ^{22}Na positron source with activity around 1.5 MBq was used. The source contribution to positron lifetime spectra consists of two components with lifetimes of 368 ps and 1.5 ns and intensities of 10% and 1%. These two components correspond to the positron annihilation events inside the source of positrons and the mylar foil in which the source was wrapped.

4. Microstructure and mechanical properties

4.1 NbTaTiZr alloy

Images from scanning electron miscroscope of NbTaTiZr alloy samples are in figure 4.1. It can be seen from the images that microstructure near the edges of the ingots is homogeneous. On the other hand, microstructure deeper in the ingot and at the centre of the ingot shows distinct phase separation in the form of dendritic structures. Both of these areas were analysed using EDS. EDS measurements are in figure 4.2. They proved that areas near edges have indeed homogeneous composition and that the bright areas in figure 4.2 are enriched in Nb and Ta, whereas the dark areas are Zr and Hf. This shows that solid solution phase is metastable at room temperature and was retained only near the edges of the samples that were cooled with the highest cooling rate.

Figure 4.1: SEM image of NbTaTiZr alloy in the as-cast case for a) area near the edge of the ingot, b) the centre of the ingot.

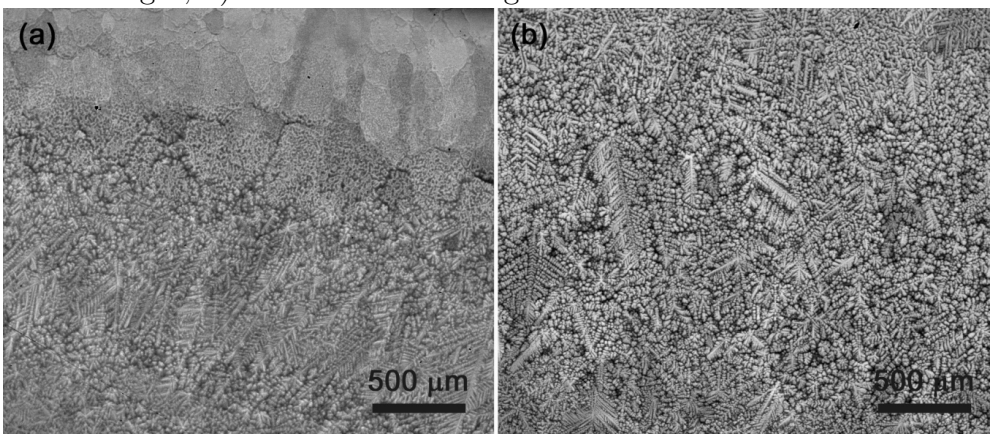

Figure 4.2: Line EDS scan of the NbTaTiZr alloy sample in the as-cast state along the horizontal line for a) area near the edge of the ingot, b) the centre of the ingot.

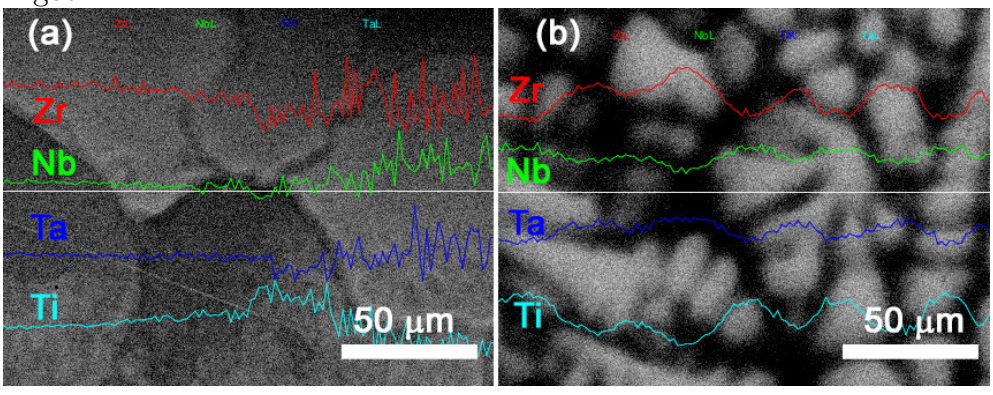

The composition of the bright areas enriched in Nb and Ta is

(32 ± 2) at.%Nb, (35 ± 2) at.%Ta, (17 ± 1) at.%Ti, (16 ± 1) at.%Zr.
The composition of the dark areas enriched in Zr and Hf is
(23 ± 2) at.%Nb, (17 ± 2) at.%Ta, (25 ± 2) at.%Ti, (35 ± 2) at.%Zr.
Both of these phases have bcc structure, as was confirmed by X-ray diffraction analysis. The X-ray diffraction spectrum is plotted in figure 4.3. It shows diffraction peaks corresponding to BCC structure. The peaks are significantly broaneded, because they consist of two overlapping peaks corresponding to each of the two phases. Analysis of the spectrum showed that the Nb, Ta rich phase has the lattice parameter of $a = 3.3509(8)$ Å, while Ti, Zr phase has the lattice parameter of $a = 3.380(2)$ Å.

Figure 4.3: X-ray diffraction spectrum for NbTaTiZr alloy in the as-cast state and in the state upon annealing at 1200 °C.

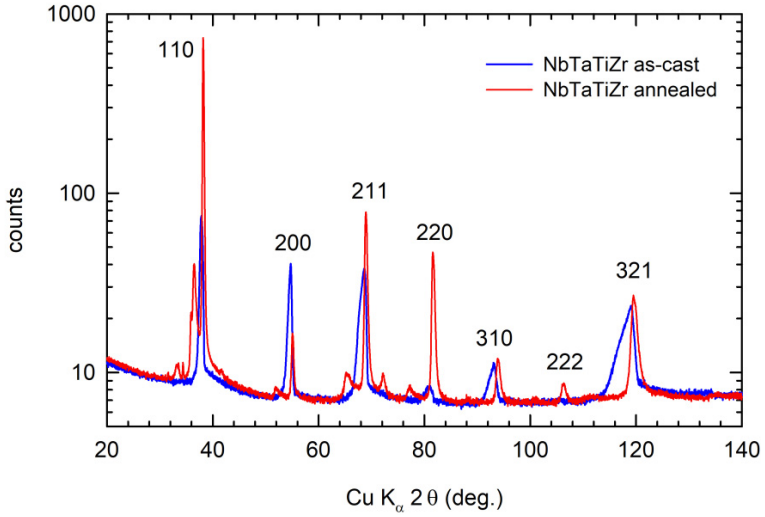

The image from scanning electron microscope of the sample annealed at 1200 °C is in figure 4.4. The dendritic microstructure is similar to the miscrostructure of as-cast samples. The EDS elemental maps in figure 4.5 show that there are still areas enriched in Nb and Ta separated by dendritic arms enriched in Ti and Zr. Therefore annealing at 1200 °C is not sufficient to form single phase solid solution. The X-ray diffraction spectrum in figure 4.3 shows less sharp peaks, which is indicative of sharpening of both phases. It means that the change of chemical composition is more abrupt around the dendritic arms.

Figure 4.4: SEM images of NbTaTiZr alloy upon annealing at 1200 °C. Image a) shows an overview of the microstructure, image b) shows a detail.

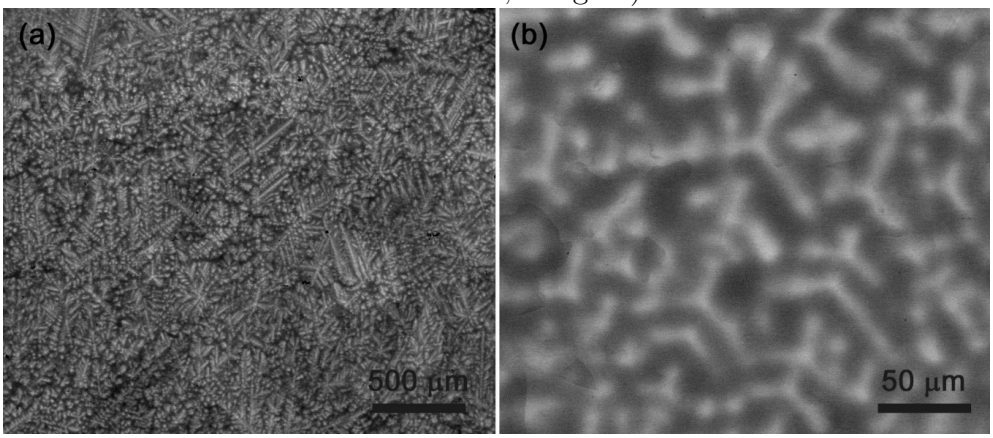

Figure 4.5: EDS elemental maps of NbTaTiZr alloy upon annealing at 1200 °C.

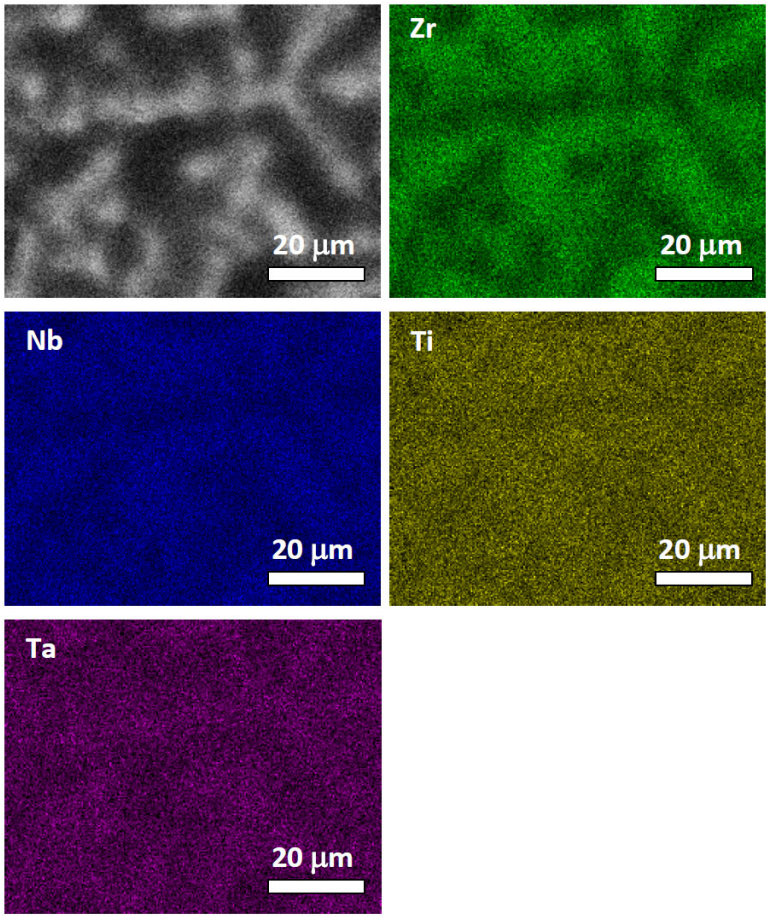

4.2 HfNbTaTiZr alloy

SEM micrographs of HfNbTaTiZr alloy miscrostructure is shown in figure 4.6. The structure is again inhomogenenous with dendritic arms, but this time the changes in composition between the two phases are smaller. This indicates that

the addition of Hf has a role in stabilizing solid solution. The EDS scans are in figure 4.7. The composition of the phases is as follows.

Figure 4.6: SEM image of HfNbTaTiZr alloy in the as-cast case. Image a) shows an overview of microstructure, image b) shows a detail.

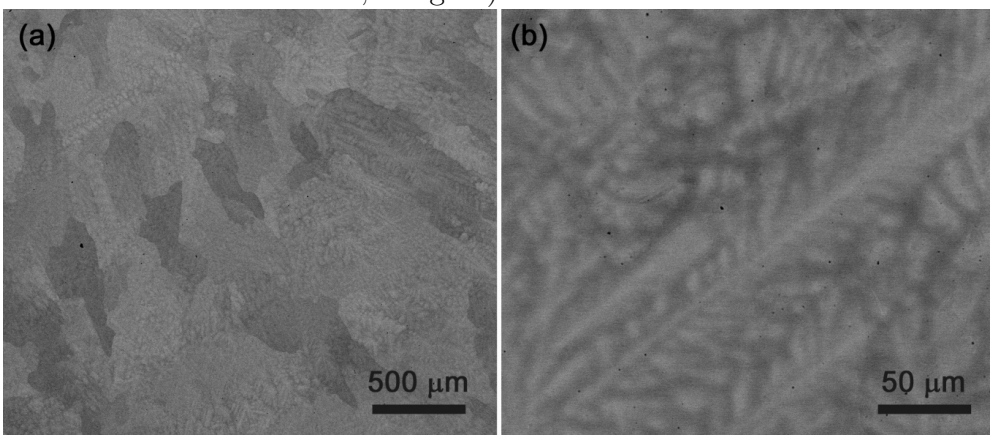

Figure 4.7: EDS elemental maps of HfNbTaTiZr alloy in the as-cast state.

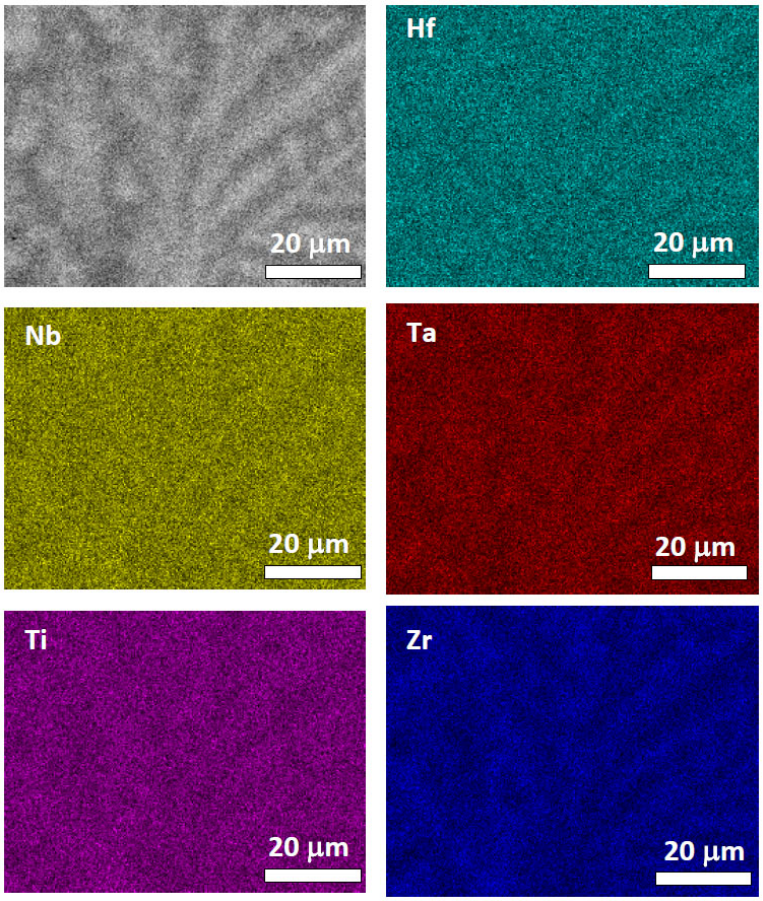

The composition of the bright areas enriched in Nb and Ta is (20 ± 1) at.%Hf, (23 ± 1) at.%Nb, (21 ± 1) at.%Ta, (17 ± 1) at.%Ti, (19 ± 1) at.%Zr. The composition of the dark areas enriched in Zr and Hf is (21 ± 1) at.%Hf, (19 ± 1) at.%Nb, (18 ± 1) at.%Ta, (21 ± 1) at.%Ti, (21 ± 1) at.%Zr.

The X-ray diffraction spectrum is in figure 4.8. Again the peaks are diffraction peaks of BCC structure and they are slightly broaneded, because they contain two overlapping peaks correspoding to both phases. Because the broadening is only small, it can be assumed that the sample consists of only one phase of lattice parameter $a = 3.4059(1)$ Å.

Figure 4.8: X-ray diffraction spectrum for HfNbTaTiZr alloy in the as-cast state and in the state upon annealing at 1200 °C.

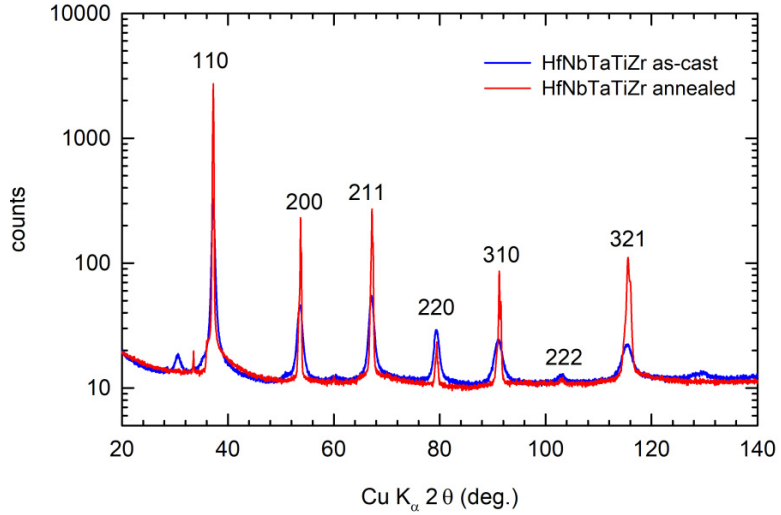

Upon annealing at 1200 °C, the sample exhibits only one solid solution phase, as can be seen from SEM image in figure 4.9. EDS scan (figure 4.10) showed nearly uniform distribution of alloying elements in the sample. Annealing resulted in narrower X-ray diffraction peaks that correspond to BCC structure with lattice parameter of $a = 3.4055(1)$ Å.

Figure 4.9: SEM image of HfNbTaTiZr alloy after annealing at 1200 °C. Image a) shows an overview of the microstructure, image b) shows a detail.

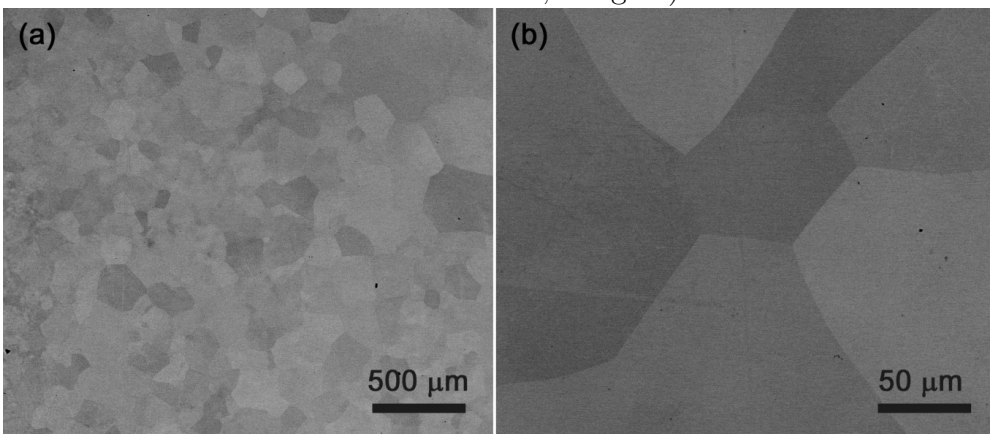

Figure 4.10: EDS elemental maps of HfNbTaTiZr alloy after annealing at 1200°C.

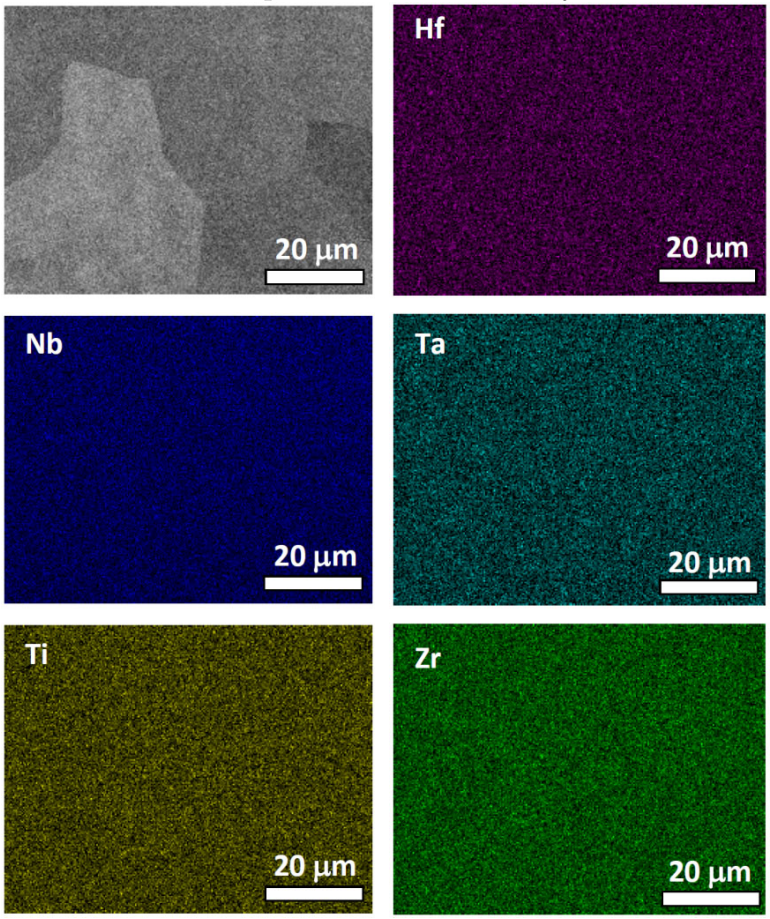

As will be further discussed in the upcoming sections, solid solution phase in HfNbTaTiZr alloy is metastable at room temperature. Below 1000 °C the solid solution phase decomposes into two BCC phases and below 800 °C the phase rich in Hf, Ti, Zr further develops into a HCP phase. The single solid solution BCC phase can be retained when rapidly quenched upon annealing.
In the as-cast sample two BCC structures were observed, which means that the cooling rate was not fast enough to prevent formation of the two BCC phases, but was still fast enough to prevent transformation of the Hf, Ti, Zr rich phase into HCP structure. The absence of transoformation is caused by low mobilitiy of alloying atoms at low temperatures. The transformation requires annealing for extensive period of time at the temperature of around 600 °C. This was investigated using sample that was annealed in vacuum at 1000 °C and then let slowly cool with the furnace. As can be seen from SEM images of such samples in figure 4.11, Hf, Ti, Zr rich HCP phase was formed at grain boundaries in this case.

Figure 4.11: SEM image of HfNbTaTiZr alloy after being annealed at 1000 °C for one hour and let slowly cool with the furnace. Image a) shows an overview of the microstructure, image b) shows a detail.

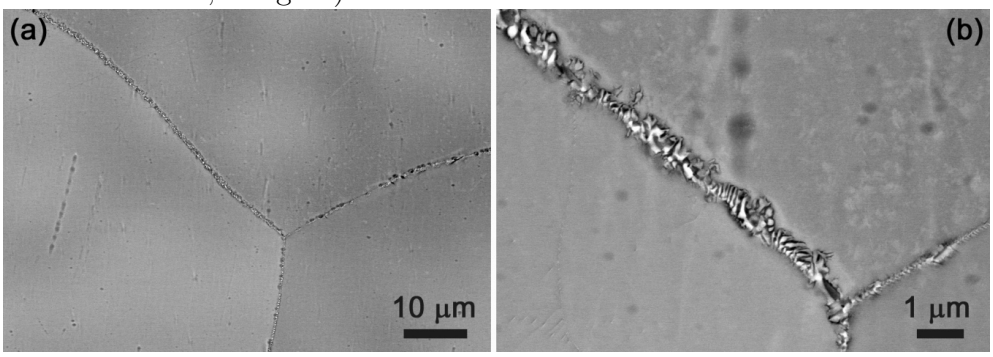

4.3 HfNbTiVZr alloy

In the HfNbTiVZr alloy, Ta is replaced by V. Since V has smaller atomic radius than other alloying elements, the lattice of HfNbTiVZr is significantly distorted. The SEM micrograph of HfNbTiVZr alloy microstructure is in figure 4.12.

Figure 4.12: SEM image of HfNbTiVZr alloy in the as-cast case. Image a) shows an overview of microstructure, image b) shows a detail.

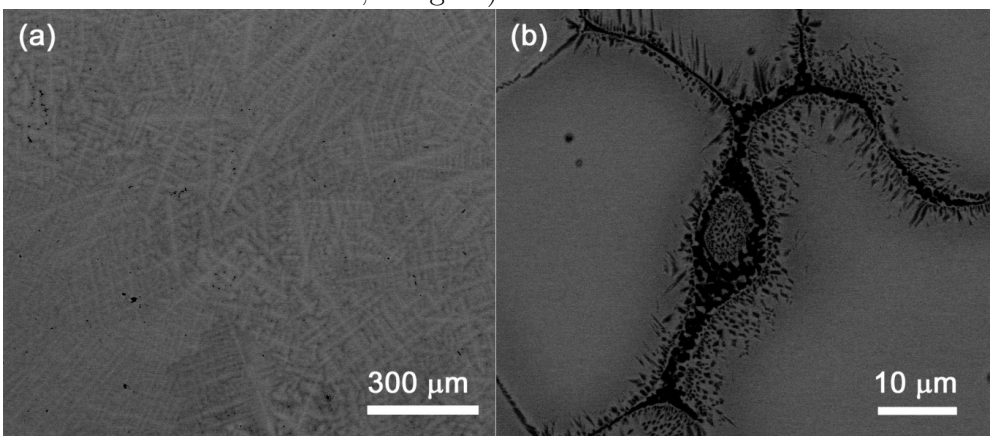

The bright areas rich in Hf and Nb have composition of
(23 ± 1) at.%Hf, (24 ± 1) at.%Nb, (20 ± 1) at.%Ti, (16 ± 1) at.%V, (17 ± 1) at.%Zr.
The composition of the dark areas rich in V and Zr is
(19 ± 1) at.%Hf, (18 ± 1) at.%Nb, (20 ± 1) at.%Ti, (22 ± 1) at.%V, (21 ± 1) at.%Zr.
Vanadium segregates at grain boundaries and form needle-like particles, as can be in in figure b). EDS measurements (see figure 4.13) confirm that these particles are enriched in V and Zr. The X-ray diffraction spectrum plotted in figure 4.14 once again correspond to BCC structure and once again the peaks are broadened, which is caused by overlapping spectra of both phases. The average lattice parameter of both phases is $a = 3.3630(6)$ Å.

Figure 4.13: EDS elemental maps of HfNbTiVZr alloy in the as-cast state.

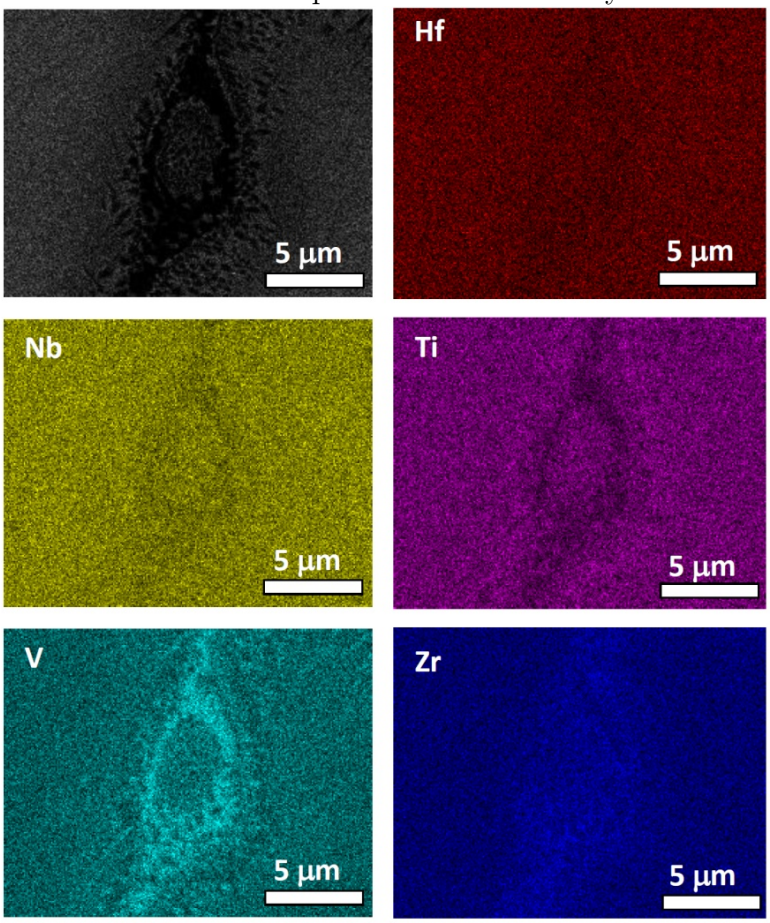

Figure 4.14: X-ray diffraction spectrum for HfNbTiVZr alloy in the as-cast state and in the state upon annealing at 1200 °C.

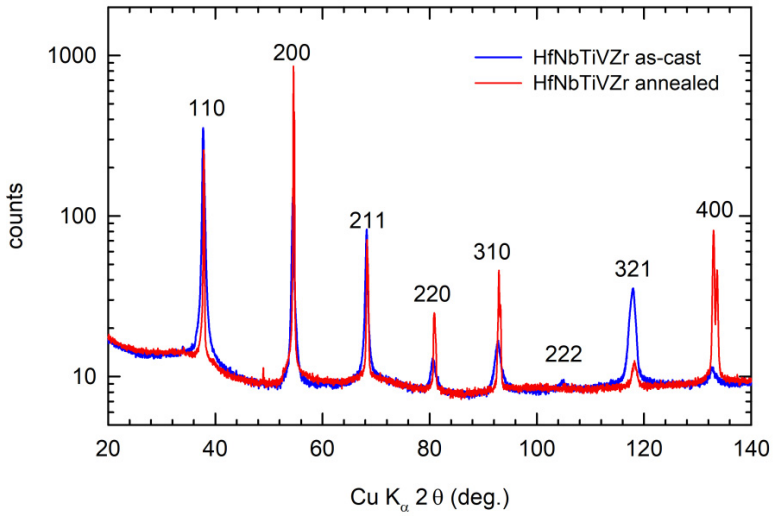

When the samples of HfNbTiVZr alloy were annealed at 1200 °C and quenched in water, a single phase solid solution was formed, which can be seen from SEM micrograph in figure 4.15. The detail in the figure shows that the segregation of V at the ground boundaries happen to a lesser extent than in the as-cast

sample. Nucleation of the phase enriched in V and Zr takes places preferentially at grain boundaries. Faster cooling rate can lead to supression of its formation. The X-ray diffraction spectrum in figure shows less broadened peaks, which is consistent with the observation of supression of the V and Zr rich phase. The lattice parameter of the annealed alloy is $a = 3.3624(4)$ Å.

Figure 4.15: SEM image of HfNbTiVZr alloy after annealing at 1200 °C. Image a) shows an overview of the microstructure, image b) shows a detail.

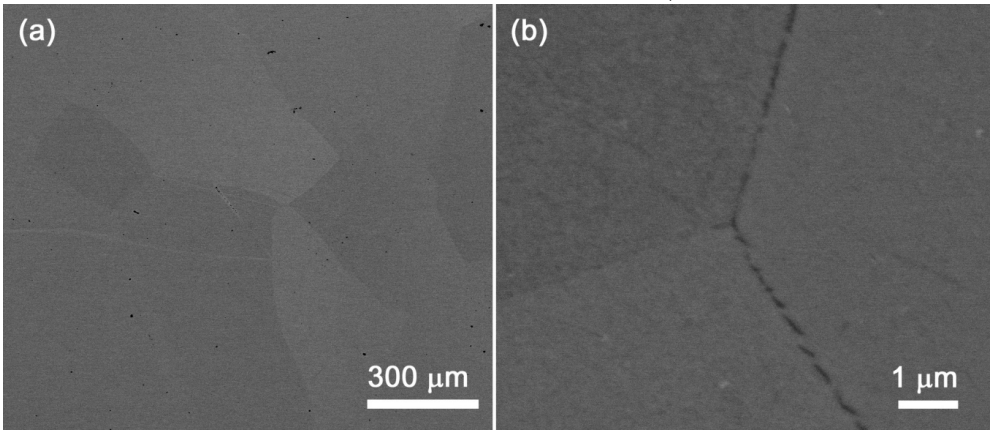

4.4 HfNbTaTiVZr alloy

The microstructure of as-cast HfNbTaTiVZr alloy is shown in figure 4.16. The EDS map for this alloy is shown in figure 4.17. The microstructure of the alloy has dendritic character with bright dendrites rich in Nb, Ta separated by darker inter-dendritic areas rich in Hf, Ti, V, Zr. Apart from that, segregation of V was observed at ground boundaries.

Figure 4.16: SEM image of HfNbTaTiVZr alloy in the as-cast case. Image a) shows an overview of microstructure, image b) shows a detail.

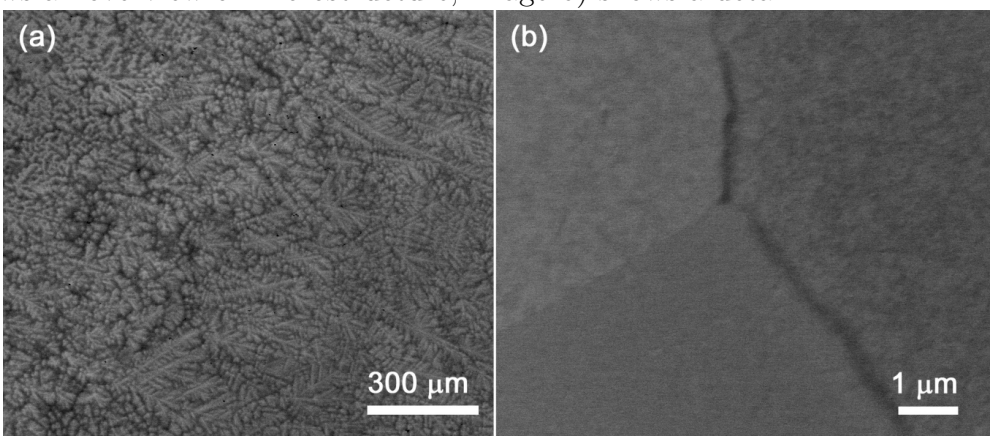

Figure 4.17: EDS elemental maps of HfNbTaTiVZr alloy in the as-cast state.

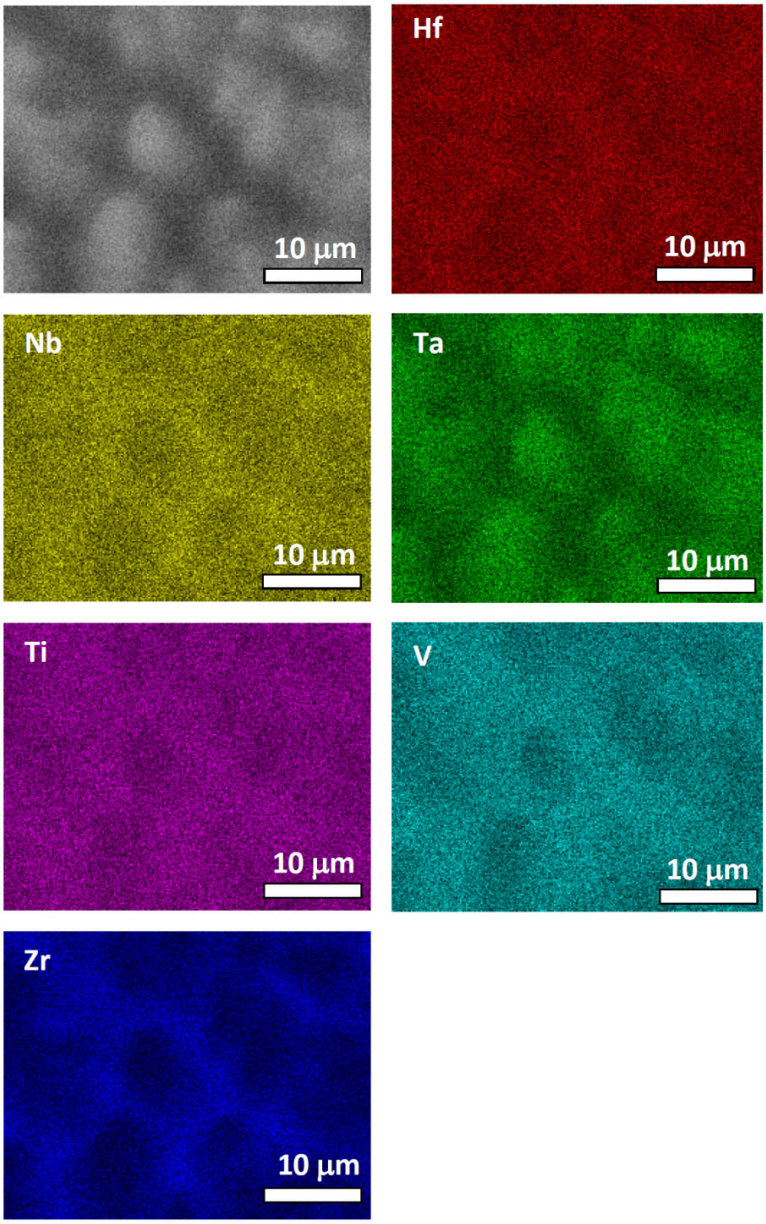

The bright areas rich in Nb and Ta are composed of
(16 ± 1) at.%Hf, (18 ± 1) at.%Nb, (20 ± 1) at.%Ta, (16 ± 1) at.%Ti, (14 ± 1) at.%V, (16 ± 1) at.%Zr.
The composition of the dark areas rich in Hf, Ti, V, Zr is
(18 ± 1) at.%Hf, (15 ± 1) at.%Nb, (12 ± 1) at.%Ta, (17 ± 1) at.%Ti, (18 ± 1) at.%V, (20 ± 1) at.%Zr.
The X-ray diffraction spectrum of the HfNbTaTiVZr alloy is plotted in figure 4.18. Its peaks correspod to the BCC structure. The peaks are broadened and consist of two overlapping spectra for each phase. The average lattice parameter is $a = 3.3545(6)$ Å.

Figure 4.18: X-ray diffraction spectrum for HfNbTaTiVZr alloy in the as-cast state and in the state upon annealing at 1200 °C.

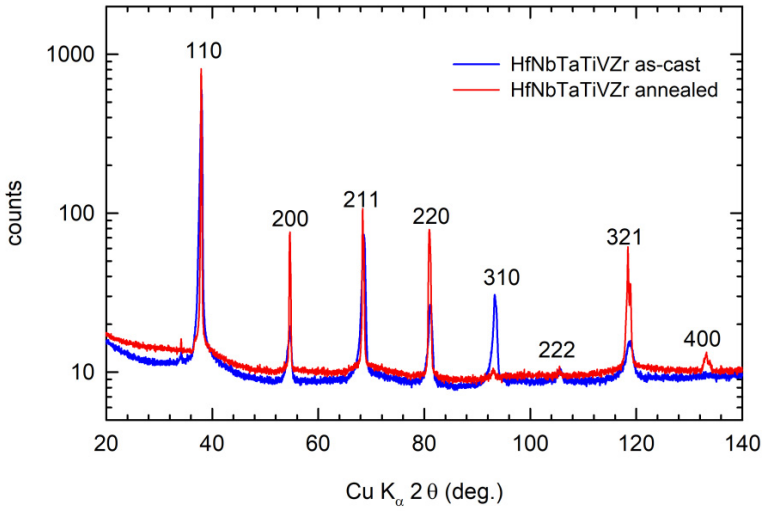

When annealed at 1200 °C, the HfNbTaTiVZr alloy exhibits single solid solution phase, which can be seen in SEM micrographs in figure 4.19, EDS maps in figure 4.20 and is also reflected in the narrower peaks in the X-ray diffraction spectrum. The lattice parameter of the annealed sample is $a = 3.3551(2)$ Å. The cooling rate was high enough to supress segregation of V at ground boundaries completely. Vlasák et al. [2022]

Figure 4.19: SEM image of HfNbTaTiVZr alloy after annealing at 1200°C. Image a) shows an overview of the microstructure, image b) shows a detail.

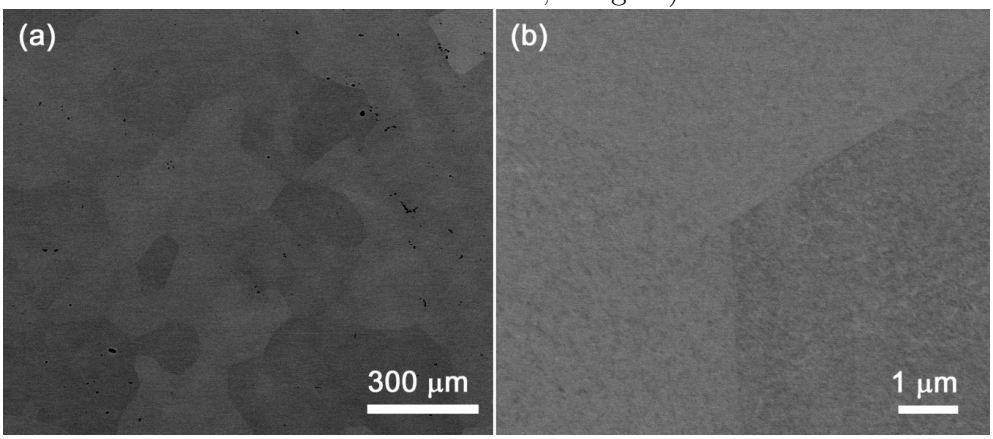

Figure 4.20: EDS elemental maps of HfNbTaTiVZr alloy after annealing at 1200 °C.

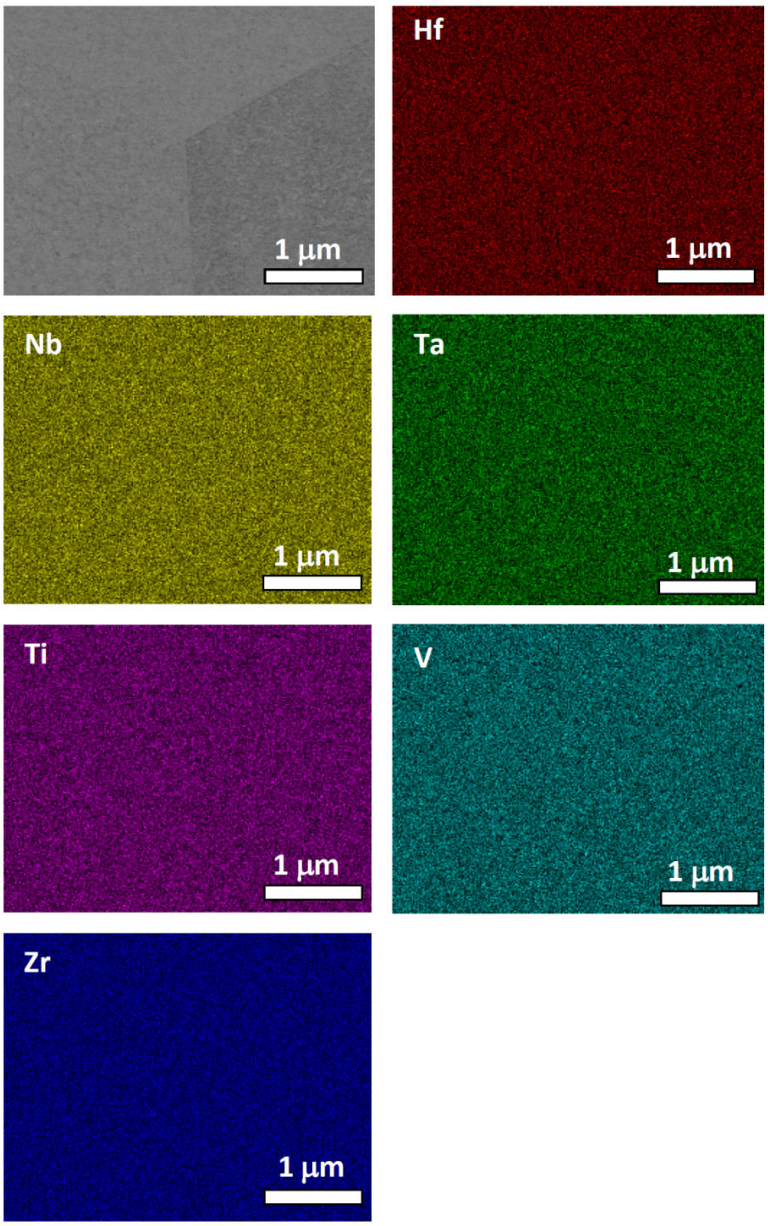

5. Grain refined HfNbTaTiZr alloy

5.1 Microstructure

First the microstructure of HfNbTaTiZr alloy was studied in the as-cast state. The XRD pattern revealed that the alloy has BCC structure with lattice parameter $a = 3.4059(1)$ Å, which is consistent with the findings on this alloy in the literature. Senkov et al. [2011a] give the lattice parameter as $a = 340.4$ pm.
EBSD map of the as-cast HfNbTaTiZr alloy is shown in figure 5.1 a). The alloy contains coarse grains with the mean size of 200 μm. The distribution of grain sizes can be seen in figure 5.2 a). Grain misorientation distribution corresponds to random distribution. According to TEM measurements, as-cast samples contain only a very small concentration of dislocations.

Figure 5.1: EBSD map of the HfNbTaTiZr alloy in a) as-cast state, b) after processing using HPT without any torsion ($N = 0$).

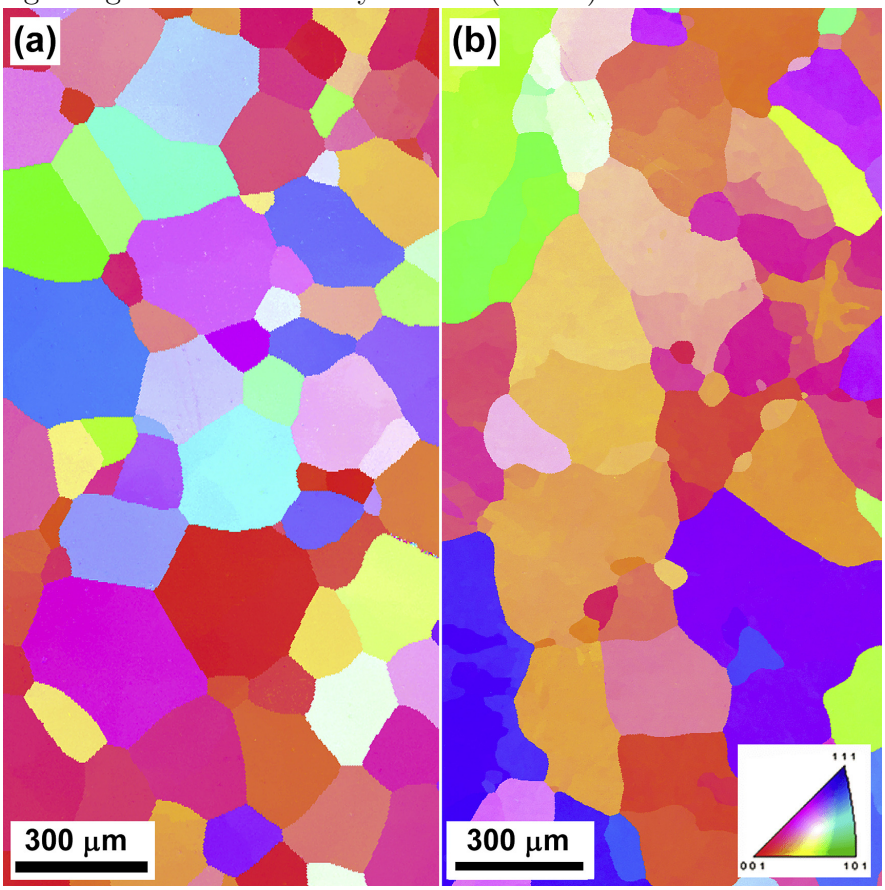

Figure 5.2: Grain size distribution histograms in a) as-cast sample, b) HPT processed sample with no torsion ($N = 0$).

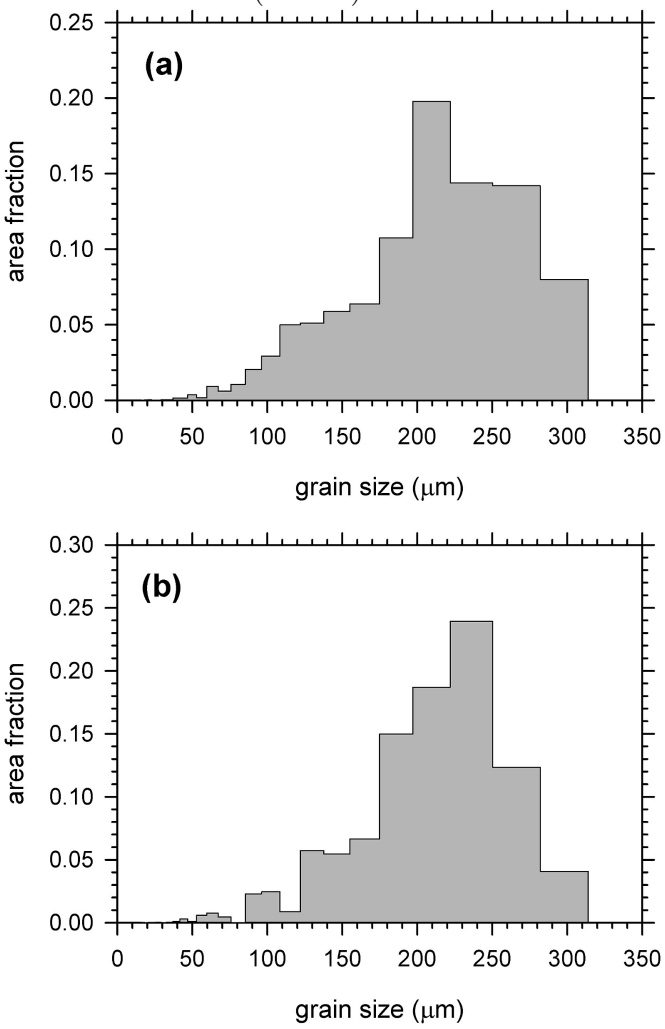

When the sample was processed using high pressure torsion without any torsion ($N = 0$), no grain refinement was detected, as can be seen from the EBSD map in figure 5.1 b). However, dislocations were introduced to the alloy by plastic deformation, which caused stress to build up inside grains. This stress causes continuous change of crystal orientation inside grains, which is reflected in the EBSD map by colour changes inside each grain.

The HPT processed sample with no torsion ($N = 0$) contains crystallites with preferred orientations $\langle 110 \rangle$ and $\langle 100 \rangle$. When HPT processed with torsion ($N > 0$), the $\{100\}$ texture component disappered, the $\{110\}$ component was retained and a new $\{211\}$ component apperared. The tendency to form such textures can be understood by noting that both $\{110\}$ and $\{211\}$ are common slip planes in BCC structures.

HPT processing with equivalent strain $e > 2$ leads to significant grain refinement, which can be seen from EBSD maps of HPT processed sample in figure 5.3. As can be seen from the map, grain fragmentation does not occur only by dislocation mechanism, but also by twinning. By analysis of the map it was found that $\{332\}\langle 113 \rangle$ twins are forming in HPT processing with smaller equivalent strains.

Figure 5.3: EBSD map of HPT processed samples with equivalent strain a) $e = 1$, b) $e = 2$, c) $e = 5$.

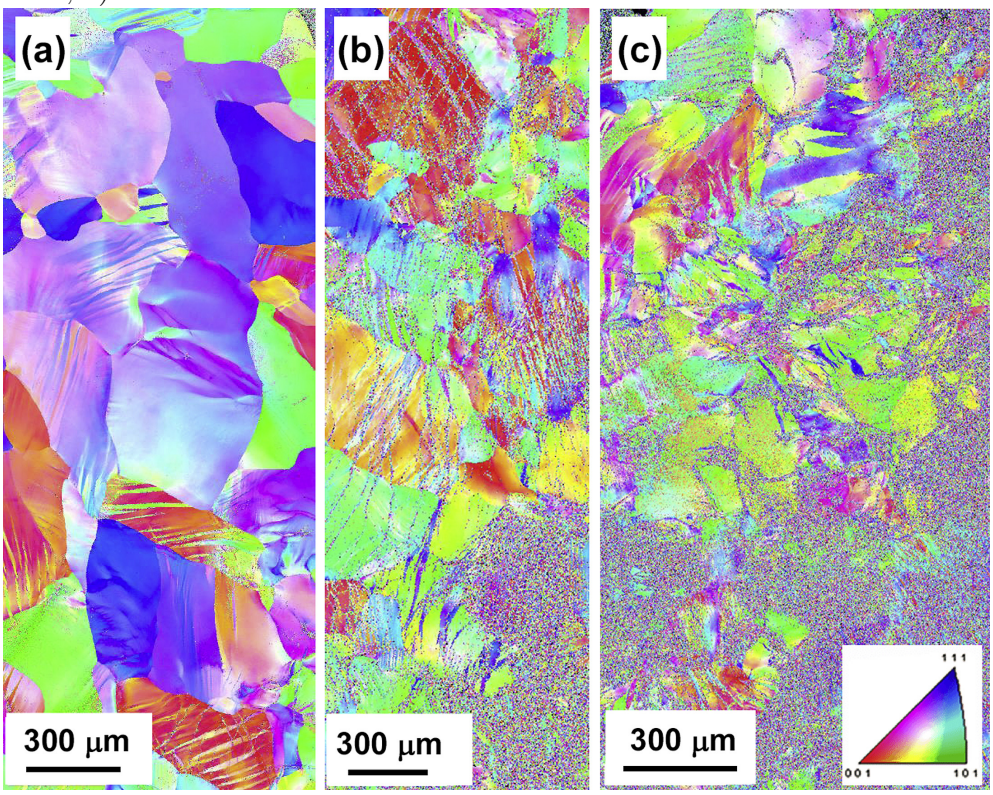

The $\{332\}\langle 113\rangle$ twins have a misorientation angle of 50.5° around the $\langle 110\rangle$ direction of the parent grain. The fraction of misorientation angles in the HPT processed samples at 50.5° is therefore enhanced, as can be seen in grain misorientation distribution histogram in figure 5.4 c). The enhancement at angles of $20 - 40°$ is caused by rotation of the $\{332\}\langle 113\rangle$ twins caused by plastic deformation.

Figure 5.4: Grain misorientation distribution histogram for a) as-cast sample, b) HPT processed sample with no torsion ($N = 0$), c) HPT processed sample with equivalent strain $e = 1$. Misorientation angles lower than 5° are not shown.

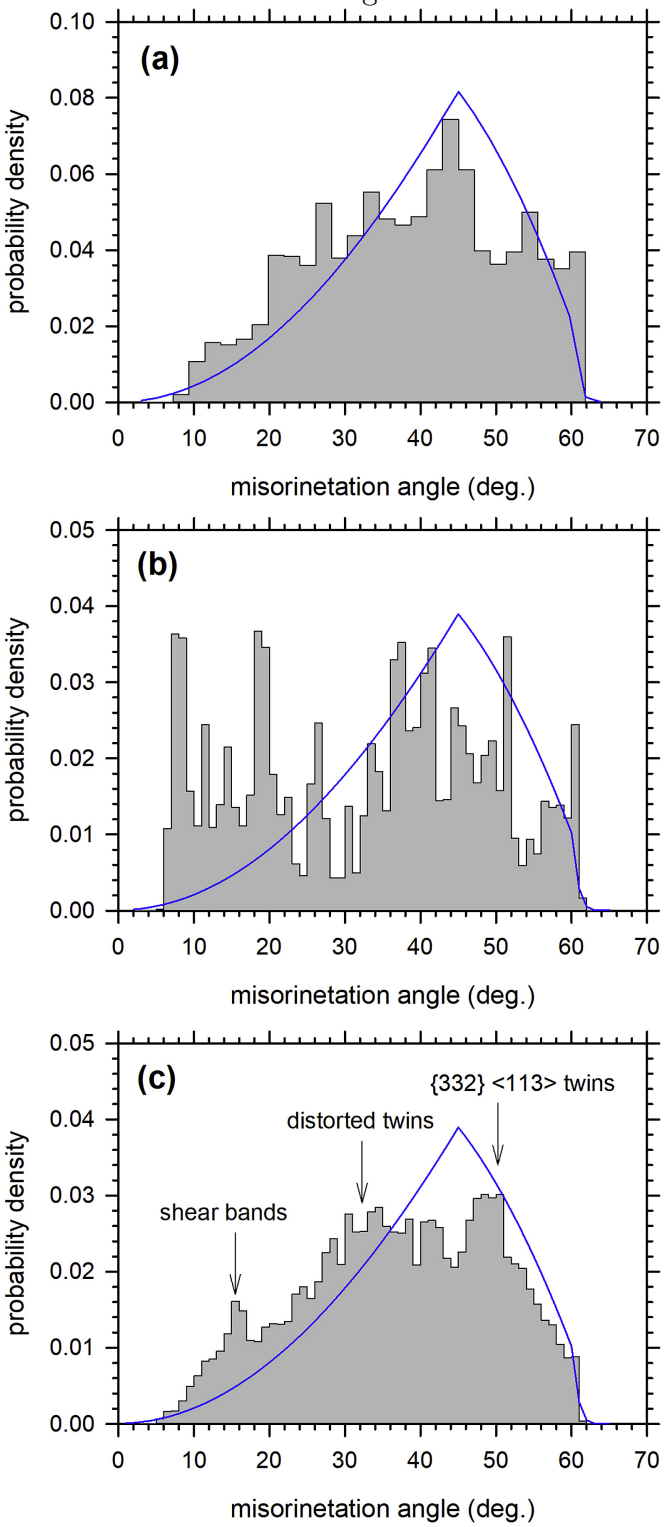

As can be seen from the EBSD maps, grain refinement occurs preferentially in grains of specific orientations when HPT processed with smaller equivalent strains. The orientations seem to be orientations unfavourbale for shear in $\{110\}\langle\bar{1}11\rangle$ and $\{211\}\langle\bar{1}11\rangle$ slip systems. For sufficiently large equivalent strains

($e > 10$) ultrafine grain structure was achieved in the whole volume of the sample, but it was impossible to perform EBSD map measurements on HPT processed samples with equivalent strain largen than 5 because of high concentration of defects and stress in grains.

5.2 Positron lifetime measurements

In the measured positron annihilation lifetime spectra two components were resolved: one component with lifetime τ_1 and intensity I_1 corresponding to annihilation of positrons in the free state (not trapped in defects) and the other with lifetime τ_2 and intensity I_2 corresponding to annihilation of positrons in defects. The lifetime of the second component is larger and is approximately equal to $\tau_2 \approx 189$ ps for both as-cast sample and samples subjected to HPT deformation with different equivalent strains. On the ohter hand, the free positron component lifetime decreases with encresing strain, for equivalent strains $e > 5$ it cannot be distinguished in the spectrum anymore. This indicates that the character of the defects does not change during HPT processing with different equivalent strains. However, the concentration of the defects increases with increasing strain, as can be deduced from the increase of the intensity of the second component. For HPT processed samples with equivalent strain $e > 5$ virtually all positrons are trapped in defects and annihilate from the trapped state.

Figure 5.5: Results of the measurements of positron lifetime on samples HPT process with different equivalent strains: lifetimes τ_1 of free positrons and τ_2 of positrons trapped in defects as a function of equivalent strain and the quantity τ_f.

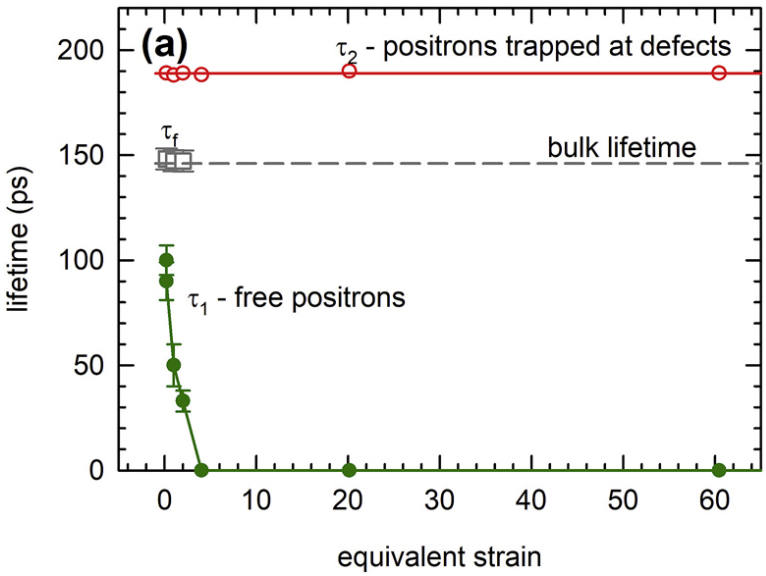

Figure 5.6: Results of the measurements of positron lifetime on samples HPT process with different equivalent strains: intensity I_2 of the component correspoding to the positrons trapped in defect. The dependence of mean positron lifetime on equivalent strain is shown in the inset.

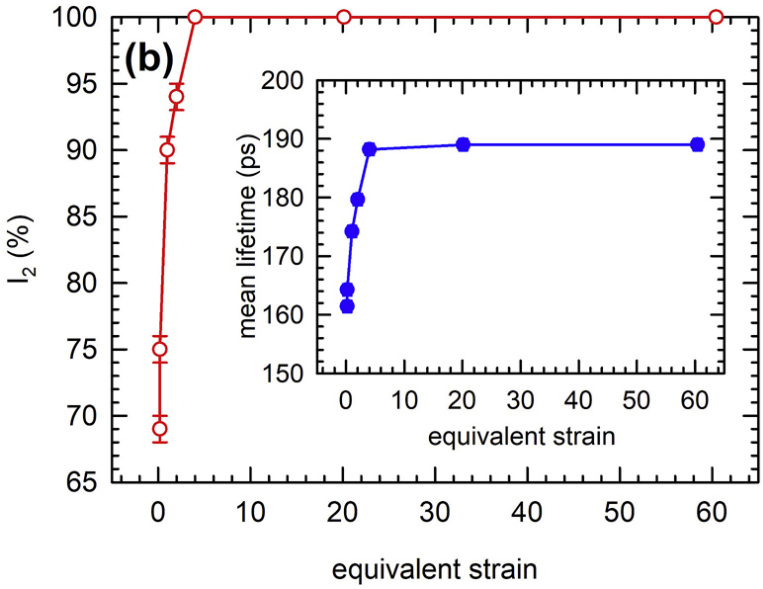

Severe plastic deformation introduces dislocations. But dislocations are rather shallow traps for positrons. Positrons trapped in dislocations usually diffuse along the dislocation line and get trapped in vacancies bound to the dislocation. Therefore the lifetime 189 ps can be expected to be a mean value of lifetimes of positrons trapped in various kind of vacancies surrounded by various atoms the alloy is composed of.
In figure the mean positron lifetime as a function of equivalent strain is plotted. The mean positron lifetime is given by the equation

$$\tau_{mean} = \tau_1 I_1 + \tau_2 I_2. \tag{5.1}$$

At the beginning, the mean positron lifetime sharply increases because of increase of concentration of defects introduced in the sample by plastic deformation. For samples with equivalent strain $e > 5$, the mean positron lifetime saturates at around 189ps, which corresponds to the fact that virtually all positron are trapped in defects and annihilate from the trapped state. This means that by methods of positron annihilation spectroscopy the concentration of defects only for equivalent strains $e < 5$ can be determined.
For equivalent strains $e < 5$ the concentration of the defects can be determined using the conventional two state trapping model described in chapter 2. The model relies on three basic assumptions. In order to check whether these assumptions were satisfied, the parameter τ_f given by the equation

$$\tau_f = \left(\frac{I_1}{\tau_1} + \frac{I_2}{\tau_2} \right)^{-1} \tag{5.2}$$

was calculated. For samples with $e < 5$ the parameter was about 146 ps, which corresponds well to the bulk lifetime of free positrons in a well annealed and

therefore nearly defectless sample of HfNbTaTiZr. This means that the assumptions of the conventional trapping model are satisfied and that one can use it to determine the concentration of defects.
The concentration of defects was determined from the equations

$$c = \frac{K}{\nu}, \tag{5.3}$$

$$K = I_2 \left(\frac{1}{\tau_1} - \frac{1}{\tau_2} \right). \tag{5.4}$$

The specific positron trapping rate should lie in the range of $10^{-5} - 10^{-4}\,\mathrm{m^2 s^{-1}}$, which are typical values for dislocations in metals. Because the HfNbTaTiZr alloy has BCC structure, the value of $\nu = 0.4 \cdot 10^{-4}\,\mathrm{m^2 s^{-1}}$ corresponding to BCC α-Fe was used.
Using this value of positron trapping rate, the following concentrations of dislocations were found: for HPT processed sample with no torsion ($N = 0$) $c \approx 1 \cdot 10^{-14}\,\mathrm{m^{-2}}$ and for HPT processed sample with equivalent strain $e = 2$ it was $c \approx 6 \cdot 10^{-14}\,\mathrm{m^{-2}}$. When the concentration of dislocations increased over $c \approx 8 \cdot 10^{-14}\,\mathrm{m^{-2}}$ all the positrons were trapped in the dislocations.

5.3 Microhardness development

Vickers microhardness was measured on the HPT processed samples with different equivalent strains in nodes of a rectangular mesh with node spacing of 0.5 mm. The maps of Vickers hardness for different equivalent strains are shown in figure 5.7. As expected, for smaller number of revolutions N the hardness is the largest near the edges of the sample, which were deformed with the largest strain. As N increases the region of higher hardness gets bigger and tends to the center of the sample. For $N = 5$ the sample shows nearly uniform microhardness across the whole surface. Further plastic deformation with higher number of revolutions N lead to only a slight increase of microhardness.

Figure 5.7: Map of Vickers microhardness for HPT processed samples with different number of revolutions N.

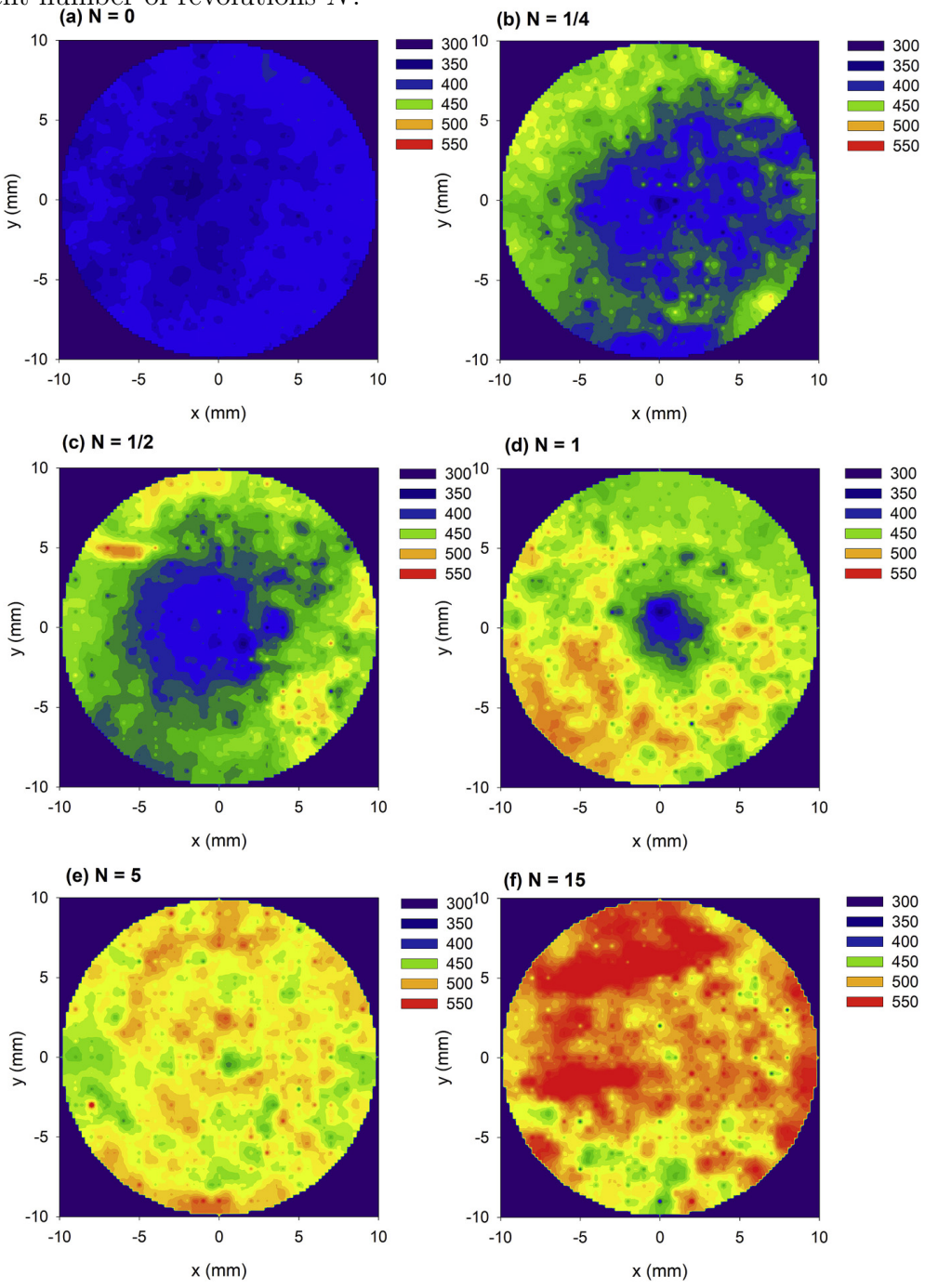

The dependence of microhardness on equivalent strain is shown in figure 5.8. For the purpose of this graph, microhardness values measured at the same distance from the disk center r were averaged.

Figure 5.8: Development of microhardness as a function of equivalent strain.

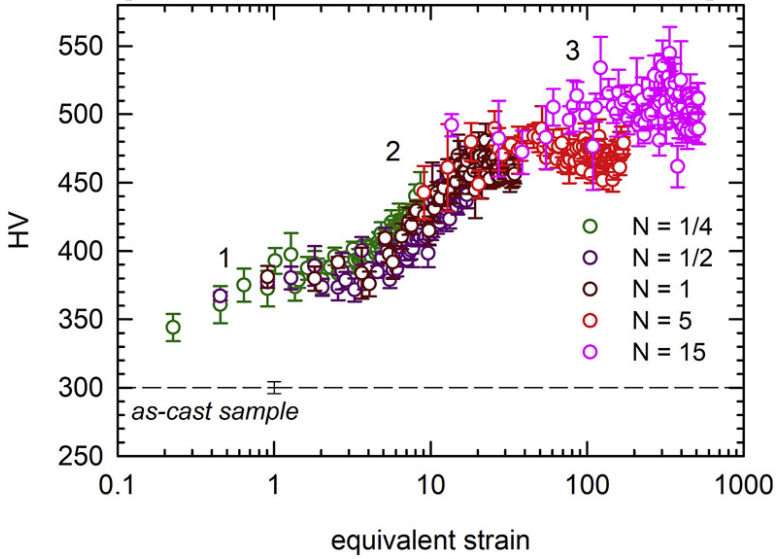

The development of microhardness shows three distinct stages. The first stage occurs for deformation with small equivalent strain ($e < 2$). As mentioned above, the deformation with such small equivalent strains did not lead to significant grain refinement. In the first stage the microhardness increases due to work hardening by dislocations caused by severe plastic deformation.
For equivalent strains $e = 2$ to $e = 3$ the microhardness is HV ≈ 390. For higher strains the ultrafine grain structure starts to form, which causes the microhardness to increase to values around HV ≈ 490 and mark the stage 2.
For very high equivalent strains $e > 100$ the stage 3 occurs. It is characterised by additional slight increase in microhardness to values around HV ≈ 510. This increase is not caused by grain refinement, which was shown by TEM investigations. It is caused by decomposition of HfNbTaTiZr solid solution as shall be explained later.

5.4 Tensile measurements

Figure 5.9 shows tensile stress-strain curves for miniature tensile samples of as-cast sample and HPT processed samples with different equivalent strains. The as-cast sample has the yield strength $R_{p0.2} = 1030(50)$ MPa, the ultimate strength $R_m = 1070(30)$ MPa and the total elongation to failure of 15(3)%. These values were compared with values obtained from tensile stress-strain curve of standard dog-boneshape specimen in the as-cast state. The curve is shown in figure 5.10. The measurements on the standard specimen showed yield strength $R_{p0.2} = 1000(10)$ MPa, the ultimate strength $R_m = 1010(10)$ MPa and the total elongation to failure of 13(2)%. It is clear that measurements done on both samples were comparable to each other.

Figure 5.9: Tensile stress-strain curves for as-cast sample and HPT processed samples with different equivalent strain measured on miniature samples.

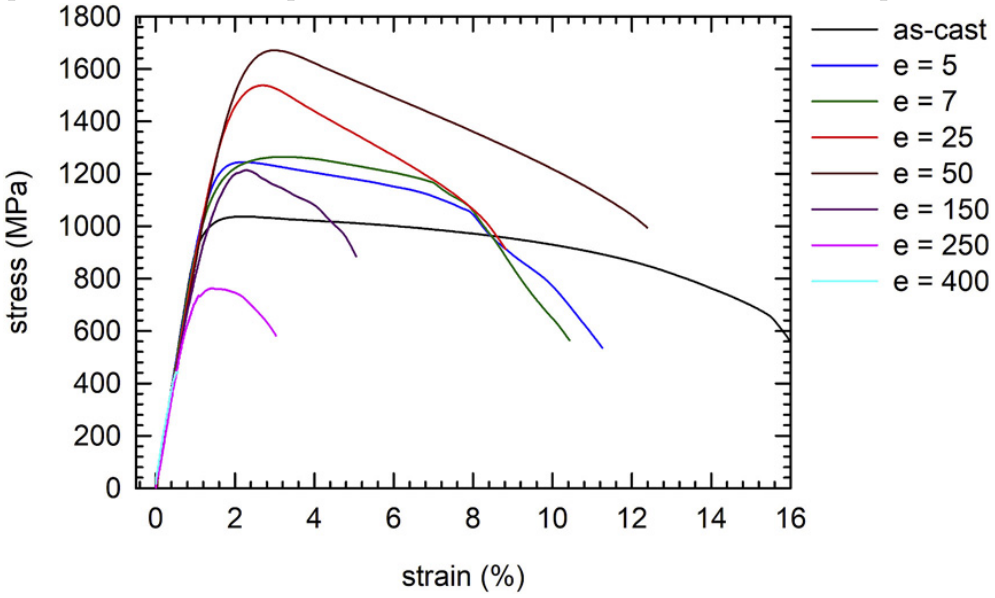

Figure 5.10: Tensile stress-strain curve for as-cast sample measured on standard dog-boneshape specimen.

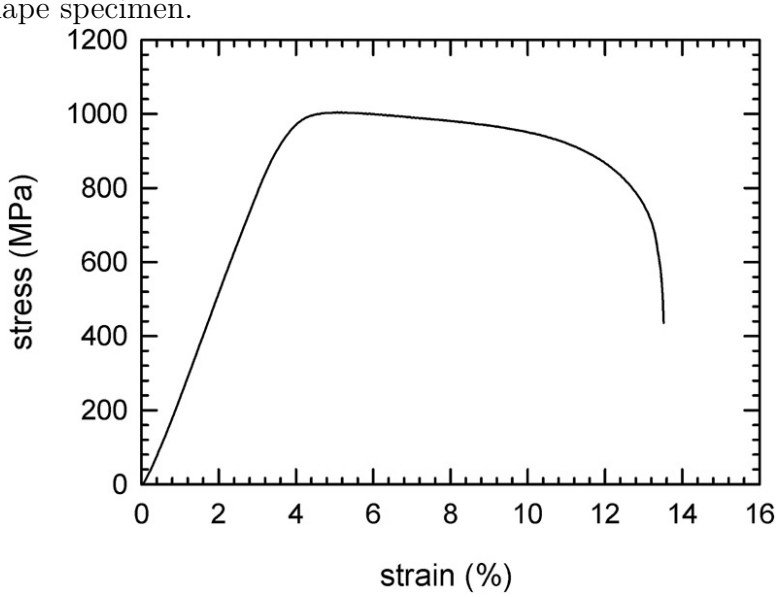

Figure 5.11 shows the development of yield strength and ductility of HPT processed samples. The yield strength of samples deformed with equivalent strain around $e \approx 50$ increased to $R_{p0.2} = 1480(50)$ MPa and the ultimate strength increased to $R_m = 1670(40)$ MPa. The ductility of the HPT processed samples decreased, but was still around 10%. HPT processed samples with equivalent strain larger than $e > 100$ exhibit large decrease of strength even below the value for as-cast sample and drastic decrease of ductibility.

Figure 5.11: a) Yield strength and b) total elongation to failure of HPT processed samples as a function of equivalent strain.

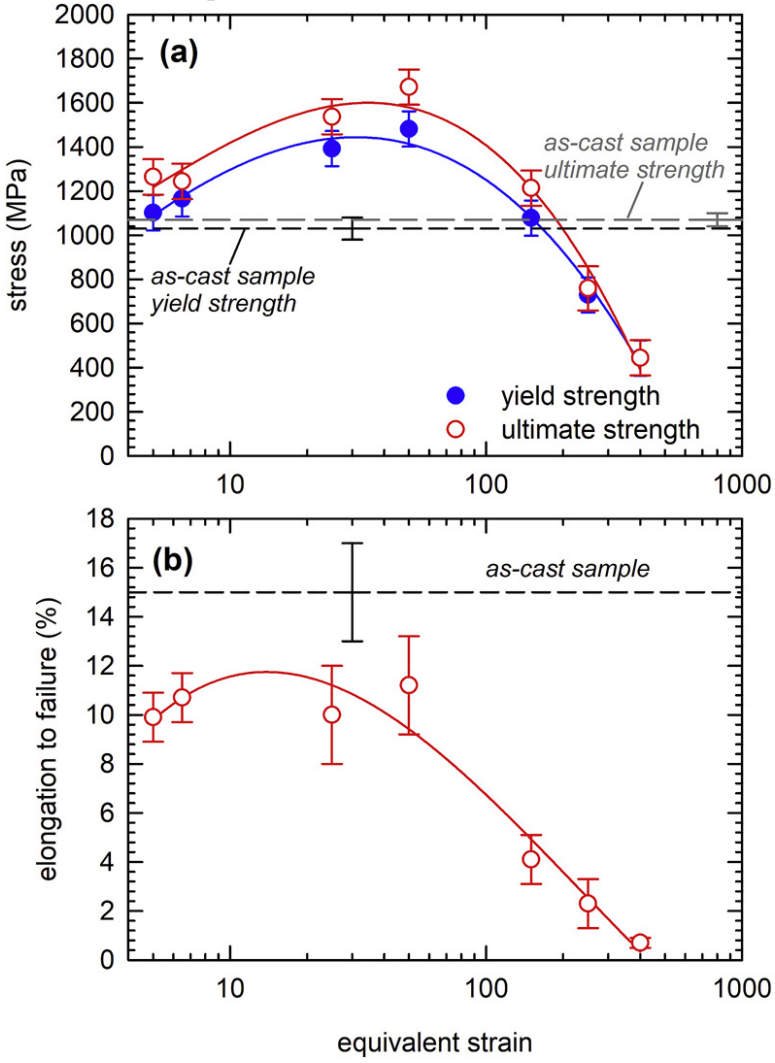

Fracture surfaces of samples ruptured during tensile tests were investigated using SEM. SEM photographs are shown in figure 5.12. As-cast sample and HPT processed samples with smaller equivalent strains $e < 50$ all exhibited a ductile fracture. The size of the dimples of the as-cast sample suggested that the fracture occured by nucleation, growth and coalescence of microvoids. The same could be said about the HPT processed sample with equivalent strain $e \approx 50$, but this time the dimples were smaller, which indicated shorter stage of plastic flow.

Figure 5.12: Fracture surfaces of HfNbTaTiZr alloy samples after their rupture in the tensile test. Individual scans show: a) and d) as-cast sample, b) and e) HPT processed sample $e = 50$, c) and f) HPT processed $e = 400$.

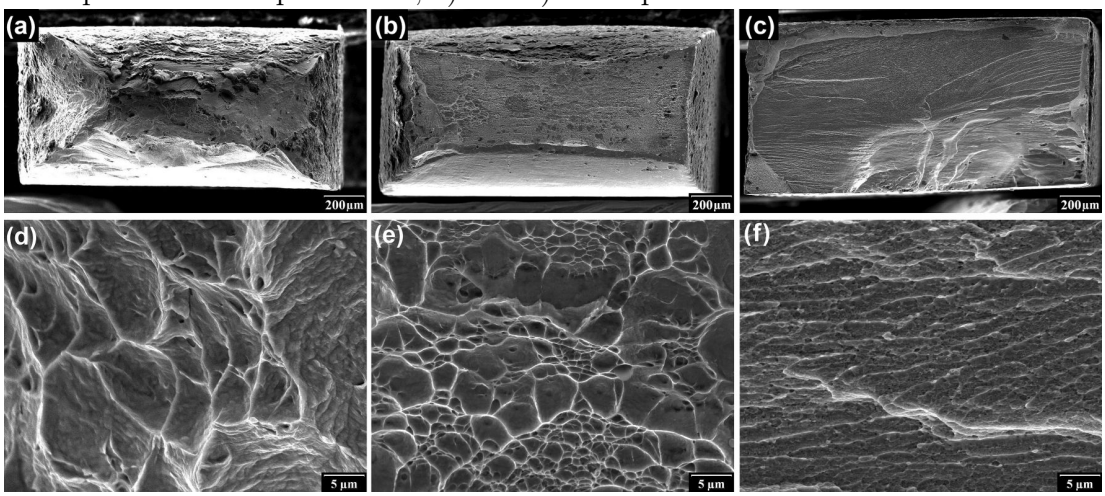

On the other hand, the fracture surfaces of HPT processed samples with equivalent strain larger than $e > 50$ were flat. Fracture occured in a plane that corresponded to the region of localized strain.

5.5 Discussion

When deformed with lower equivalent strains, the microstructure of the samples was rather inhomogeneous. It consisted of areas with coarse grains and of areas with ultra fine refined structure. Deformation of HPT processed samples was localized in shear bands where grain refinement took place.
Work hardening occured during HPT processing with lower equivalent strain corresponding to the stage number one of the microhardness measurement. The positron annihilation lifetime measurement testified that the reason for this were dislocations produced in the samples during plastic deformation.
Twinning was observed on EBSD maps during earlier stages of HPT processing. It has been suggested by Miracle and Senkov [2017] that the twinning should contribute to the good ductility of HfNbTaTiZr alloy.

5.6 Solid solution decomposition

A single phase solid solution HfNbTaTiZr is not thermodynamically stable at ambient temperature. According to Calphad calculations, rather a mechanical mixture of Zr, Hf rich HCP phase and Ta, Nb rich BCC phase forms. However, since the diffusivity of the elements from which the alloy consists is low, a solid solution can exist as a metastable structure. Schuh et al. [2018] Dirras et al. Dirras et al. [2015] experimentally proved this by investigating samples solidified with various cooling rates.
The figure 5.13 shows a SEM backscatter electron micrograph of an as-cast sample and samples annealed at 650°C and 700°C for one hour. The structure of the as-

cast sample is nearly uniform, micrographs of the annealed samples show phase separation. The regions rich in Ta, Nb appears brighter, since the average atomic number Z of such regions is $Z = \frac{73+41}{2} = 57$, as opposed to the regions rich in Zr and Hf with average atomic number $Z = \frac{40+72}{2} = 56$. Figure 5.14 shows a microhardness map of the as-cast sample and the sample annealed at 650°C. The microhardness of the as-cast sample is homogeneous due to the uniform microstructure. On the other hand, the microhardness of the annealed sample is inhomogeneous. The reason for that is that the regions probed by the indents contained both phases with different mechanical properties.

Figure 5.13: SEM BSE micrograph of a) an as-cast sample, b) sample annealed at 650°C for one hour and c) sample annealed 700°C for one hour.

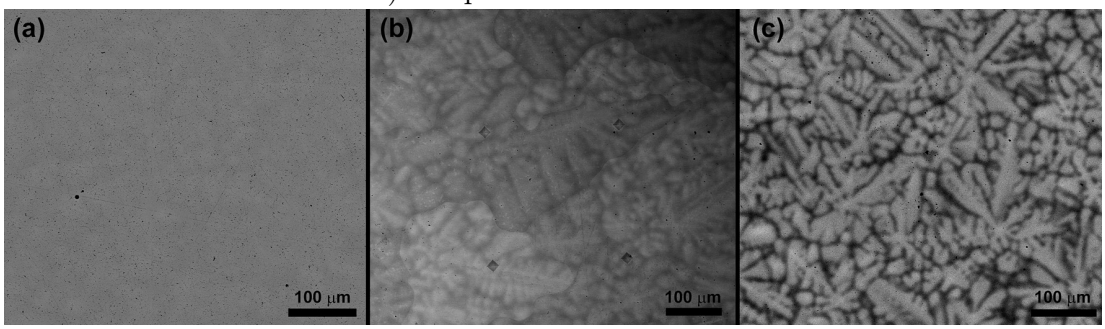

Figure 5.14: a) microhardness map of the as-cast sample, b) microhardness map of the sample annealed at 650°C, c) histogram of measured microhardness values.

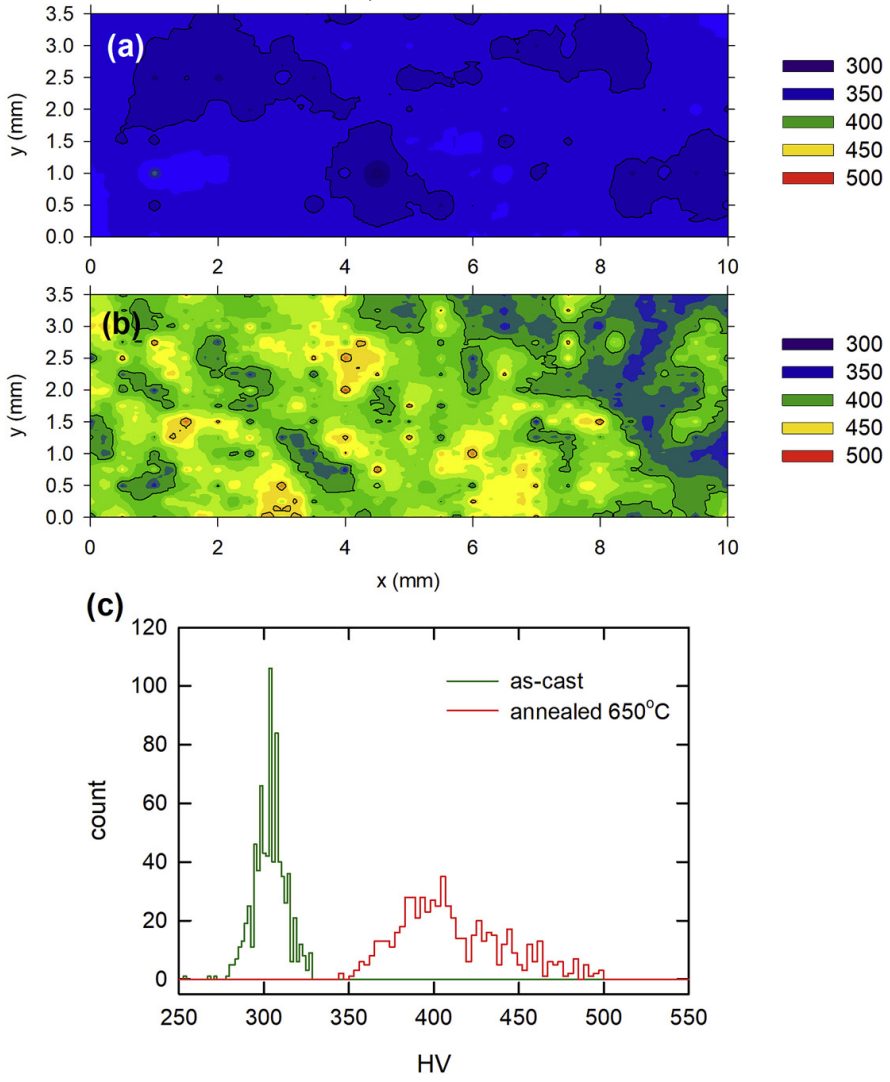

HPT processing caused a high density of dislocations and vacancies, which accelerates diffusion. Zhilyaev and Langdon [2008] Grain boundaries also contributed to the acceleration of diffusion by providing fast diffusion channels. Valiev et al. [1993] Particles rich in Zr and Hf were observed to nucleate at grain boundaries. To investigate this, a coarse grained sample and an ultra fine refined one (HPT processed with equivalent strain $e \approx 50$) were subjected to an isothermal annealing at 200°C and microhardness was measured after each step. The results are shown in figures 5.15 and 5.16. It can be seen that the microhardness remains constant (within statistical error) in the coarse grained sample, whereas it increases with annealing time in the refined sample. This shows that the stability of the random solid solution is lower in the HPT processed sample than in the coarse grained one. Apart from the rise of microhardness, the decomposition leads to a loss of ductility and a decrease in strength.

Figure 5.15: The development of microhardness during isothermal annealing at 200°C of the as-cast sample.

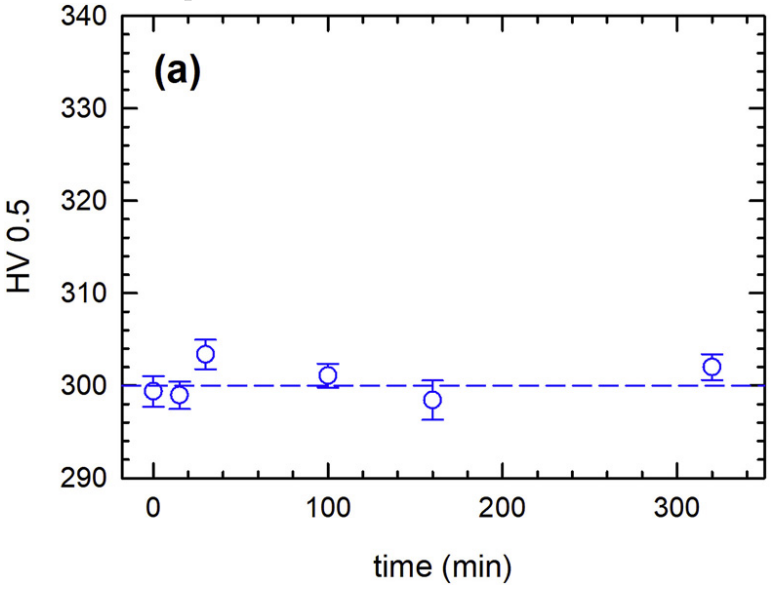

Figure 5.16: The development of microhardness during isothermal annealing at 200°C of the HPT processed ($e \approx 50$) sample.

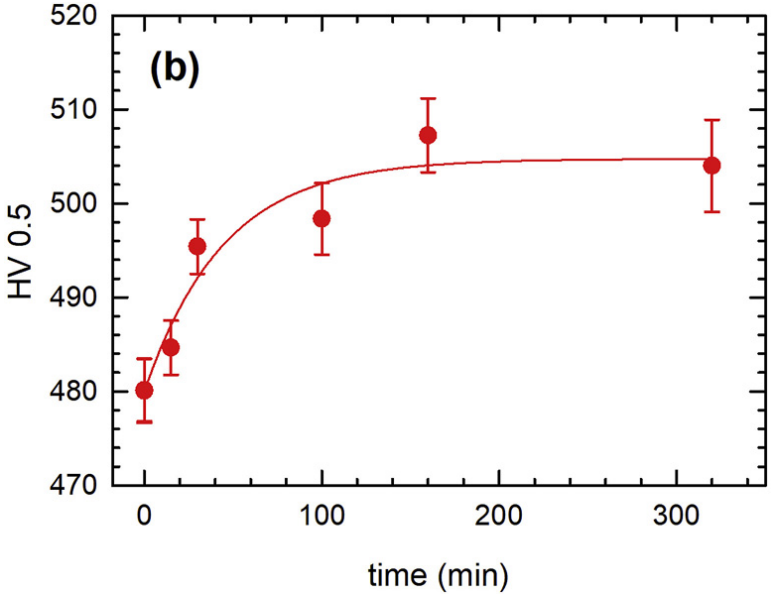

As was determined by Schuh et al. [2018], hardness of the Zr, Hf rich phase is around 280 HV, hardness of the Ta, Nb phase is around 268 HV and hardness of the random solid solution is around 300 HV. This is supportive of the idea that the rise of microhardness after solid solution decomposition is caused by misfit strengthening predominantly from the misfit between Nb-Ta-Ti and Zr-Hf. Since atoms of Nb, Ta and Ti have similar dimensions, the misfit between these atoms should be small. The same applies to Zr and Hf misfits. The interfaces between the Nb-Ta-Ti and Zr-Hf phases serve as obstacles to dislocation movement. Apart from that, nanometer sized particles of Zr, Hf rich phase lead to precipitation

strengthening in deformed samples with larger equivalent strains $e > 50$. Čížek et al. [2018]

6. Lattice distortions

6.1 Lattice distortion quantification in HEAs

Lattice distortions represent one of the main characteristics of high entropy alloys. Since HEAs contain five or more elements of different atomic size, it is supposed that their lattice is significantly distorted. To quantify the distortions and describe the average atomic size differences, the so-called atomic misfit parameter δ is employed. It is defined by the equation

$$\delta = \sqrt{\sum_{i=1}^{N} c_i \left(1 - \frac{r_i}{\overline{r}}\right)^2}, \tag{6.1}$$

where c_i is the concentration of the i-th elemental constituent, r_i is the atomic radius of the i-th elemental constituent, N is the number of elemental constituents and $\overline{r}$ is the weighted average of atomic radii defined by the relation

$$\overline{r} = \sum_{i=1}^{N} c_i r_i. \tag{6.2}$$

Quantification of lattice distortions in HEAs is difficult. Attempts in this direction are complicated by the stochastic nature of the distortions and the fact that they occur on the atomic scale.

Series of twenty HEAs consisting of Hf, Zr, Nb, Ta, Ti, V, Zr were investigated. Each sample was prepared from pure elements (with 99.99% purity) using vacuum arc melting. To achieve homogeneity, each ingot was 10 times remelted. Samples were cut from cast ingots, they had shapes of thin rectangular parallelepipeds with dimensions of 10, 10 and 1 mm. To recover crystal defects introduced during casting and cutting, samples were annealed at 1200 °C for 2 hours in a vacuum chamber (pressure 10^{-5} mbar).

For investigations of the samples the following equipment was used. For scanning electron microscopy, FEI Quanta 200F microscope equipped with detector for energy dispersive X-ray spectroscopy (EDS) was employed. For X-ray diffraction studies, Bruker D8 Discover diffractometer with a 1D LynxEye detector was used. Microhardness measurements were done using Struers Durascan 5 tester. A load of 0.5 kg was applied for 10 s during measurements. For positron annihilation studies of the samples, a ^{22}Na positron source with activity of around 1 MBq deposited on 7 μm thick Kapton foil was used. To carry out measurements, digital spectrometer described in Bečvář et al. [2005] with the time resolution of 144 ps was used.

For each of the HEAs the misfit parameter δ was calculated using equation 6.1. The half of the distance of nearest neighours in the stable phase under standard conditions was used as the atomic radius r_i for each element. The molar configuration entropy of solid solution S_{SS} and the mixing enthalpy of solid solution H_{SS} was calculated using the Miedema's model Takeuchi and Inoue [2005]. As can be seen from the data, H_{SS} decreases with the misfit parameter. The values of H_{SS} and δ for the alloys studied suggest that formation of solid solution should be expected. Negative correlation between H_{SS} and δ can be seen in figure 6.1.

As-cast samples of studied alloys exhibit dendritic structure. As an example, let us consider the case of HfNbTaTiZr aloy shown in picture 4.6. All studied alloys have BCC structure, as was confirmed by XRD analysis. When annealed at 1200 °C for two hours, a single phase random solid solution was formed. Furthermore, dislocations that were introduced in the samples during cutting were fully recovered.
Positron spectrum of the well annealed samples contain only one component (apart from the source component), which corresponds to annihilation of delocalized positrons. The lifetimes of decolalized positrons fall in the interval $(138 - 150)$ ps as can be seen from table 6.1. When these lifetimes are plotted against misfit parameter δ, it can be seen that they increase as δ increases (see figure 6.2). This means that positrons are sensitive to the lattice distortions present in HEAs and positron lifetime measurements can be used as a measure of lattice distortions. This was also supported by theoretical calculations of bulk positron lifetime in Čížek et al. [2022].

Figure 6.1: H_{SS} as a function of misfit parameter δ for studied alloys.

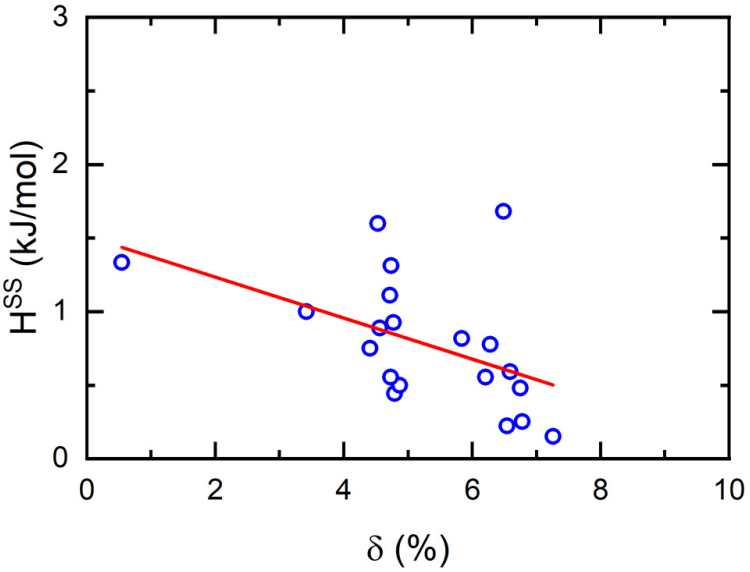

Figure 6.2: Bulk positron lifetimes τ_B as a function of the atomic misfit parameter δ. Circles show exeprimentally determined lifetimes, stars and triangles calculated lifetimes determined using the weighted average approach or randomly filled supercells approach.

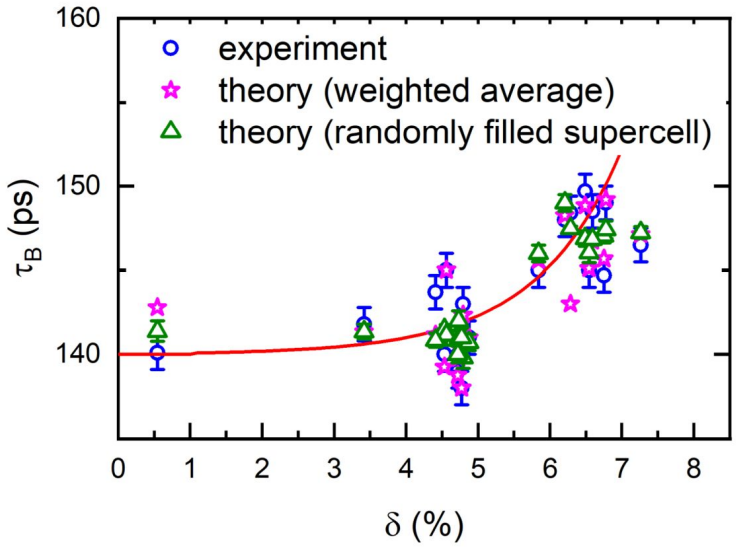

Lattice distorsions in HEAs are usually thought to be connected with strengthening, as was explained in the first chapter. This was investigated in case of previously studied alloys using Vickers microhardness testing. Vickers microhardness values are listed in table 6.1 and are plotted as a function of misfit parameter δ in figure 6.3. It can be seen that lattice distortion in the case of these alloys indeed cause strengthening.

Figure 6.3: Microhardness as a function of misfit parameter δ for studied alloys.

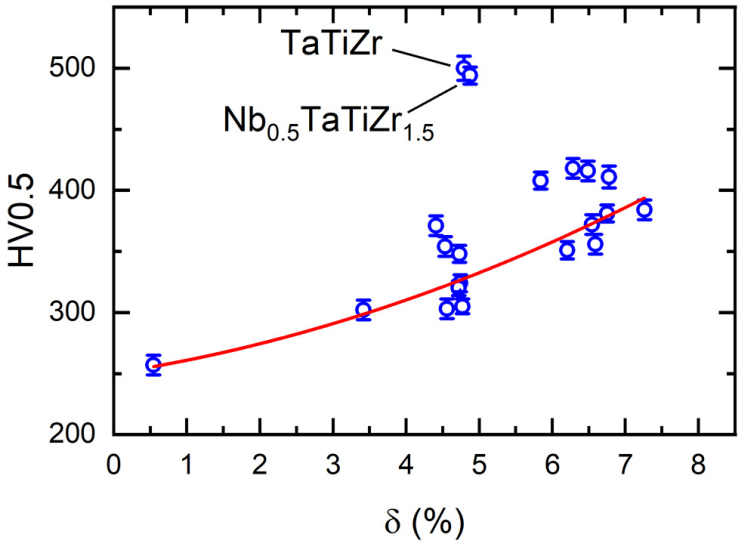

Table 6.1: Studied alloys, their composition and properties.

alloy	δ (%)	S_{SS} (R)	H_{SS} (kJ $\cdot$ mol^{-1})	Z	a (Å)	HV0.5	τ_B (ps)
NbTaTi	1.05	1.10	1.33	45.3	3.2969(7)	257(8)	140(1)
NbTiZr	5.03	1.10	0.89	34.3	3.3969(6)	303(9)	145(1)
TaTiZr	5.01	1.10	0.44	45.0	3.4460(8)	500(10)	143(1)
NbTaTiZr	4.83	1.39	0.75	44.0	3.3509(8)	371(8)	144(1)
NbTiVZr	7.04	1.39	0.25	31.5	3.3153(5)	411(9)	149(1)
$Nb_{0.5}TaTiZr_{1.5}$	5.22	1.32	0.50	43.9	3.3220(9)	494(7)	141(1)
$Nb_{1.5}TaTiZr_{0.5}$	3.83	1.32	1.00	44.1	3.4511(9)	302(8)	142(1)
$Nb_2TaTiZr_2$	5.27	1.33	0.56	42.8	3.3882(3)	348(7)	140(2)
Nb_2TiVZr_2	6.91	1.33	0.22	34.5	3.3530(2)	372(8)	145(1)
$HfNb_4TaTiZr_4$	5.43	1.39	0.93	44.6	3.4520(9)	305(6)	138(1)
HfNbTaTiZr	4.98	1.61	1.60	46.0	3.4081(4)	354(8)	140(1)
HfNbTiVZr	7.06	1.61	0.48	39.8	3.3624(4)	381(7)	145(1)
$Hf_{0.5}Nb_{1.5}TiV_{1.5}Zr_{0.5}$	6.70	1.50	1.68	34.8	3.2827(4)	416(8)	150(1)
$Hf_{0.75}Nb_{0.75}TiV_{1.25}Zr_{1.25}$	7.53	1.58	0.15	37.1	3.3538(3)	384(8)	147(1)
$HfNbTiVZr_{0.5}$	6.88	1.58	0.59	39.6	3.3415(3)	356(8)	149(1)
$Hf_{0.5}NbTa_{0.5}TiZr$	5.00	1.56	1.31	43.9	3.4033(5)	324(7)	140(1)
$HfNbTaTiZr_2$	5.15	1.56	1.11	48.0	3.4270(5)	320(6)	139(1)
$HfNbTi_2VZr$	6.46	1.56	0.56	36.7	3.3501(4)	351(7)	148(1)
HfNbTaTiVZr	6.58	1.79	0.78	45.2	3.3551(2)	418(8)	148(1)
$HfNbTaTi_2VZr$	6.10	1.75	0.82	41.9	3.3413(2)	408(7)	145(1)

6.2 Lattice distortion quantification in HfNbTaTiZr alloy

In this section investigation of lattice distortion of HfNbTaTiZr alloy using techniques of positron annihilation spectroscopy is discussed. HfNbTaTiZr samples for this type of investigation were prepared by vacuum arc melting from pure metals of 99.99% purity. Casting was done in a water cooled copper crucible. Ingots were ten times re-melted and flipped over before each melting to ensure proper mixing of elements. Samples of dimensions of 1 mm x 1 mm x 10 mm^3 were cut using a water cooled saw with a diamond wheel.
Samples were sealed in a quartz ampoule filled with argon and evacuated to the pressure of 10^{-6} mbar. The ampoules were then annealed at 1000 °C for one hour. Upon annealing ampoules were either quenched into water or left to cool slowly in the furnace. One sample was cold rolled to thickness reduction of 30% at ambient temperature.
Apart from positron annihilation techniques, scanning electron microscopy (SEM) measurements were carried out on FEI Quanta 200F microscope equipped with spectrometer for energy dispersive X-ray spectroscopy (EDS). Positron annihilation measurements were done using a standard ^{22}Na positron source with activity of 1.5 MBq deposited on a 2 μm thick Mylar foil and spectrometer with time resolution of 145 ps. Each positron lifetime spectrum consisted of at least 10^7 positron annihilation events.
For purposes of positron lifetime spectrum decomposition source components to the spectrum needs to be known. Lifetimes of source components can be evaluated from measurements taken on well annealed pure metals, for which the lifetime of the free positron component is well known. They are $\approx$ 368 ps and $\approx$ 1.5 ns. The former component comes from positron annihilation in the source and the Mylar foil. The latter component is caused by pick-off annihilation ortho-positronium formed in the Mylar foil. Measurements on pure metals also reveal the dependence of intesities of the source components on the Z number of the samples. Interpolation for the average Z number of the HfNbTaTiZr alloy $Z = 49.6$ leads to intensities of 10% (for the $\approx$ 368 ps component) and 1% (for the $\approx$ 1.5 ns). Source components has always been subtracted from the spectra measured on HfNbTaTiZr samples.
Coincidence Doppler broadening (CDB) measurements were done on a digital spectrometer with two HPGe detectors. In each CDB spectrum consisted of at least 10^8 positron annihilation events. All the CDB ratio curves are ratio curves related to a well annealed pure aluminium sample (of 99.9999% purity).
The microstructure of as-cast HfNbTaTiZr alloy shows dendritic structure. Brighter regions in SEM pictures are enriched in Nb and Ta, whereas darker regions are enriched in Hf and Zr. When such samples were annealed at 1000°C and the annealing was finished by a water quenching, a single phase random solid solution microstructure was observed (see figure 6.4).

Figure 6.4: Back-scattered electron SEM image of HfNbTaTZr alloy. The alloy is in a) as-cast , b) annealed at 1000°C and quenched in water.

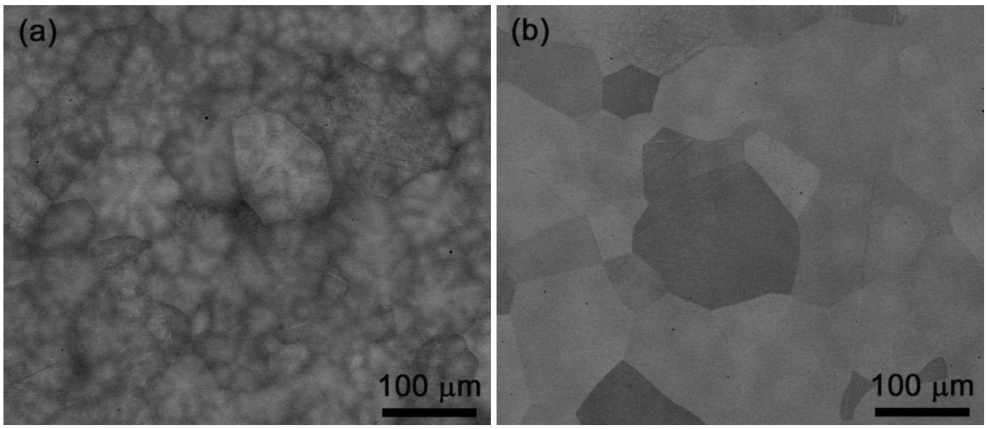

Results of positron annihilation measurements on various HfNbTaTZr alloy samples are listed in table 6.2. Positron lifetime spectra for all samples contain two components. The first component with lifetime τ_1 and intensity I_1 corresponds to annihilation of free positrons, the second component with lifetime τ_2 and intensity I_2 corresponds to annihilation of positrons trapped in defects. It can be expected that the defects were introduced into the as-cast sample mainly due to plastic deformation during cutting of the samples. This hypothesis was verified by PAS investigation of cold rolled samples. As can be seen from the table, the intensity of the second component increased to $I_2 = (88 \pm 2)\%$ for cold rolled sample (as compared to $I_2 = (69 \pm 1)\%$ for the as-cast sample). The lifetime τ_2 did not change, which testifies that the character of the defects was not changed and that the chracteristic lifetime for positrons trapped in dislocations in HfNbTaTZr alloy is around 189 ps.

Table 6.2: Lifetimes τ and intensities I of components resolved in positron spectra of various HfNbTaTZr alloy samples.

Sample	τ_1 (ps)	I_1 (%)	τ_2 (ps)	I_2 (%)
as-cast	105 ± 7	31 ± 3	189 ± 2	69 ± 1
etched 100 μm sub-surface layer	142 ± 1	100	–	–
annealed + slowly cooled	141 ± 1	100	–	–
annealed + water quenched	127 ± 2	68 ± 1	212 ± 2	32 ± 1
cold rolled, $e = 30\%$	51 ± 4	12 ± 2	186 ± 2	88 ± 2

The spectrum for the sample that was annealed at 1000 °C for one hour and then left slowly cooled contain only the first component with lifetime $\tau_1 = 141$ ps. The second component is entirely missing because of recovery of dislocations and vacancies during slow annealing. All positrons annihilated in the free state. It can be concluded that the lifetime of free positron in HfNbTaTZr alloy is around 141 ps.

The spectrum for the sample that was annealed at 1000 °C for one hour and then quenched into water has two components. The first component is again

caused by annihilation of free positrons and the second component is caused by annihilation of positrons trapped at defects. The lifetime of the second component $\tau_2 = 212$ ps is larger than the lifetime of the second component of previously discussed samples. It is because it can be attributed to annihilation of positron in vacancies and not dislocations. Vacancies disappear from the material by means of diffusion during slow cooling to room temperature, but at least part of them can persist in the water quenched sample. Lifetime of positron trapped at vacancies in HfNbTaTZr alloy is therefore likely around 212 ps.

These conclusions can be compared with theoretical calculations in Čížek et al. [2022]. Lifetimes of positrons in the BCC lattice with lattice parameter of 3.41 Å (corresponding to HfNbTaTiZr alloy) but filled only by atoms of single element (i.e. Hf, Nb, Ta, Ti or Zr) were calculated theoretically using density functional theory approach. It was found that the calculated bulk positron lifetimes are close to the measured lifetimes, but calculated lifetimes of positrons trapped in vacancies are considerably higher than the measured ones. This suggests that there is considerable ion relaxation around vacancies in HfNbTaTiZr alloy.

Results of CDB measurements are plotted in figure 6.5. Apart from measurements on the HfNbTaTiZr alloy, measurements on pure Hf, Nb, Ta, Ti, Zr in well annealed and cold roled states were also performed. In the well annealed samples all the positrons annihilate in the free state and therefore ratio curves of well annealed reference samples may be seen as momentum distributions of free positrons annihilated by electrons of corresponding element. On the other hand, nearly all the positrons annihilate when trapped in defects in the cold rolled samples, and therefore the ratio curves for cold rolled samples can be seen as an estimate of the shape of momentum distribution of positrons trapped at vacancies.

Figure 6.5: CDB ratio curves for HfNbTaTiZr alloy and pure elements Hf, Nb, Ta, Ti and Zr.

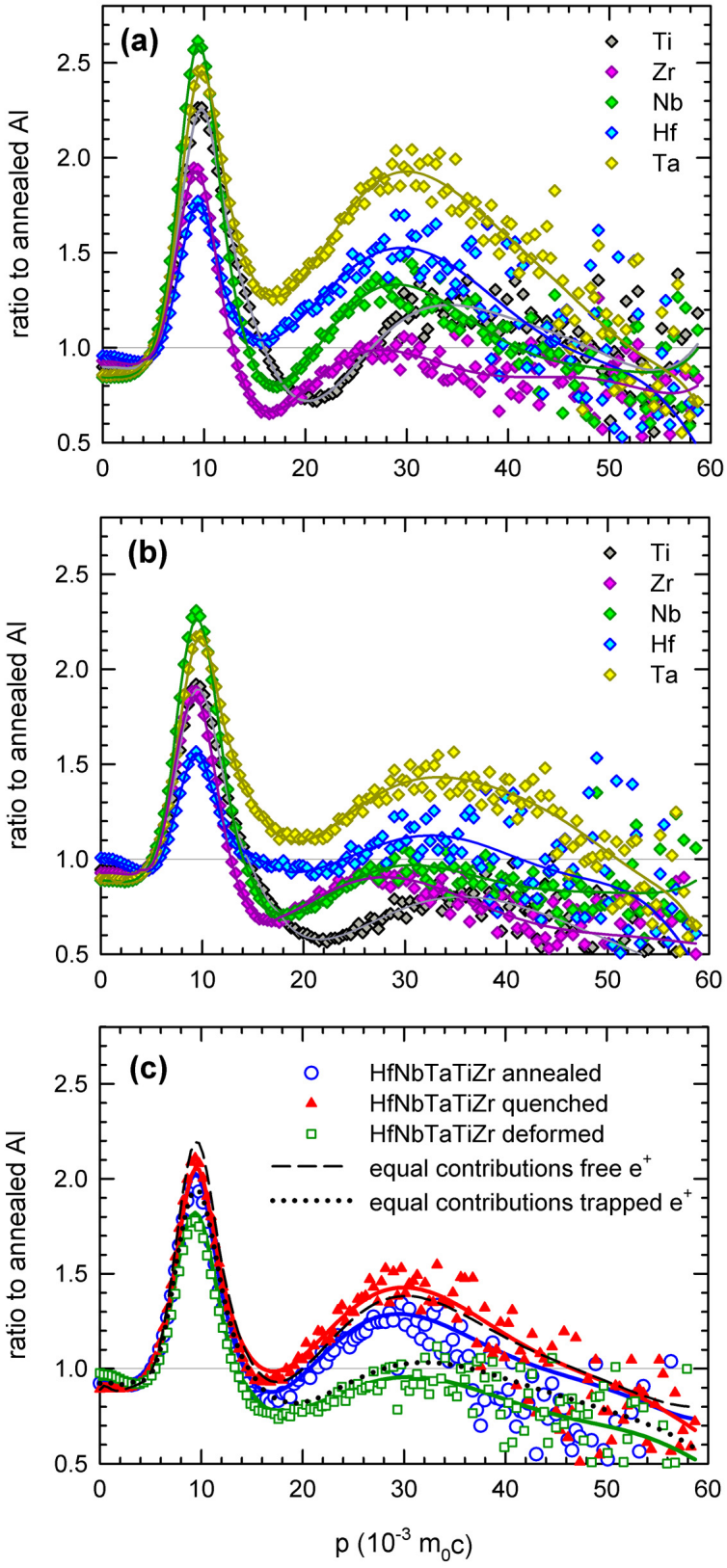

The CDB ratio curves for HfNbTaTiZr alloy show similar features as the ratio curves for pure elements, namely a sharp peak at $p \approx 10 \cdot 10^{-3}\, m_0 c$ and a broader

peak at $p \approx 30 \cdot 10^{-3}\ m_0c$. The high momentum ($p > 10 \cdot 10^{-3}\ m_0c$) region corresponds to annihilation of positrons with core electrons, which are nearly not affected by bonding and retain their atomic character. That is why the ratio curve for cold rolled samples is supressed in this region - positrons trapped in defects annihilate preferentially with low momentum conduction electrons.
The CDB ration curve for HfNbTaTiZr alloy can be in the high momentum region estimated by a function of the following type:

$$\begin{aligned}\rho(p) = (1 - F_D)\,(\xi_{Hf,f}\rho_{Hf,f}(p) + \xi_{Nb,f}\rho_{Nb,f}(p) + \xi_{Ta,f}\rho_{Ta,f}(p) + \\ + \xi_{Ti,f}\rho_{Ti,f}(p) + \xi_{Zr,f}\rho_{Zr,f}(p)) + \\ + F_D(\xi_{Hf,D}\rho_{Hf,D}(p) + \xi_{Nb,D}\rho_{Nb,D}(p) + \\ + \xi_{Ta,D}\rho_{Ta,D}(p) + \xi_{Ti,D}\rho_{Ti,D}(p) + \xi_{Zr,D}\rho_{Zr,D}(p)),\end{aligned} \tag{6.3}$$

where F_D is the fraction of positrons trapped at defects, $\rho_{X,f}(p)$ and $\rho_{X,D}(p)$ are ratio curves for positrons annihilating from a free state or from a defect for element X, $\xi_{X,f}$ denotes the probability that a free positron is annihilated in the vicinity of element X and $\xi_{X,D}$ denotes the probability that a positron is annihilated in the trapped state in the vicinity of element X.
In the case of well annealed HfNbTaTiZr alloy samples $F_D = 0$, because all the positrons annihilate from the free state. The model function 6.3 does not approximate the ratio curve good for $\xi_{Hf,f} = \xi_{Nb,f} = \xi_{Ta,f} = \xi_{Ti,f} = \xi_{Zr,f} = 0.2$ corresponding to equimillar composition of the alloy (see the dashed line in figure 6.5). By fitting the model function 6.3 to the experimental data it was found that the best fit was achieved when $\xi_{Hf,f} = 0.28 \pm 0.03$, $\xi_{Nb,f} = 0.12 \pm 0.02$, $\xi_{Ta,f} = 0.10 \pm 0.02$, $\xi_{Ti,f} = 0.11 \pm 0.02$ and $\xi_{Zr,f} = 0.39 \pm 0.03$. This can be explained by the notion that free positrons are annihilated preferentially near Hf and Zr atoms.
The fraction of positrons that annihilate in the trapped state F_D can be evaluated using the standard trapping model as

$$F_D = I_2 \frac{\tau_2 - \tau_B}{\tau_2 - I_2\tau_B}, \tag{6.4}$$

where τ_B is the bulk positron lifetime in HfNbTaTiZr alloy. After plugging in measured values for the colled rolled samples one can obtain the value of $F_D = 0.64 \pm 0.05$. This value was used in equation 6.3 and subsequently the model function was fitted on experimental data to obtain $\xi_{X,f}$ and $\xi_{X,D}$ coefficients. The calculated coefficients are listed in table 6.3. From the results it can be seen that even in the case of cold rolled samples positrons annihilated preferentially near the Hf and Zr atoms. Positrons trapped at dislocations annihilate additionally near Ti atoms, which suggests that Ti atoms segregated near dislocations.
CDB curves of samples quenched in water upon annealing are surprisingly enhanced in the high momentum region, even though the samples contain frozen vacancies. The factor F_D for these samples was evaluated from equation 6.4 as $F_D = 0.13 \pm 0.03$. This value was plugged in the model function 6.3 and the function was fitted to experimental data. Resulting $\xi_{X,f}$ and $\xi_{X,D}$ coefficients are listed in table 6.3. Positron that are annihilated from the free state annihilate preferentially near Hf and Ta atoms because Hf and Ta atoms contain the largest number of electrons. It suggests that quneching in water prevented

Table 6.3: Fitting coefficients for CDB curves fitted by the model function 6.3.

	annealed slowly cooled	cold rolled	annealed water quenched
free postirons			
$1 - F_D$	1.00	0.35 ± 0.05	0.87 ± 0.03
$\xi_{Hf,f}$	0.28 ± 0.03	0.25 ± 0.04	0.39 ± 0.03
$\xi_{Nb,f}$	0.12 ± 0.02	0.06 ± 0.03	0.11 ± 0.03
$\xi_{Ta,f}$	0.10 ± 0.02	0.05 ± 0.03	0.25 ± 0.03
$\xi_{Ti,f}$	0.11 ± 0.02	0.17 ± 0.03	0.08 ± 0.02
$\xi_{Zr,f}$	0.39 ± 0.03	0.47 ± 0.04	0.17 ± 0.02
trapped positrons			
F_D	0	0.64 ± 0.05	0.13 ± 0.03
$\xi_{Hf,f}$	–	0.15 ± 0.04	0.90 ± 0.05
$\xi_{Nb,f}$	–	0.10 ± 0.03	–
$\xi_{Ta,f}$	–	0.05 ± 0.03	0.05 ± 0.02
$\xi_{Ti,f}$	–	0.27 ± 0.03	–
$\xi_{Zr,f}$	–	0.43 ± 0.04	0.05 ± 0.02

forming regions enriched in Hf and Zr. Positrons trapped at vacancies annihilate preferentially near Hf solutes.
Figure 6.6 shows CDB curves for HfNbTaTiZr alloy in various states related to the curve for HfNbTaTiZr alloy in the annealed state. In high momentum region, the curve for cold rolled sample is below unity and the curve for annealed and water quenched sample is higher than unity. In cold rolled samples the high momentum area is decreased since positrons get trapped in defects and cannot annihilate with core electrons, as was described above. In the quenched sample there is also a larger concentration of defects (vacancies), but still the CDB curve is not suppressed. This shows that elements from which the alloy consists are not distributed completely randomly around vacancies.

Figure 6.6: CDB ratio curves for various states of HfNbTaTiZr alloy related to curves for annealed HfNbTaTiZr sample.

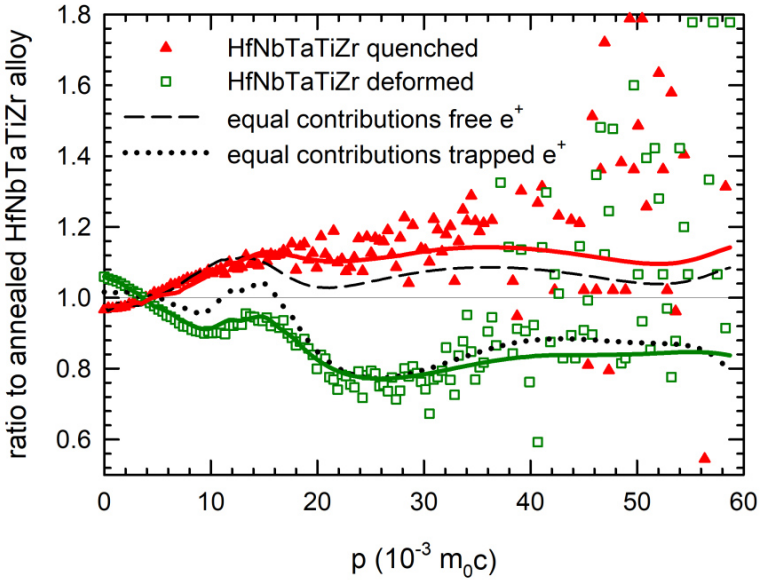

Quenched-in vacancies are located preferentially in the vicinity of Hf atoms. This could be explained by the size of the Hf atoms - they have quite large atomic radius (1.56 Å). The problem with this explanation is that Zr atoms have also rather large atomic radius, even larger than Hf atoms (1.59 Å), yet no enhancement corresponding to Zr atoms is seen in measured CDB curves. This could mean that one needs to consider not only atomic size, but also electronic states. Furthermore, there should be considerable ion relaxation around vacancy, which leads to the reduction of vacancy free volume. This could also explain smaller lifetimes for positrons annihilated from trapped states in vacancies discussed in a preceding section.

Conclusion

In this doctoral thesis equimolar high entropy alloys NbTaTiZr, HfNbTaTiZr, HfNbTiVZr and HfNbTaTiVZr were studied. All of them have disordered BCC structure. In the as-cast state all the alloys exhibit dendritic microstructure and atoms of vanadium segregate at grain boundaries. Upon annealing at 1200 °C for 2 hours finished by water quenching all the alloys except for NbTaTiZr can be described as sigle phase solid solution.

It was proved that strengthening in these HEAs was caused by lattice distortions, which are the result of atoms of various elements having different atomic radii occupying lattice sites randomly. It was also shown that positrons actively search for interstitial regions with extended open volume and are located there with higher probability. Therefore positron lifetimes can be used for characterisation of lattice distortions. Moreover positron annihilation stidies revealed vacancies in HfNbTaTiZr alloy are not distributed randomly, but are preferentialy located in the vicinity of Hf ions.

Bibliography

S. Agostinelli, J. Allison, K. Amako, J. Apostolakis, H. Araujo, and D. Arce, P. ... Zschiesche. Geant4—a simulation toolkit. *Nuclear Instruments and Methods in Physics Research Section A: Accelerators, Spectrometers, Detectors and Associated Equipment*, 506(3):250–303, 2003.

F. Bečvář, J. Čížek, I. Procházka, and J. Janotová. The asset of ultra-fast digitizers forpositron-lifetime spectroscopy. *Nuclear Instruments and Methods in Physics Research A*, 539(1):372–385, 2005.

B. Cantor, I. T. H. Chang, P. Knight, and A. J. B. Vincent. Microstructural development in equiatomic multicomponent alloys. *Materials Science and Engineering: A*, 375–377:213–218, 2004.

G. Dirras, J. Gubicza, A. Heczel, L. Lilensten, J.-P. Couzinié, L. Perrière, I. Guillot, and A. Hocinia. Microstructural investigation of plastically deformed Ti20Zr20Hf20Nb20Ta20 high entropy alloy by X-ray diffraction and transmission electron microscopy. *Materials Characterization*, 108:1–7, 2015.

D. Drouin, A. R. Couture, D. Joly, X. Tastet, V. Aimez, and R. Gauvin. CASINO V2.42—A Fast and Easy-to-use Modeling Tool for Scanning Electron Microscopy and Microanalysis Users. *Scanning*, 29(3):92–101, 2007.

R. F. Egerton. *Physical Principles of Electron Microscopy*. Springer, 2005.

J. Čížek. Měření doby života pozitronů a jeho využití při studiu kovových materiálů. *Pokroky matematiky, fyziky a astronomie*, 44(3):201–217, 1999.

J. Čížek, M. Vlček, and I. Procházka. Digital spectrometer for coincidence measurement of Doppler broadening of positron annihilation radiation. *Nuclear Instruments and Methods in Physics Research A*, 623:982–994, 2010.

J. Čížek, P. Haušild, M. Cieslar, O. Melikhova, T. Vlasák, M. Janeček, R. Král, P. Harcuba, F. Lukáč, J. Zýka, J. Málek, J. Moon, and H. S. Kim. Strength enhancement of high entropy alloy HfNbTaTiZr by severe plastic deformation. *Journal of Alloys and Compounds*, 768(5):924–937, 2018.

J. Čížek, T. Vlasák, and O. Melikhova. Characterization of Lattice Defects in Refractory Metal High-Entropy Alloy HfNbTaTiZr by Means of Positron Annihilation Spectroscopy. *Physica Status Solidi a*, 219(9), 2022.

J. I. Goldstein, D. E. Newbury, J. R. Michael, N. W. M. Ritchie, J. H. J. Scott, and D. C. Joy. *Scanning Electron Microscopy and X-Ray Microanalysis*. Springer, 2018.

G. Grimvall. *Thermophysical Properties of Materials*. Elsevier, 1999.

P. Hautojärvi. *Positrons in Solids*. Springer-Verlag, 1979.

J. Y. He, W. H. Liu, H. Wang, Y. Wu, X. J. Liu, T. G. Nieh, and Z. P. Lu. Effects of Al addition on structural evolution and tensile propertiesof the FeCoNiCrMn high-entropy alloy system. *Acta Materialia*, 62:105–113, 2014.

P. Hovington, D. Drouin, and R. Gauvin. CASINO: A New Monte Carlo Code in C Language for Electron Beam Interaction. *Scanning*, 19(1):1–14, 1997.

D. H. Lee, M. Y. Seok, Y. Zhao, I. C. Choi, J. He, Z. Lu, J. Y. Suh, U. Ramamurty, M. Kawasaki, T. G. Langdon, and J. Jang. Spherical nanoindentation creep behavior of nanocrystalline andcoarse-grained CoCrFeMnNi high-entropy alloys. *Acta Materialia*, (109):314–322, 2016.

C. Li, X. Cao, F. Liu, P. Zhang, Z. Zhang, L. Wei, and B. Wang. Effect of tissue density on PET spatial resolutionin magnetic environment. *European Physical Journal Plus*, 135(1), 2020.

L. Liu, J. B. Zhu, C. Zhang, J. C. Li, and Q. Jiang. Microstructure and the properties of FeCoCuNiSnx high entropy alloys. *Materials Science and Engineering A*, 548:64–68, 2012.

L. Liu, J. B. Zhu, L. Li, J. C. Li, and Q. Jiang. Microstructure and tensile properties of FeMnNiCuCoSnx high entropy alloys. *Materials and Design*, 44: 223–227, 2013a.

W. H. Liu, Y. Wu, J. Y. He, T. G. Niehband, and Z. P. Lu. Grain growth and the Hall–Petch relationship in a high-entropy FeCrNiCoMn alloy. *Scripta Materialia*, (68):526–529, 2013b.

W. H. Liu, J. Y. He, H. L. Huang, H. Wang, Z. P. Lu, and C. T. Liu. Effects of Nb additions on the microstructure and mechanical propertyof CoCrFeNi high-entropy alloys. *Intermetallics*, 60:1–8, 2015.

A. R. Miedema. A simple model for aloys. i. rules for the alloying behaviour of transition metals. *Philips technical review*, 33(6):149–160, 1973.

D. B. Miracle and O. N. Senkov. A critical review of high entropy alloys and related concepts. *Acta Materialia*, 122:448–511, 2017.

B. S. Murty, J.-W. Yeh, S. Ranganathan, and P. P. Bhattacharjee. *High-Entropy Alloys*. Elsevier, 2019.

H. P. Myers. *Introductory Solid State Physics*. Taylor and Francis, 1997.

F. Otto, A. Dlouhý, Ch. Somsen, H. Bei, G. Eggeler, and E. P. George. The influences of temperature and microstructureon the tensile properties of a CoCrFeMnNi high-entropy alloy. *Acta Materialia*, 61(15):5743–5755, 2013a.

F. Otto, Y. Yang, H. Bei, and E. P. George. Relative effects of enthalpy and entropy on the phase stability of equiatomic high-entropy alloys. *Acta Materialia*, 61(7):2628–2638, 2013b.

B. Schuh, B. Völker, J. Todt, N. Schell, L. Perrière, J. Li, J. P. Couzinié, and A.. Hohenwarter. Thermodynamic instability of a nanocrystalline, single-phase TiZrNbHfTa alloy and its impact on the mechanical properties. *Acta Materialia*, 142:201–212, 2018.

O. N. Senkov, J. M. Scott, S. V. Senkova, D. B. Miracle, and C. F. Woodward. Microstructure and room temperature properties of a high-entropy TaNbHfZrTi alloy. *Journal of Alloys and Compounds*, 509(20):6043–6048, 2011a.

O. N. Senkov, G. B. Wilks, J. M. Scott, and D. B. Miracle. Mechanical properties of Nb25Mo25Ta25W25 and V20Nb20Mo20Ta20W20 refractory high entropy alloys. *Intermetallics*, 19(5):698–/706, 2011b.

O. N. Senkov, S. V. Senkova, and C. Woodward. Effect of aluminum on the microstructure and properties of two refractory high-entropy alloys. *Acta Materialia*, 68:214–/228, 2014.

R. E. Smallman and A. H. W. Ngan. *Modern Physical Metallurgy*. Elsevier, 2014.

A. Takeuchi and A. Inoue. Classification of Bulk Metallic Glasses by Atomic Size Difference, Heat of Mixing and Period of Constituent Elements and Its Application to Characterization of the Main Alloying Element. *Materials Transactions*, 46(12):2817–/2829, 2005.

A. Takeuchi and A. Inoue. Mixing enthalpy of liquid phase calculated by miedema's scheme andapproximated with sub-regular solution model for assessing forming abilityof amorphous and glassy alloys. *Intermetallics*, 18:1779–1789, 2010.

K.-Y. Tsai, M.-H. Tsai, and J.-W. Yeh. Sluggish diffusion in Co–Cr–Fe–Mn–Ni high-entropy alloys. *Acta Materialia*, 61:4887–4897, 2013.

F. Tuomisto and I. Makkonen. Defect identification in semiconductors with positron annihilation: Experiment and theory. *Rev. Mod. Phys.*, (85):1583, 2013.

R. Z. Valiev, I. M. Razumovskii, and V. I. Sergeev. Diffusion along grain boundaries with non-equilibrium structure. *Physica status solidi a*, 139(2):321–335, 1993.

T. Vlasák, J. Čížek, O. Melikhova, F. Lukáč, D. Preisler, M. Janeček, P. Harcuba, M. Zimina, and O. Srba. Thermal stability of microstructure of high entropy alloys based on refractory metals Hf, Nb, Ta, Ti, V, Zr. *Metals*, 12(3):394, 2022.

J.-W. Yeh. Recent progress in high entropy alloys. *Annales De Chimie – Sciencedes Materiaux*, 31:633–648, 2006.

J.-W. Yeh, S.-K. Chen, S.-J. Lin, J.-Y. Gan, T.-S. Chin, T.-T. Shun, C.-H. Tsau, and S.-Y. Chang. Nanostructured High-Entropy Alloys with Multiple Principal Elements: Novel Alloy Design Concepts and Outcomes. *Advanced Engineering Materials*, 6(5):299–303, 2004a.

J.-W. Yeh, S.-K. Chen, S.-J. Lin, J.-Y. Gan, T.-S. Chin, T.-T. Shun, C.-H. Tsau, and S.-Y. Chang. Nanostructured High-Entropy Alloys with Multiple Principal Elements: Novel Alloy Design Concepts and Outcomes. *Advanced Engineering Materials*, 6(5):299–303, 2004b.

A. J. Zaddach, R. O. Scattergood, and C. C. Koch. Tensile properties of low-stacking fault energy high-entropy alloys. *Materials Science and Engineering A*, 636:373–378, 2015.

F. Zhang, C. Zhang, S. L. Chen, J. Zhu, W. S. Cao, and U. R. Kattner. An understanding of high entropy alloys from phasediagram calculations. *CALPHAD: Computer Coupling of Phase Diagrams andThermochemistry*, 45:1–10, 2014.

A. P. Zhilyaev and T. G. Langdon. Using high-pressure torsion for metal processing: Fundamentals and applications. *Progress in Materials Science*, 53: 893—-979, 2008.

List of Figures

List of Tables

List of Abbreviations

HEA ... high-entropy alloy
FCC ... face-centered cubic
BCC ... body-centered cubic
HCP ... hexagonal close-packed
SS ... solid solution
IM ... intermetallic
CCA ... complex concentrated alloy
SEM ... scanning electron miscroscopy
BSE ... back-scattered electron(s)
SE ... secondary electron(s)
EBSD ... electron bascatter diffraction
PAS ... positron annihilation spectroscopy
CDB ... Coincidence Doppler broadening
VAR ... vacuum arc remelting
HPT ... high pressure torsion
XRD ... X-ray diffraction

List of publications

Publications related to high entropy alloys:

1. J. Čížek, P. Haušild, M. Cieslar, O. Melikhova, T. Vlasák, M. Janeček, R. Král, P. Harcuba, F. Lukáč, J. Zýka, J. Málek, J. Moon, H.S. Kim, Strength enhancement of high entropy alloy HfNbTaTiZr by severe plastic deformation, *J. Alloys. Compd.* **768**, 924-937 (2018), doi:10.1016/j.jallcom.2018.07.319, IF = 3.779.
   T. Vlasák was responsible for preparation of samples, microstructure characterization by electron microscopy and analysis of results, author contribution 20%

2. F. Lukáč, M. Dudr, J. Čížek, P. Harcuba, T. Vlasák, M. Janeček, J. Kuriplach, J. Mooon, H.S. Kim, J. Zýka, J. Málek, Defects in High Entropy Alloy HfNbTaTiZr Prepared by High Pressure Torsion, *Acta Physica Polonica A* **134**, 891-894 (2018). doi: 10.12693/APhysPolA.134.891, IF = 0.857
   T. Vlasák was responsible for preparation of samples, microstructure characterization by electron backscattered diffraction and analysis of results, author contribution 20%

3. J. Málek, J. Zýka, F. Lukáč, M. Vilémová, T. Vlasák, J. Čížek, O. Melikhova, A. Macháčková, H.-S. Kim, The Effect of Processing Route on Properties of HfNbTaTiZr High Entropy Alloy, *Materials* **12**, 4022 (2019) doi:10.3390/ma12234022, IF = 2.972.
   T. Vlasák was responsible for preparation of samples, heat treatment and microstructure characterization by electron microscopy, author contribution 20%

4. F. Lukáč, P. Hruška, S. Cichoň, T. Vlasák, J. Čížek, T. Kmječ, O. Melikhova, M. Butterling, M.O. Liedke, A. Wagner, Defects in Thin Layers of High Entropy Alloy HfNbTaTiZr, *Acta Physica Polonica A* **137**, 219-221 (2020) doi: 10.12693/APhysPolA.137.219, IF = 0.579.
   T. Vlasák was responsible for analysis and interpretation of data measured on variable energy slow positron beam, author contribution 15%

5. J. Kuriplach, J. Čížek, T. Vlasák, O. Melikhova, F. Lukáč, J. Zýka, J. Málek, Behavior of Positrons in the HfNbTaTiZr Complex Concentrated Alloy, *Acta Physica Polonica A* **137**, 260-264 (2020)
   doi: 10.12693/APhysPolA.137.260, IF = 0.579.
   T. Vlasák was responsible for simulation of HfNbTaTiZr alloy and analysis of results of theoretical calculations, author contribution 30%

6. J. Čížek, T. Vlasák, O. Melikhova, Characterization of lattice defects in refractory metal high entropy alloy HfNbTaTiZr by means of positron annihilation spectroscopy, *Phys. Stat. Sol. A* **219**, 2100840 (2022) doi: 10.1002/pssa.202100840, IF= 1.98

T. Vlasák was responsible for preparation of samples, heat treatment, microstructure characterization by electron microscopy and analysis of results, author contribution 40%

7. T. Vlasák, J. Čížek, O. Melikhova, F. Lukáč, D. Preisler, M. Janeček, P. Harcuba, M. Zimina, O. Srba, Thermal stability of microstructure of high entropy alloys based on refractory metals Hf, Nb, Ta, Ti, V, Zr, *Metals* **12**, 394 (2022) doi: 10.3390/met12030394, IF = 2.35.
   T. Vlasák was responsible for preparation of samples, positron annihilation measurements, microstructure characterization by electron microscopy and analysis of results, author contribution 60%

Other publications:

1. J. Čížek, P. Hruška, T. Vlasák, M. Vlček, M. Janeček, P. Minárik, T. Krajňák, M. Šlapáková, M. Dopita, R. Kužel, T. Kmječ, J.G. Kim, H.-S. Kim, Microstructure development of ultra fine grained Mg-22 wt%Gd alloy prepared by high pressure torsion, *Mater. Sci. Eng. A* **704**, 181-191 (2017), doi:10.1016/j.msea.2017.07.100, IF=3.094
   T. Vlasák was responsible for preparation of samples and microstructure characterization by electron microscopy, author contribution 25%

2. M. Vlček, J. Čížek, F. Lukáč, P. Hruška, B. Smola, I. Stulíková, H. Kudrnová, P. Minárik, T. Kmječ, T. Vlasák, Hydrogen absorption in Mg-Gd alloy, *Int. J. Hydrogen Energy* **42**, 22598-22604 (2017), doi:10.1016/j.ijhydene.2017.04.012, IF=3.582
   T. Vlasák contributed to microstructure characterization by electron microscopy, author contribution 5%

3. P. Minárik, J. Veselý, J. Čížek, M. Zemková, T. Vlasák, T. Krajňák, J. Kubásek, R. Král, D. Hofman, J. Stráská, Effect of secondary phase particles on thermal stability of ultra-fine grained Mg-4Y-3RE alloy prepared by equal channel angular pressing, *Materials Characterization* **140**, 207-216 (2018), doi:10.1016/j.matchar.2018.04.006, IF = 2.714
   T. Vlasák was responsible for annealing of samples and contributed to defect studies by positron annihilation spectroscopy, author contribution 15%

4. P. Minárik, M. Zimina, J. Čížek, J. Stráská, T. Krajňák, M. Cieslar, T. Vlasák, J. Bohlen, G. Kurz, D. Letzig, Increased structural stability in twin-roll cast AZ31 magnesium alloy processed by equal channel angular pressing, *Materials Characterization* **153**, 199-207 (2019) doi:10.1016/j.matchar.2019.05.006, IF = 3.22.
   T. Vlasák contributed to defect studies by positron annihilation spectroscopy, author contribution 5%

5. J. Čížek, M. Janeček, T. Vlasák, B. Smola, O. Melikhova, R.K. Islamgaliev, S.V. Dobatkin, The Development of Vacancies during Severe Plastic Deformation, *Materials Transactions* **60**, 1533-1542 (2019) doi:10.2320/matertrans.MF201937, IF = 0.764.
   T. Vlasák was responsible for analysis of data obtained by positron annihilation spectroscopy, author contribution 15%

6. O. Melikhova, J. Čížek, P. Hruška, T. Vlasák, J. Fitl, M. Novotný, Investigation of free volumes in phthalocyanines and perylene, *AIP Conference Proceedings* **2182**, 050025 (2019) doi:10.1063/1.5135868
   T. Vlasák was responsible for analysis of data obtained by positron annihilation spectroscopy, author contribution 10%

7. I. Procházka, T. Vlasák, J. Čížek, F. Lukáč, M.O. Liedke, W. Anwand, Y. Jirásková, D. Janičkovič, Quenched-in Vacancies and Hardening of Fe-Al Intermetallics, *Acta Physica Polonica A* **137**, 255-259 (2020)
   doi: 10.12693/APhysPolA.137.255, IF = 0.579.
   T. Vlasák was responsible for preparation of samples and depth resolved defect studies using variable energy slow positron beam, author contribution 40%

8. M. Vlach, J. Čížek, V. Kodetová, M. Leibner, M. Cieslar, P. Harcuba, L. Bajtošová, H. Kudrnová, T. Vlasák, V. Neubert, E. Černošková, P. Kutálek, Phase transformations in novel hot-deformed
   Al–Zn–Mg–Cu–Si–Mn–Fe(–Sc–Zr) alloys, *Materials and Design* (2020) doi: 10.1016/j.matdes.2020.108821, IF = 6.289.
   T. Vlasák contributed to analysis of data measured obtained using coincidence Doppler broadening spectroscopy, author contribution 5%

A. Attachments

A.1 Attachment 1 – Author's publication 1

J. Čížek, P. Haušild, M. Cieslar, O. Melikhova, T. Vlasák, M. Janeček, R. Král, P. Harcuba, F. Lukáč, J. Zýka, J. Málek, J. Moon, H.S. Kim, Strength enhancement of high entropy alloy HfNbTaTiZr by severe plastic deformation, *J. Alloys. Compd.* **768**, 924-937 (2018),
doi:10.1016/j.jallcom.2018.07.319, IF = 3.779.
T. Vlasák was responsible for preparation of samples, microstructure characterization by electron microscopy and analysis of results, author contribution 20%

A.2 Attachment 2 – Author's publication 2

F. Lukáč, M. Dudr, J. Čížek, P. Harcuba, T. Vlasák, M. Janeček, J. Kuriplach, J. Mooon, H.S. Kim, J. Zýka, J. Málek, Defects in High Entropy Alloy HfNbTaTiZr Prepared by High Pressure Torsion, *Acta Physica Polonica A* **134**, 891-894 (2018). doi: 10.12693/APhysPolA.134.891, IF = 0.857

T. Vlasák was responsible for preparation of samples, microstructure characterization by electron backscattered diffraction and analysis of results, author contribution 20%

A.3 Attachment 3 – Author's publication 3

J. Málek, J. Zýka, F. Lukáč, M. Vilémová, T. Vlasák, J. Čížek, O. Melikhova, A. Macháčková, H.-S. Kim, The Effect of Processing Route on Properties of HfNbTaTiZr High Entropy Alloy, *Materials* **12**, 4022 (2019) doi:10.3390/ma12234022, IF = 2.972.

T. Vlasák was responsible for preparation of samples, heat treatment and microstructure characterization by electron microscopy, author contribution 20%

A.4 Attachment 4 – Author's publication 4

F. Lukáč, P. Hruška, S. Cichoň, T. Vlasák, J. Čížek, T. Kmječ, O. Melikhova, M. Butterling, M.O. Liedke, A. Wagner, Defects in Thin Layers of High Entropy Alloy HfNbTaTiZr, *Acta Physica Polonica A* **137**, 219-221 (2020) doi: 10.12693/APhysPolA.137.219, IF = 0.579.
T. Vlasák was responsible for analysis and interpretation of data measured on variable energy slow positron beam, author contribution 15%

A.5 Attachment 5 – Author's publication 5

J. Kuriplach, J. Čížek, T. Vlasák, O. Melikhova, F. Lukáč, J. Zýka, J. Málek, Behavior of Positrons in the HfNbTaTiZr Complex Concentrated Alloy, *Acta Physica Polonica A* **137**, 260-264 (2020)
doi: 10.12693/APhysPolA.137.260, IF = 0.579.
T. Vlasák was responsible for simulation of HfNbTaTiZr alloy and analysis of results of theoretical calculations, author contribution 30%

A.6 Attachment 6 – Author's publication 6

J. Čížek, T. Vlasák, O. Melikhova, Characterization of lattice defects in refractory metal high entropy alloy HfNbTaTiZr by means of positron annihilation spectroscopy, *Phys. Stat. Sol. A* **219**, 2100840 (2022) doi: 10.1002/pssa.202100840, IF= 1.98
T. Vlasák was responsible for preparation of samples, heat treatment, microstructure characterization by electron microscopy and analysis of results, author contribution 40%

A.7 Attachment 7 – Author's publication 7

T. Vlasák, J. Čížek, O. Melikhova, F. Lukáč, D. Preisler, M. Janeček, P. Harcuba, M. Zimina, O. Srba, Thermal stability of microstructure of high entropy alloys based on refractory metals Hf, Nb, Ta, Ti, V, Zr, *Metals* **12**, 394 (2022) doi: 10.3390/met12030394, IF = 2.35.
T. Vlasák was responsible for preparation of samples, positron annihilation measurements, microstructure characterization by electron microscopy and analysis of results, author contribution 60%